LIBRARY
Michigan State
University

This is to certify that the

thesis entitled

A CALORIMETRIC STUDY OF MIXTURES OF
COBALT AND NICKEL CHLORIDE HEXAHYDRATES

presented by

Nguyen Truong Lam

has been accepted towards fulfillment
of the requirements for

Ph.D. degree in Physics

Major professor

Date 9/7/1977

O-7639


MSU

A CALORIMETRIC STUDY OF MIXTURES OF COBALT AND NICKEL CHLORIDE HEXAHYDRATES

By

Nguyen Truong Lam

A DISSERTATION

Submitted to
Michigan State University
in partial fulfillment of the requirements
for the degree of

DOCTOR OF PHILOSOPHY

Department of Physics

1977

G108355

ABSTRACT

A Calorimetric Study of Mixtures of Cobalt and Nickel Chloride Hexahydrates

by

Nguyen Truong Lam

Using a standard He^4 adiabatic calorimeter, we have measured the specific heats of a series of ten mixed crystals with chemical formula $Co_xNi_{1-x}Cl_2\cdot 6H_2O$. All the samples studied show fairly sharp transitions. The critical temperatures thus determined vary continuously from 2.43°K to 4.47°K for x ranging from 0.89 to 0.13. The Néel temperatures for $x = 1$ and $x = 0$ have been determined earlier as 2.29°K and 5.34°K. We found that the critical behaviors of the mixed crystals can be explained by assuming that the Ni and Co spins behave like Ising spins randomly distributed on a square lattice, and interact through exchange interactions which do not change with concentrations. We have applied the annealed Ising, the annealed Bethe-Peierls-Weiss (BPW), the quenched BPW models to this system. All three theoretical models can be solved exactly, and have varying degrees of physical validity. The quenched models assume the distribution function of the exchange interactions to be fixed, while the annealed models allow this distribution to come into equilibrium with the spins at each temperature. We found that the T_N vs. concentration diagram can be fairly well explained by both the annealed Ising and BPW models. However, the annealed BPW does not fit the experimental specific heat data as well as the quenched BPW model, while the latter predicts critical temperatures which are too high. In all cases, the specific heat data near the critical region agree well with the annealed Ising model. We present semi-quantitative arguments to support the view that the quantitative differences between the quenched and annealed BPW models are due to some peculiarity in the BPW approximation itself, and that it is unlikely that an exact solution of the quenched Ising model will exhibit significant differences from the annealed Ising model.

The low temperature specific heats are also found to follow a T^3 dependence between $0.5T/T_N$ and $0.75T/T_N$. This is presumably due to spin wave behavior. We also present some preliminary magnetic phase diagram data. We discuss these features qualitatively and suggest directions in which further theoretical and experimental investigations on $Co_xNi_{1-x}Cl_2 \cdot 6H_2O$ can be carried out.

ACKNOWLEDGMENTS

I would like to express my sincere thanks to my thesis advisor, Dr. H. Forstat, for having suggested the topic of this research, and for his advice and encouragement, without which this project might never have been completed. His understanding and patience in attempting to teach me experimental physics are greatly appreciated. I would also like to thank Dr. M. F. Thorpe for many fruitful discussions about the theory of the annealed Ising model. To Dr. T. A. Kaplan I owe many valuable comments which help clarify some of my ideas about the physics of random magnetic systems. The financial supports of the Air Force Office of Scientific Research and of the Physics Department, during the early and later stages of this work, are gratefully acknowledged.

Finally, to my parents who have always given me so much, and asked for so little in return, I dedicate this thesis.

TABLE OF CONTENTS

LIST OF TABLES

LIST OF FIGURES

Figure Page

Introduction

In recent years, there has been an upsurge of interest in random magnetic systems. As can be expected, such systems present interesting experimental and theoretical problems. The present work is a calorimetric study of random mixtures of two antiferromagnetic insulators.

$NiCl_2 \cdot 6H_2O$ and $CoCl_2 \cdot 6H_2O$ have similar molecular weights, formation energies and crystallographic structures. Furthermore, the lattice constants are nearly equal. Therefore, one can expect the two salts to form a complete series of solid solutions and indeed, the compositional phase diagram has been studied as early as 1928 by Osaka et al.[1] The magnetic behaviors of both salts have been extensively investigated. Calorimetric studies indicate Néel temperatures in the liquid He^4 region (2.29°K for $CoCl_2 \cdot 6H_2O$ with effective spin $S = 1/2$ and 5.34°K for $NiCl_2 \cdot 6H_2O$ with effective spin $S' = 1$). Magneto caloric and susceptibility studies establish that both salts can be described as anisotropic antiferromagnets although the source of the anisotropy may differ in each salt.

Using a standard He^4 calorimeter, we have established the Néel temperature vs. concentration diagram for a wide range of compositions. To explain this phase diagram, we have made the following assumptions:

a) the Ni^{++} and Co^{++} ions are randomly distributed on a square lattice.

b) the exchange constants between like ions retain their "pure" values in the mixed lattice.

Thus, the only adjustable parameter is the exchange constant between unlike ions. We have taken this exchange constant to be antiferromagnetic. Further, it has been possible to carry out a detailed comparison between experimental and theoretical specific heats. Among the theoretical models considered, the one which appears to explain the phase diagram and fit the experimental specific heats the best is the "annealed Ising" model. However, these apparent agreements raise almost as many questions as they answer. We will attempt to address those questions in the course of this work.

As far as their magnetic behaviors are concerned, $NiCl_2 \cdot 6H_2O$ and $CoCl_2 \cdot 6H_2O$ exhibit qualitatively similar magnetic phase diagrams. However, the anisotropy energies in $NiCl_2 \cdot 6H_2O$ are significantly higher than those of $CoCl_2 \cdot 6H_2O$. Also, the easy axes are oriented differently. Therefore, one might expect an extensive study of the magnetic phase diagrams of mixed crystals to reveal some interesting aspects. Unfortunately, we have not been able to grow single mixed crystals of sufficient quality to warrant such an investigation. We will present preliminary magnetic phase diagrams for two concentrations and attempt to discuss them qualitatively.

This work will be divided into three sections:

-Section I sets forth the theoretical models used.

-Section II describes the experimental apparatus.

-Section III contains a discussion of the results and offers suggestions for further work.

I. Theory

A. General considerations

Consider a lattice of N magnetic ions with spins S_i, whose magnetic behaviors can be described by a Heisenberg Hamiltonian,

$$\mathcal{H} = - \sum_{\{i,j\}} J_{ij} \vec{S}_i \cdot \vec{S}_j \tag{1.1}$$

Following Brout,[2] we distinguish between two kinds of thermodynamic behaviors if the J_{ij}'s are allowed to vary randomly.

1.) Quenched model

The positions of the ions are "frozen in", i.e. they are not allowed to change with temperature. For a definite ionic configuration specified by $(\vec{x}_i, \vec{x}_j, \ldots)$, one writes the Hamiltonian explicitly as

$$\mathcal{H}(\vec{x}_i,\vec{x}_j,\ldots) = - \sum_{\{i,j\}} J_{ij}(\vec{x}_i,\vec{x}_j\ldots)\vec{S}_i\cdot\vec{S}_j \tag{1.2}$$

and the partition function as

$$Z(\vec{x}_i,\vec{x}_j,\ldots) = \sum_{\{\vec{s}_i\}} e^{-\beta\mathcal{H}} \tag{1.3}$$

with

$\beta = 1/kT$

k = Boltzmann's constant

T = temperature

In (1.3), the summation is carried out over all possible spin states. For the particular ionic configuration under consideration, the average energy can be claculated in the usual way as

$$U(\vec{x}_i,\vec{x}_j,\ldots) = -\frac{\partial \ln Z}{\partial\beta} \tag{1.4}$$

The macroscopic energy $\bar{U}$ cannot depend on a particular ionic configuration, but only on such parameters as the concentrations of the ions. In other words, the observable $\bar{U}$ must be an average of the $U(\vec{x}_i,\vec{x}_j,\ldots)$ over all spatial configurations, i.e.

$$\bar{U} = \langle\langle U(\vec{x}_i,\vec{x}_j\ldots)\rangle\rangle \tag{1.5}$$

or

$$\bar{U} = \langle\langle -\frac{\partial \ln Z}{\partial\beta}\rangle\rangle = -\frac{\partial}{\partial\beta}\langle\langle \ln Z(\vec{x}_i,\vec{x}_j,\ldots)\rangle\rangle \tag{1.6}$$

Here, the double bracket denotes configurational averaging. From (1.6) one sees that all thermodynamic functions can be obtained from $\langle\langle \ln Z(\vec{x}_i,\vec{x}_j\ldots)\rangle\rangle$.

As far as mixtures of magnetic insulators are concerned, the quenched model can certainly be realized in practice.

2. Annealed model

In this model, one allows the probability distribution of the J_{ij}'s to come to equilibrium with the spins at each temperature. In much the same way one lets the number of particles vary in the grand canonical ensemble. One is thus led to introduce a grand partition function

$$\Xi = \sum_{\{\vec{s}_i\}}\sum_{\{f_n\}} e^{-\beta\mathcal{H}} e^{-\beta\xi_n f_n} \tag{1.7}$$

where

ξ_n = chemical potential associated with a possible value J_n of J_{ij}

f_n = thermodynamic variable conjugate to ξ_n

The average energy $\bar{U}$ is now given by

$$\bar{U} = - \frac{\partial \ln \Xi}{\partial \beta} \tag{1.8}$$

With the ξ_n's determined so as to produce the average distribution P(J), which is assumed independent of temperature.

In (1.7) the summation over the spins and the f_n's are carried out simultaneously. Looking at (1.7), one can say that, roughly speaking, the annealed model amounts to averaging the partition function Z over the probability distribution of the J_{ij}'s, while in the quenched model, this averaging is done for lnZ. As one may imagine, the former averaging is mathematically much more tractable.

The nature of "f_n" may seem obscure at the moment. It can be related to the probability for a particular exchange interaction J_n to occur. More details will be provided in part C.

B. Mean field models

In almost all dissertations on magnetic insulators, one usually begins with some sort of mean field approximation. Let us follow this tradition by considering two random mean field models.

1. Virtual crystal approximation

In the mean field approximation one replaces the Heisenberg Hamiltonian (1.1) by a sum of single spin Hamiltonians, i.e.

$$\mathcal{H}_{mf} = \sum_{i} \mathcal{H}_i \tag{1.9}$$

where

$$\mathcal{H}_i = -\vec{S}_i \cdot \sum_{j} J_{ij} \langle \vec{S}_j \rangle \tag{1.10}$$

The bracket denotes thermal average.

For definitiveness, let us assume all J_{ij} 0, two kinds of magnetic ions A and B (with spins S_A and S_B), and nearest neighbor interactions only. Thus, we introduce three kinds of exchange interactions: J_{AA}, J_{AB}, J_{BB}. Further, assume the presences of small anisotropy energies which orient all spins in the same direction, in the ordered state. In the following, we can then drop all vector notations.

Consider an A ion surrounded by z nearest neighbors. From (1.10), one sees that the effective field acting on ion A is given by

$$H_A = [J_{AA}\, n_A\, \sigma_A + J_{AB}\, n_B\, \sigma_B] \,/\, g_A \mu \tag{1.11}$$

Similarly

$$H_B = [J_{AB}\, n_A\, \sigma_A + J_{BB}\, n_B\, \sigma_B] \,/\, g_B \mu \tag{1.12}$$

Here

$g_A(g_B)$ = gyromagnetic ratio of ion A(B) along the magnetization direction

μ = Bohr magneton

$n_A(n_B)$ = number of nearest neighbors of type A(B)

$\sigma_A = \langle S_A \rangle \qquad \sigma_B = \langle S_B \rangle$

Let p and q be the concentrations of ions A and B respectively.

We have

$$n_A + n_B = z \tag{1.13}$$

$$p + q = 1 \tag{1.14}$$

The virtual crystal approximation consists in setting

$$n_A = zp \tag{1.15}$$

$$n_B = zq \tag{1.16}$$

The mean field consistency conditions become

$$\sigma_A = S_A \, B_{S_A} \, (x_A) \tag{1.17}$$

$$\sigma_B = S_B \, B_{S_B} \, (x_B) \tag{1.18}$$

where

$$\begin{aligned} B_S\,(x) &= \text{the Brillouin function} \\ &= \frac{2S+1}{2S} \coth \frac{2S+1}{2S}\, x - \frac{1}{2S} \coth \frac{x}{2S} \end{aligned} \tag{1.19}$$

$$x_A = \frac{S_A g_A \mu H_A}{kT} \tag{1.20}$$

$$x_B = \frac{S_B g_B \mu H_B}{kT} \tag{1.21}$$

The system of equations (1.17) and (1.18) possesses non zero solutions only below a critical temperature T_c. To find T_c, expand the right hand sides of (1.17) and (1.18) around $\sigma_A = \sigma_B = 0$. Using the well known Taylor series

$$B_S(x) = \frac{S+1}{3S} + 0(x^3) \tag{1.22}$$

these expansions read

$$\sigma_A = \frac{S_A(S_A + 1)}{3kT} \left[z(pJ_{AA}\,\sigma_A + qJ_{AB}\,\sigma_B) \right] \qquad (1.23)$$

$$\sigma_B = \frac{S_B(S_B + 1)}{3kT} \left[z(pJ_{AB}\,\sigma_A + qJ_{BB}\,\sigma_B) \right] \qquad (1.24)$$

Using the mean field expressions for the critical temperatures of the pure systems

$$T_A = \frac{z\ S_A(S_A + 1)J_{AA}}{3k} \qquad T_B = \frac{z\ S_B(S_B + 1)J_{BB}}{3k} \qquad (1.25)$$

We can rewrite (1.23) and (1.24) as a homogeneous linear system

$$\left(p - \frac{T}{T_A} \right)\sigma_A + q\,\frac{J_{AB}}{J_{AA}}\,\sigma_B = 0 \qquad (1.26)$$

$$p\,\frac{J_{AB}}{J_{BB}}\,\sigma_A + \left(q - \frac{T}{T_B} \right)\sigma_B = 0 \qquad (1.27)$$

To get a non-zero solution the determinant should vanish. This condition leads to a quadratic equation in T.

$$T^2 - (pT_A + qT_B)T + T_A\,T_B\,pq\,(1 - \frac{J_{AB}^2}{J_{AA}J_{BB}}) = 0 \qquad (1.28)$$

The positive solution T_c is given by

$$T_c = \frac{1}{2} \left[(pT_A + qT_B) + \sqrt{(pT_A - qT_B)^2 + 4pq\ T_A T_B \frac{J_{AB}^2}{J_{AA}J_{BB}}} \right] \qquad (1.29)$$

(1.29) gives the critical temperature vs. concentration in this approximation. Note that when $J_{AB}^2 = J_{AA}J_{BB}$, (1.29) reduces to

$$T_c = pT_A + qT_B \tag{1.30}$$

and the T_c vs. p curve becomes a straight line.

2. Quenched mean field model

The virtual crystal assumption may appear somewhat arbitrary. It certainly ignores fluctuations in the local surroundings of an ion. In the hope of producing a more consistent (if not better) approximation, let us follow the procedure outlined in part A for quenched random models. In this case, the configurational averaging of lnZ can be carried out in a simple manner.

Assume that the ions are distributed completely randomly on the lattice. The probability for a lattice site to be accupied by an A ion is simply p = concentration of A ions. The probability that this ion is surrounded by n_A and n_B nearest neighbors of types A and B is then $\frac{z!}{n_A!n_B!} p^{n_A}q^{n_B}$.

In other words, if we let

$P_A(n_A,n_B)$ = probability of occurrence of a cluster with an A ion at the center surrounded by n_A A ions and n_B B ions

Then

$$P_A(n_A,n_B) = p\ w(n_A,n_B) \tag{1.31}$$

with

$$w(n_A,n_B) = \frac{z!}{n_A!n_B!}\ p^{n_A}q^{n_B} \tag{1.32}$$

The partition function associated with this particular cluster will be denoted by Z_A

Similarly

$$P_B(n_A,n_B) = qw(n_A,n_B) \tag{1.33}$$

with associated partition function Z_B

The configurationally averaged partition function Z is given by

$$\begin{aligned} \ln Z &= \sum_{n_A=0}^{z} P_A(n_A,n_B)\ \ln Z_A + \sum_{n_A=0}^{z} P_B(n_A,n_B)\ \ln Z_B \\ &= p\sum_{n_A=0}^{z} w(n_A,n_B)\ \ln Z_A + q\sum_{n_A=0}^{z} w(n_A,n_B)\ \ln Z_B \end{aligned} \tag{1.34}$$

The explicit expressions for Z_A and Z_B are

$$Z_A = \sinh\left(\frac{2S_A+1}{2S_A}\ x_A\right)\Big/ \sinh\left(\frac{x_A}{2S_A}\right) \tag{1.35}$$

$$Z_B = \sinh\left(\frac{2S_B+1}{2S_B}\ x_B\right)\Big/ \sinh\left(\frac{x_B}{2S_B}\right) \tag{1.36}$$

with x_A and x_B defined earlier [equations (1.20) and (1.21)].

Just as for the pure lattices, the average spins σ_A and σ_B are calculated as

$$\sigma_A = S_A\frac{\partial \ln Z}{\partial x_A} = pS_A\sum w(n_A,n_B)\ \frac{\partial \ln Z_A}{\partial x_A} = pS_A\sum w(n_A,n_B)B_{SA}(x_A) \tag{1.37}$$

$$\sigma_B = S_B \frac{\partial \ln Z}{\partial x_B} = qS_B \sum w(n_A,n_B) \frac{\partial \ln Z_B}{\partial x_B} = qS_B \sum w(n_A,n_B) B_{S_B}(x_B) \tag{1.38}$$

Expand the Brillouin functions around $\sigma_A = \sigma_B = 0$ to get

$$\sigma_A = \frac{pS_A(S_A+1)}{3kT} \sum w(n_A,n_B)\ [n_A J_{AA} \sigma_A + n_B J_{AB} \sigma_B] \tag{1.39}$$

$$\sigma_B = \frac{qS_B(S_B+1)}{3kT} \sum w(n_A,n_B)\ [n_A J_{AB} \sigma_A + n_B J_{BB} \sigma_B] \tag{1.40}$$

Now

$$\sum w(n_A,n_B) n_A = \sum_{n_A=0}^{z} \frac{z!}{n_A! n_B!}\ p^{nA} q^{nB} n_A = zp \tag{1.41}$$

$$\sum w(n_A,n_B) n_B = \sum_{n_A=0}^{z} \frac{z!}{n_A! n_B!}\ p^{nA} q^{nB} n_B = zq \tag{1.42}$$

Expressing J_{AA}, J_{BB} in terms of T_A and T_B, we obtain

$$\left(p^2 - \frac{T}{T_A}\right)\sigma_A + pq\,\frac{J_{AB}}{J_{AA}}\,\sigma_B = 0 \tag{1.43}$$

$$pq\,\frac{J_{AB}}{J_{BB}}\,\sigma_A + \left(q^2 - \frac{T}{T_B}\right)\sigma_B = 0 \tag{1.44}$$

Comparing (1.44), (1.43) with (1.27) and (1.26) one can immediately write down the equation for the T_c-p diagram as

$$T_c = \frac{1}{2}\left[(p^2 T_A + q^2 T_B) + \sqrt{(p^2 T_A - q^2 T_B)^2 + 4p^2 q^2 T_A T_B \frac{J_{AB}^2}{J_{AA} J_{BB}}}\right] \tag{1.45}$$

Thus, as far as the T_c-p diagram is concerned, the quenched mean field model simply amounts to substituting p^2 and q^2 for p and q in the virtual crystal approximation. From (1.41) and (1.42), one also sees that it is possible to obtain the virtual crystal approximation by letting

$$P_A(n_A,n_B) = P_B(n_A,n_B) = w(n_A,n_B) \tag{1.46}$$

which is certainly a rough way of doing configurational averaging.

So far, we have considered only the ferromagnetic case. In general, the zero field thermodynamic behavior of an antiferromagnet is identical to that of the corresponding ferromagnet, provided the antiferromagnetic lattice can be subdivided into two sublattices [called "up" and "down" sublattices], such that the nearest neighbors of an "up" spin belong to the "down" sublattice, and vice versa. One can verify this equivalence directly by noting that the effective field acting on an A spin which is "up" should be written as

$$H_A = [J_{AA}n_A\sigma_A(\text{down}) + J_{AB}n_B\sigma_B(\text{down})]/g_A\mu \tag{1.47}$$

With all exchange constants negative, one readily verifies that by imposing new consistency conditions

$$\sigma_A(\text{up}) = -\sigma_A(\text{down}) \tag{1.48}$$

$$\sigma_B(\text{up}) = -\sigma_B(\text{down}) \tag{1.49}$$

the same T_c-p diagram is obtained as before. For zero external magnetic field, (1.48) and (1.49) certainly appear reasonable. As is also well known,[3] a two sublattice division is possible for simple crystallographic structures, such as the simple cubic and square lattices.

C. Annealed Ising model

So far we have considered only isotropic Heisenberg interactions. Since S = 1/2 for the Co ions and both pure crystals exhibit magnetic anisotropy, it seems natural to turn to a random Ising model as the next approximation. For mixtures of magnetic insulators one would like to try a quenched random Ising model. However, except for the one dimensional case, the quenched model is beset with considerable mathematical difficulties. The annealed Ising model turns out to have a simpler mathematical structure. Basically, it can be related to the regular Ising model, for which exact solutions are available in one and two dimensions. The following development closely follows Thorpe and Beeman.[4] The basic ideas behind the annealed Ising model have been discussed earlier in the literature.[5,6] But ref. 4 has the merit of clearly setting forth a general approach to the problem.

1. Relation between the annealed and regular Ising models

The most general Ising Hamiltonian can be written as

$$H = - \sum_{<mn>} J_{mn} \sigma_m \sigma_n \qquad (1.50)$$

with spin variables

$$\sigma_m, \sigma_n = \pm 1$$

Suppose the J_{mn}'s can take on a set of discrete values J_1, J_2, ...J_i, ...J_n. With each J_i associate a chemical potential ξ_i.

The extended Hamiltonian $\mathcal{H}$ can then be written as a sum of bond Hamiltonians

$$\mathcal{H} = \sum_{<mn>} \mathcal{H}_{mn} \tag{1.51}$$

where, for example

$$\mathcal{H}_{12} = -\sum_{i=1}^{n} J_i f_i \, \sigma_1 \sigma_2 - \sum_{i} \xi_i f_i \tag{1.52}$$

With $f_i = 1$ if $J_{12} = J_i$; 0 otherwise.
Note that f_i can be considered as a thermodynamical variable conjugate to ξ_i. To have a single exchange interaction associated with each bond, the f_i should satisfy the condition

$$\sum_{i=1}^{n} f_i = 1 \tag{1.53}$$

This makes

$$\sum_{i} \langle f_i \rangle = 1 \tag{1.54}$$

The bracket < > denotes thermal average. $\langle f_i \rangle$ can be interpreted as a probability for a bond to have the interaction J_i. The requirement that $\langle f_i \rangle$ be temperature independent will determine ξ_i.

The grand partition function Ξ involves a summation over both the f_i and the spins σ_j

$$\Xi = \sum_{\{\sigma_j\}} \sum_{\{f_i\}} e^{-\beta \mathcal{H}} \tag{1.55}$$

Do the sum over the f_i first. Since, the $\mathcal{H}_{mn}$ in (1.55) commute with one another, this sum reduces to a product of terms of the form.

$$\sum_{\{f_i\}} e^{-\beta \mathcal{H}_{mn}} = \sum_{i} \exp(\beta J_i \sigma_m \sigma_n + \beta \xi_i) \tag{1.56}$$

The next step consists in noting that the product $\sigma_m \sigma_n = \pm 1$. One can then rewrite (1.55) as

$$\sum_{i} \exp(\beta J_i \sigma_m \sigma_n + \beta \xi_i) = A_e{}^{K\sigma_m\sigma_n} \tag{1.57}$$

Explicitly

for $\sigma_m \sigma_n = 1$ $$\sum_i \exp(\beta J_i + \beta \xi_i) = Ae^K \tag{1.58}$$

$\sigma_m \sigma_n = -1$ $$\sum_i \exp(-\beta J_i + \beta \xi_i) = Ae^{-K} \tag{1.59}$$

Combining (1.59) and (1.58) we find expressions for A and K

$$e^{2K} = \left[\sum_i e^{\beta(\xi_i + J_i)}\right] \Big/ \left[\sum_j e^{\beta(\xi_i - J_i)}\right] \tag{1.60}$$

$$A^2 = \left[\sum_i e^{\beta(\xi_i + J_i)}\right] \left[\sum_j e^{\beta(\xi_i - J_i)}\right] \tag{1.61}$$

Notice that K and A depend only on temperature T and the J_i, and not on the pair of spins σ_m, σ_n under consideration. Therefore, performing all the summations in (1.55), we get

$$\Xi = A^{N_B} \sum_{\{m,n\}} e^{K\sigma_m\sigma_n} = A^{N_B}\, Z(K) \tag{1.62}$$

where

N_B = total number of bonds in the lattice

$Z(K)$ = partition function of the regular Ising lattice

(1.61) tells us that the annealed Ising model at temperature T can be effectively related to a regular Ising model at a different temperature T', inversely proportional to K.

From now on, assume nearest neighbors interaction only. Then for a lattice of N spins, each one of which is surrounded by z nearest neighbors, we have $N_B = \frac{Nz}{2}$.

As mentioned earlier, $\langle f_i \rangle$ can be considered as the average probability for a bond to have the interaction J_i. It is calculated as follows

$$\langle f_i \rangle = \frac{2}{Nz}\frac{\partial \ln \Xi}{\partial(\beta \xi_i)} = \frac{\partial \ln A}{\partial \xi_i} + \frac{2}{Nz}\frac{\partial \ln Z}{\partial K}\frac{\partial K}{\partial \xi_i} \qquad (1.63)$$

or

$$\langle f_i \rangle = \frac{\partial \ln A}{\partial \xi_i} + \varepsilon(K)\frac{\partial K}{\partial \xi_i} \qquad (1.64)$$

where

$$\varepsilon(K) = \frac{2}{Nz}\frac{\partial \ln Z}{\partial K} = \langle \sigma_1 \sigma_2 \rangle$$ = nearest neighbor correlation function in the regular lattice

Using (1.61) and (1.60), one finds that (1.64) is equivalent to

$$\frac{e^{\beta(\xi_i + J_i)}}{\sum_j e^{\beta(\xi_j + J_j)}} = \frac{2\langle f_i \rangle}{[1+\epsilon(K)] + [1-\epsilon(K)]e^{2(K-\beta J_i)}} \qquad (1.65)$$

Sum over all i to obtain

$$\sum_i \frac{\langle f_i \rangle}{[1+\varepsilon(K)] + [1-\varepsilon(K)]e^{2(K-\beta J_i)}} = \frac{1}{2} \tag{1.66}$$

Using $\sum_i \langle f_i \rangle = 1$, one shows that (1.66) reduces to a more symmetrical form

$$\sum_i \frac{\langle f_i \rangle}{\coth(K-\beta J_i)-\varepsilon(K)} = 0 \tag{1.67}$$

Going over to a continuous probability distribution function P(J), (1.67) becomes

$$\int \frac{P(J)\, dJ}{\coth(K-\beta J)-\varepsilon(K)} = 0 \tag{1.68}$$

In summary, (1.68) allows us to calculate K as a function of temperature T, once P(J) has been specified. Incidentally, suppose we change all the signs of the J's without altering $P(|J|)$. From (1.59) we see that K simply becomes -K. Then (1.68) remains satisfied, provided $\varepsilon(K) = -\varepsilon(-K)$. In this case, there is complete equivalence between the ferromagnetic annealed Ising model and the antiferromagnetic one with the same P(J).

2. Specific heat of the annealed Ising model

One can proceed further and obtain general expressions for the average energy U and the magnetic specific heat C.

$$U = -\frac{Nz}{2} \sum_i J_i \langle f_i \sigma_1 \sigma_2 \rangle = \sum_i J_i \frac{\partial \ln \Xi}{\partial (\beta J_i)} \tag{1.69}$$

$$C = \frac{\partial U}{\partial T} \tag{1.70}$$

Combining (1.61), (1.60), (1.68) we derive

$$U = \frac{Nz}{2} \int \left\{ \frac{1 - \varepsilon \coth (K-\beta J)}{\coth (K- \beta J) - \varepsilon} \right\} J \; P(J) \; dJ \tag{1.71}$$

Further

$$C = \frac{Nk}{2} z \beta^2 \left\{ I_3 \left[1-\varepsilon^2 (K) \right] + I_2^{\,2} \left[I_1 - \left(1-\varepsilon^2 (K) - \frac{d\varepsilon}{dK} \right)^{-1} \right]^{-1} \right\} \tag{1.72}$$

With

$$I_1 = \int [\coth (K- \beta J) - \varepsilon(K)]^{-2} \; P(J) \; dJ \tag{1.73a}$$

$$I_2 = \int [\coth (K- \beta J) - \varepsilon(K)]^{-2} \operatorname{csch}^2(K- \beta J) P(J) \; dJ \tag{1.73b}$$

$$I_3 = \int [\coth (K- \beta J) - \varepsilon(K)]^{-2} \operatorname{csch}^2(K- \beta J) J^2 \; P(J) \; dJ \tag{1.73c}$$

Consider some special cases.

3. Annealed Ising chain

The one dimensional regular Ising model has first been solved by E. Ising.[7] For the nearest neighbor correlation function we have

$$\varepsilon(K) = \tanh K \tag{1.74}$$

Substituting (1.74) into (1.71) and (1.72), we find

$$U = -\frac{Nz}{2}\int J \tanh(\beta J)\, P(J)\, dJ \tag{1.75}$$

$$\frac{C}{Nk} = \frac{z}{2}\beta^2 \int J^2 \operatorname{sech}^2(\beta J)\, P(J)\, dJ \tag{1.76}$$

If we have two kinds of ions A and B randomly distributed on the chain with concentration p and q, and with interaction constants J_{AA}; J_{BB}; J_{AB}, a natural choice of P(J) might be

$$P(J) = p^2\delta(J-J_{AA}) + 2pq\,\delta(J-J_{AB}) + q^2\delta(J-J_{BB}) \tag{1.77}$$

where δ denotes a Dirac delta function.

To elaborate slightly, suppose we have N_A A ions and N_B B ions ($N_A + N_B = N$) which are randomly distributed on an infinite lattice. (1.77) is the bond distribution function which results in the limit $N \to \infty$, such that $\frac{N_A}{N} = p$ and $\frac{N_B}{N} = q$.

Substituting (1.77) into (1.76), the specific heat becomes

$$\frac{C}{Nk} = \frac{z}{2}\beta^2 \left[p^2 J_{AA}^2 \operatorname{sech}^2 \beta J_{AA} + 2pq J_{AB}^2 \operatorname{sech}^2 \beta J_{AB} + q^2 J_{BB}^2 \operatorname{sech}^2 \beta J_{BB}\right] \tag{1.78}$$

With z=2, the above agrees exactly with the heat capacity of the quenched Ising linear chain as calculated by Katsura and Matsubara[8].

So, in the one dimensional case, the annealed and quenched models for Ising spins are completely equivalent.

4. Annealed Ising square lattice

As is well known, the regular two-dimensional square Ising model has first been solved by Onsager.[9] He obtained the following expression for $\varepsilon(K)$

$$\varepsilon(K) = \coth 2K\left[\frac{1}{2} + \pi^{-1}\,(2\tanh^2 2K-1)\,F_1(k_1)\right] \qquad (1.79)$$

where

$$k_1 = 2\frac{\sinh 2K}{(\cosh 2K)^2} \qquad (1.80a)$$

$F_1(k)$ = complete elliptic integral of the first kind

$$F_1(k) = \int_0^{\pi/2} d\theta(1-k^2\sin^2\theta)^{-1/2} \qquad (1.80b)$$

(1.79) looks more formidable than it really is, since it turns out that $F_1(k)$ can be readily evaluated by computer.

A second order phase transition occurs when $\frac{d\varepsilon}{dK}$ diverges. This happens for $K_c = \frac{1}{2}\ln(1+\sqrt{2})$ and $\varepsilon_c = \frac{1}{\sqrt{2}}$.

Inserting those values of K_c and ε_c into (1.68) and assuming $P(J)$ given by (1.77), we obtain the critical temperature T_c vs. concentration diagram.

Further, using the full expression for $\varepsilon(K)$ and (1.68), K has been numerically calculated as a function of temperature T, by the standard Newton-Raphson method. (1.72) and (1.73) then give specific heat as a function of T.

These theoretical results will be compared with experimental data in chapter III.

Note that $\varepsilon(K)$ is an odd function of K. This ensures complete equivalence between the antiferromagnetic and ferromagnetic annealed square Ising lattices under zero magnetic field.

5. Correlations between bonds

At this point, it may be worthwhile to ask the question: to what extent does an annealed model approximate a quenched model which one expects to be much more physically realistic for mixtures of magnetic insulators? Within the framework of the annealed Ising model, it is possible to provide a partial answer to this question.

In the quenched model, the interaction constants are independently distributed on the lattice according to some probability function P(J) which does not change with temperature. The annealed model allows the interaction constants distribution to come into equilibrium with the spins at each temperature. This makes the interactions distribution fluctuate around some average distribution (which we have also called P(J)). One can also look at the situation from a different point of view.

Consider two pairs of spins: (σ_1, σ_2) and (σ_r, σ_{r+1}). Let f_i and f_j refer to the first and second pairs of spins respectively. The thermal average $\langle f_i f_j \rangle$ can be interpreted as $P(J_i, J_j)$ = joint probability for (σ_1, σ_2) and (σ_r, σ_{r+1}) to have interaction constants J_i and J_j respectively.

Thorpe[4] has shown that

$$\langle f_i f_j \rangle = \langle f_i \rangle \langle f_j \rangle \, (1 + c) \tag{1.81}$$

where

$$c = \frac{\langle \sigma_1 \sigma_2 \sigma_r \sigma_{r+1} \rangle - \varepsilon^2(K)}{[\coth (K-\beta J_i) - \varepsilon(K)][\coth (K-\beta J_j) - \varepsilon(K)]} \tag{1.82}$$

In the quenched model, $P(J_1,J_2) = P(J_1) \cdot P(J_2)$. So from (1.81) one can say that the annealing process has destroyed the "true" randomness or statistical independence of the bonds. For the Ising chain, $\langle \sigma_1 \sigma_2 \sigma_r \sigma_{r+1} \rangle = \langle \sigma_1 \sigma_2 \rangle \langle \sigma_r \sigma_{r+1} \rangle = \varepsilon^2$ so that $c = 0$. This helps explain why the annealed and quenched Ising chains are completely equivalent.

Now, let $f_i = f_j$ and $\sigma_1 = \sigma_r$; $\sigma_2 = \sigma_{r+1}$ in (1.81) and (1.82). We obtain

$$c = \frac{\langle f_i^2 \rangle - \langle f_i \rangle^2}{\langle f_i \rangle^2} = \frac{1 - \varepsilon^2(K)}{[\coth(K-\beta J_i) - \varepsilon(K)]^2} \tag{1.83}$$

since $\sigma_1^2 = \sigma_2^2 = 1$

c in (1.83) can be considered as the fractional mean square deviation of the bond occupation probability for J_i from its average value $\langle f_i \rangle$. The magnitude of c is then a rough measure of the extent to which the annealed and quenched models differ from one another. One should not take this too literally, however. For example, in the linear chain, (1.83) becomes small but does not vanish, although the annealed linear chain is equivalent to the quenched one.

It turns out that there is one non trivial theoretical model where one can make a direct comparison between the annealed and quenched approaches. This is the Bethe-Peierls-Weiss model, which we will consider in the next section.

D. BPW model

The BPW approximation was first applied to the Ising model by Bethe[10] and Peierls.[11] Later, Weiss[12] extended it to the Heisenberg model. Let us first review the BPW treatment of the regular Ising lattice.

1. Regular Ising lattice

Consider a cluster consisting of a central spin with its z nearest neighbors. The BPW approximation treats the interactions within the cluster exactly, and replaces the effects of the outside spins by an effective field acting on the nearest neighbors. Explicitly, the cluster Hamiltonian can be written as

$$\mathcal{H}_{cl} = -J \sum_{n=1}^{z} \sigma_o \sigma_n - g\,\mu H\,\sigma_o - g\,\mu(H+H')\sum_{n=1}^{z} \sigma_n \qquad (1.84)$$

where

σ_o = central spin = ± 1

σ_n = nearest neighbor spins = ± 1

H = external magnetic field

H' = effective field due to outside spins.

g = gyromagnetic ratio along the magnetization direction.

J = interaction constant

We have assumed H and H' to be directed along the magnetization direction. We can then drop all vector notation.

The partition function of the cluster $Z_{cl} = \mathrm{Tr}\, e^{-\beta \mathcal{H}_{cl}}$ can be conveniently divided into two parts

$$Z_{cl} = Z_+ + Z_- \tag{1.85}$$

Z_+ corresponds to $\sigma_0 = 1$

Explicitly

$$Z_+ = \sum_{\sigma_1=\pm1} \cdots\cdots \sum_{\sigma_z=\pm1} \exp[x + (x+L+K) \sum_{n=1}^{z} \sigma_n]$$

$$= e^x [2 \cosh (x+L+K)]^z \tag{1.86}$$

Similarly Z_- correponds to $\sigma_0 = -1$ and is given by

$$Z_- = e^{-x} [2 \cosh(x+L-K)]^z \tag{1.87}$$

Here

$x = \beta g \mu H$

$L = \beta g \mu H'$

$K = \beta J$

The average spins $<\sigma_0>$ and $<\sigma_n>$ can be calculated in terms of Z_{cl} as

$$< \sigma_0 > = \frac{\partial \ln Z_{cl}}{\partial x} \tag{1.88}$$

$$< \sigma_n > = \frac{1}{z} \frac{\partial \ln Z_{cl}}{\partial L} \tag{1.89}$$

We restrict ourselves to the case H = 0. (1.88) and (1.89) then simplify to

$$< \sigma_0 > = \frac{Z_+ - Z_-}{Z_{cl}} \tag{1.90}$$

$$\langle\sigma_n\rangle = \frac{[Z_+ \tanh(L+K) + Z_- \tanh(L-K)]}{Z_{c1}} \qquad (1.91)$$

Consider first the ferromagnetic case. The effective field is then found by imposing the consistency condition $\langle \sigma_0 \rangle = \langle \sigma_n \rangle$. This yields the following equation for H' (or L)

$$e^{2L} = \left[\frac{\cosh(L + K)}{\cosh(L - K)}\right]^{z-1} \qquad (1.92)$$

or, in a more symmetrical form

$$\tanh K \tanh L = \tanh [L/(z-1)] \qquad (1.93)$$

By expanding (1.93) as a Taylor series around L = 0 one finds that a non-zero solution exists for L below a critical temperature T_c given by

$$\tanh K_c = \tanh \frac{J}{kT_c} = \frac{1}{z-1} \qquad (1.94)$$

One can also calculate the nearest neighbor correlation

$$\varepsilon(K) = \langle \sigma_0 \sigma_n \rangle = \frac{1}{z} \frac{\partial \ln Z_{c1}}{\partial K} \qquad (1.95)$$

Combining (1.86), (1.87), (1.92), we find

$$\varepsilon(K) = 1 - \frac{2}{e^{2K}\cosh 2L + 1} \qquad (1.96)$$

For N spins, the total average energy U is then given by

$$U = - \frac{NzJ}{2} \varepsilon(K) \qquad (1.97)$$

and the specific heat

$$C = \frac{dU}{dT} = Nk \frac{zK^2}{2} \frac{d\varepsilon}{dK} \tag{1.98}$$

For $T \geq T_c$, $L = 0$ and (1.96) simplified to

$$\varepsilon(K) = \tanh K \tag{1.99}$$

which is identical to the $\varepsilon(K)$ of the Ising chain. For the two sublattice antiferromagnet, the consistency condition should now be $< \sigma_o > = - < \sigma_n >$. We then find $\varepsilon(K) = - \varepsilon(|K|)$ and the specific heat is exactly the same as in the ferromagnetic case.

Just as the mean field approximation, the BPW approximation gives a finite specific heat discontinuity at T_c. The main improvement over mean field is that BPW predicts a non-zero specific heat above T_c.

Finally, note that the BPW approximation becomes exact if the Ising spins are distributed on a pseudo lattice called the "Bethe" lattice. For details, see Katsura and Takizawa.[13]

2. Annealed Bethe lattice

We are now in a position to apply the annealed Ising formalism to the Bethe lattice. Recall that the transition temperature T_c is given by

$$\int \frac{P(J)dJ}{\coth\,(K_c-\beta_c J) - \varepsilon(K_c)} = 0 \tag{1.100}$$

As $\varepsilon(K_c) = \tanh K_c = \frac{1}{z-1}$, (1.100) reduces to

$$\int P(J)\,\tanh\,(\beta_c J)dJ = \frac{1}{z-1} \tag{1.101}$$

This result has been derived earlier by Matsubara.[14]

3. Quenched Bethe Lattice

Matsubara,[14] Katsura and Matsubara,[8] Eggarter[15] have investigated the quenched Bethe lattice using three fairly indirect approaches. We present here a simpler (but less rigorous) derivation, based on a straightforward configurational averaging of $\ln Z_{cl}$.

Just as for the quenched mean field model (section B.2), we can write

$$\langle\langle \ln Z_{cl} \rangle\rangle = p \sum_{n_A=0}^{z} w(n_A,n_B)\,\ln Z_A + q \sum_{n_A=0}^{z} w(n_A,n_B)\,\ln Z_B \tag{1.102}$$

where all the symbols have been defined in B.2.

Just as for the regular lattice, we find it convenient to split Z_A and Z_B into two parts Z_{A+}; Z_{A-}; Z_{B+}; Z_{B-} such that

$$Z_{A\pm} = e^{\pm x_{Ao}}\; 2^z \cosh^{n_A}[x_{A_n}+L_A \pm K_{AA}]\cosh^{n_B}[x_{B_n}+L_B \pm K_{AB}] \tag{1.103}$$

$$Z_{B\pm} = e^{\pm x_{Bo}}\; 2^z \cosh^{n_A}[x_{A_n} + L_A \pm K_{AB}]\cosh^{n_B}[x_{B_n} + L_B \pm K_{BB}] \tag{1.104}$$

where

$$x_{io} = \beta g_i \mu H = x_{in} \tag{1.105}$$

$$K_{ij} = \beta J_{ij}$$

$$L_i = \beta g_i \mu H_i'$$

$$i = A,B$$

Note that we have introduced two effective fields H_A', H_B' acting on nearest neighbor ions of type A and B respectively.

For the ferromagnetic case, H_A' and H_B' are determined by the consistency condition

$$<\sigma_{Ao}> = <\sigma_{An}> \tag{1.106}$$

$$<\sigma_{Bo}> = <\sigma_{Bn}> \tag{1.107}$$

where, for example

$$<\sigma_{Ao}> = \frac{\partial <<\ln Z_{cl}>>}{\partial x_{Ao}}, <\sigma_{An}> = \frac{1}{z}\frac{\partial <<\ln Z_{cl}>>}{\partial L_A} \tag{1.108}$$

The full expressions for (1.106) and (1.107) appear somewhat complicated. To first order in L_A, L_B they reduce to

$$pt_{AB}[(z-1)\{pt_{AA} + qt_{BB}\}-z]L_A$$
$$+ [1-zqt_{BB} + (z-1)q^2t_{BB}^2 + pq(z-1)t_{AB}^2]L_B = 0 \tag{1.109}$$

$$[1-zpt_{AA} + (z-1)p^2t_{AA}^2 + pq(z-1)t_{AB}^2]L_A$$
$$+ qt_{AB}[(z-1)\{pt_{AA} + qt_{BB}\}-z]L_B = 0 \tag{1.110}$$

where we have abbreviated

$t_{AA} = \tanh K_{AA}$ $t_{BB} = \tanh K_{BB}$ $t_{AB} = \tanh K_{AB}$

For non-trivial solutions to exist, the determinant of the above system should vanish, or

$$[1-zp^{t}{}_{AA}+(z-1)p^2t^2_{AA}+pq(z-1)t^2_{AB}][1-zqt_{BB}+(z-1)q^2t^2_{BB}+pq(z-1)t^2_{AB}]$$
$$-pqt^2_{AB}[(z-1)\ pt_{AA}+qt_{BB}\ -z]^2 = 0 \qquad (1.111)$$

(1.111) can be factorized into

$$[\{1-(z-1)pt_{AA}\}\ \{1-(z-1)qt_{BB}\}\ -\ (z-1)^2p^2q^2t^2_{AB}][(1-pt_{AA})(1-qt_{BB})$$
$$-pqt_{AB}] = 0 \qquad (1.112)$$

This is equivalent to

$$\{1-(z-1)pt_{AA}\}\ \{1-(z-1)qt_{BB}\}\ -(z-1)^2pqt^2_{AB} = 0 \qquad (1.113)$$

since the other term in brackets corresponds to $z = 2$ (linear chain) and has no non-trivial solution.

To sum up, (1.113) gives the T_c vs. concentration diagram for the quenched ferromagnetic Bethe lattice. As usual, for the two sublattice antiferromagnet, the consistency conditions should now be $<\sigma_{Ao}> = -<\sigma_{An}>$ and $<\sigma_{Bo}> = -<\sigma_{Bn}>$. This then yields the same T_c vs. p equation as in (1.113), except that now t_{AA} and t_{BB} should enter with their absolute values.

In chapter III, we will compare (1.113) with the annealed Bethe result (eq. 1.101). Right now, we can easily write down expressions for the specific heat above T_c.

Above T_c, since $\epsilon(K) = \tanh K$ the annealed Bethe lattice specific heat C_A reduces to the linear chain form [eq. 1.78], assuming P(J) given by (1.77).

To find the quenched Bethe lattice specific heat C_Q, one first finds the energy per bond $-\frac{1}{z}\frac{\partial <<\ln Z_{cl}>>}{\partial\beta}$. Since there are $\frac{Nz}{2}$ bonds the total energy U is then $-\frac{N}{2}\frac{\partial<<\ln Z_{cl}>>}{\partial\beta}$.

Finally, $C_Q = \frac{dU}{dT}$. Above T_c, $H_A' = H_B' = 0$ and one finds that C_Q reduces to (1.78). Therefore, above a certain temperature, we have $C_A = C_Q$ and the annealed and quenched Bethe lattices become equivalent.

Below T_c, C_A and C_Q must be evaluated numerically. The results will be presented in chapter III.

4. Quenched classical Heisenberg Bethe lattice

Finally, as an aside, one may mention the quenched classical Heisenberg BPW model, since the T_c vs. p diagram looks similar to (1.113). Assuming that the spins couple through a Heisenberg interaction and behave like classical vectors, Boubel et al.[16] [also Katsura[17]] have derived the following T_c vs. p diagram, within a quenched BPW approximation.

$$[1-(z-1)pL(\beta_c J_{AA})][1-(z-1)qL(\beta_c J_{BB})] - (z-1)^2 pqL^2(\beta_c J_{AB}) = 0 \tag{1.114}$$

where

$$L(x) = \coth x - \frac{1}{x} = \text{the Langevin function.} \tag{1.115}$$

II. Experimental Techniques

A. Experimental Apparatus

1. Dewar and calorimeter

The experimental apparatus consists of a pyrex dewar shown in Fig. 1 and a triple can calorimeter shown in Figs. 2 and 3. The dewar was made to specifications by H. S. Martin and Son (Evanston, Illinois) and has been described in details earlier.[18]

The fundamental problem in adiabatic calorimetry is to ensure good thermal isolation of the sample. In this case, the surroundings consist of a) the large He^4 bath at 4.2°K in which the calorimeter is immersed, b) a smaller volume of He^4 contained in a Helium can which is connected to the inner can where the sample is placed. Good thermal isolation can be achieved by ensuring that the sample is not in contact with the inner can, and by pumping on the inner and outer cans. The purpose of the Helium can is to allow temperatures lower than 4.2°K to be reached by pumping on a small volume of He^4.

To reduce heat leaks to the inner can, all pumping lines (including the leads line) are made of german silver. The Helium can and inner can are made of copper. The inner can pumping lines and leads line are partially surrounded by the He^4 in the Helium can. When they emerge from the end

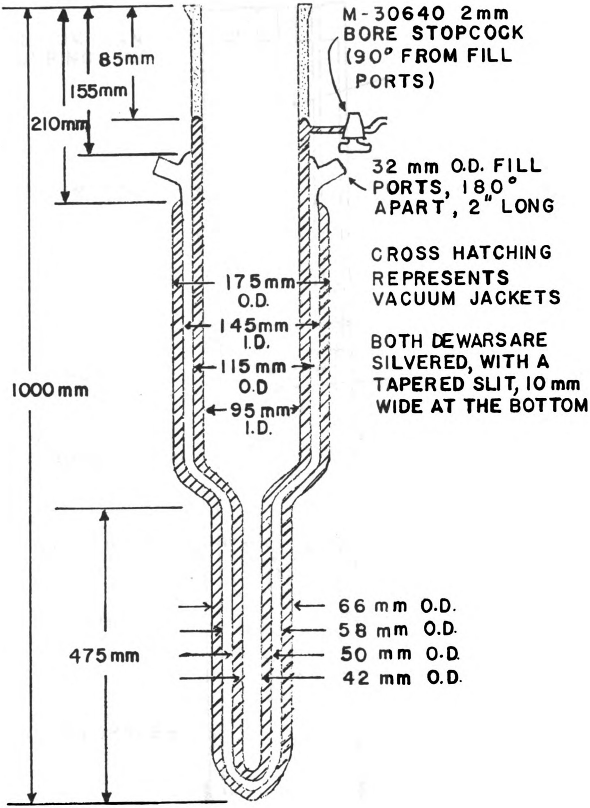

Figure 1. Pyrex helium dewar

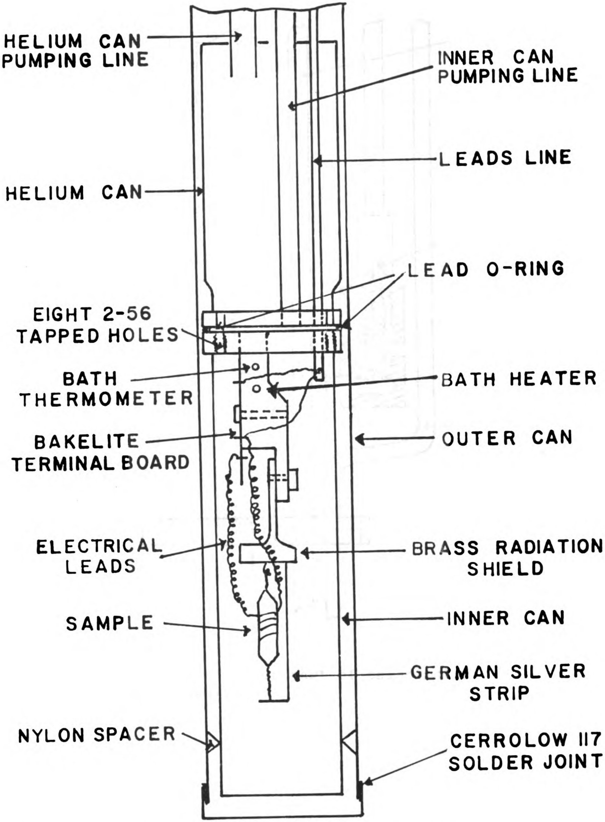

Figure 2. Cross section of body of calorimeter
(Not to scale)

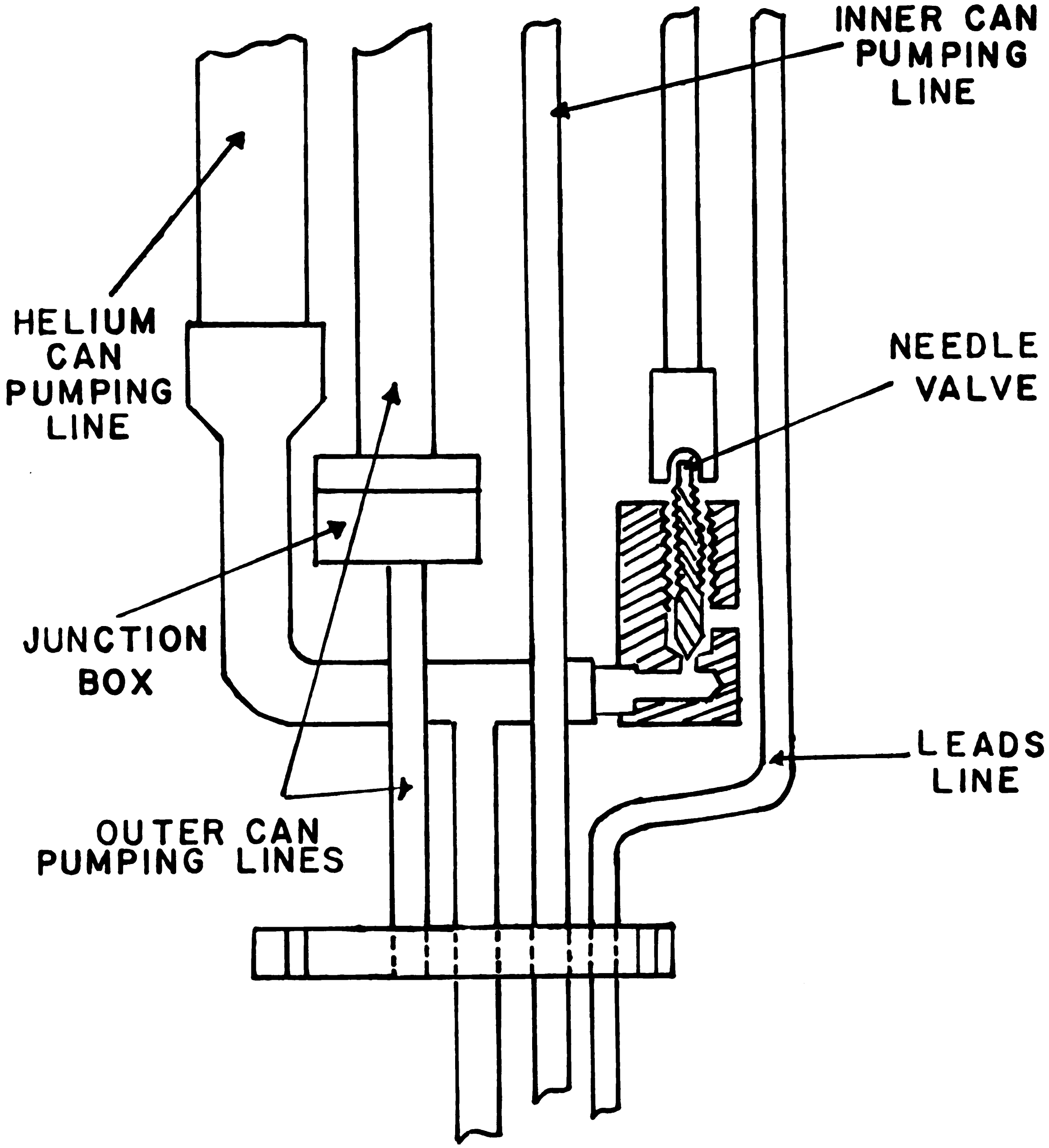

Figure 3. Side view of upper part of calorimeter
(Not to scale)

of the leads line, the electrical leads are glued to the bottom of the Helium can, thus ensuring good contact to a low temperature bath. The bottom of the outer can is made removable, to allow insertion of nylon spacers which further prevent thermal contact between inner and outer cans.

Heat radiation from parts of the calorimeter at room temperature constitutes another source of thermal leak. The standard remedy for this is to put right angle bends in pumping lines, wherever practical. As shown in Fig. 3, the lower part of the Helium can evacuation line is connected by a tee joint to the upper part, so that pumping on the Helium can is done through one side of the tee. The upper part of the outer can pumping line ends in a junction box, from which emerge two smaller pumping lines to the outer can. A brass radiation shield is attached to the bottom of the Helium can. Note however that the inner can pumping lines go straight down. Apparently, this produces no adverse effects during specific heat measurements. The brass shield has two clearance holes drilled through it, to allow insertion of a stainless steel shield enclosing the smaple. This limits the sizes of the samples, and does not seem to have any effects, in one way or another. This shield was removed in the last run.

This calorimeter is basically a modification of a rotator calorimeter designed by J. R. Ricks. Some of the early measurements were done with a calorimeter designed by N. D. Love and described in his thesis.[18] In Love's calorimeter, the inner can is simply soft soldered (with Cerrolow 117) to the bottom of the Helium can. But, due to repeated failures of the soldered joints, we have resorted to a "flange" system, whereby the sealing is ensured by a lead O ring between flanges on the inner and Helium cans. Details of the arrangement are depicted in Fig. 2.

2. Nylon sample holder

For experiments in a magnetic field, we use a nylon a C-clamp attached to a nylon support to prevent the sample from rotating under the influence of the field. This has been more fully described elsewhere.[19]

3. Vacuum Pumps

The pumping system is depicted schematically in Fig. 4. A Veeco EP 2AI 350W air cooled diffusion pump, which can attain a pressure of 10^{-6} mm Hg, is used for pumping on the inner and outer cans. A Welch Duo Seal pump serves as the forepump. Another such pump maintains vacuum on one arm of the U tube manometer, and is used to evacuate the McLeod gauge after a reading. A high capacity Stokes mechanical pump evacuates the dewar or pumps on the bath in the Helium can.

4. Pressure Gauges

Helium can pressures above 2.5cm Hg are measured with a mercury U tube manometer. Below that pressure, an oil-filled manometer is used to observe qualitatively the change in pressure with temperature during thermometer calibration, while the McLeod gauge measures the calibration pressure accurately.

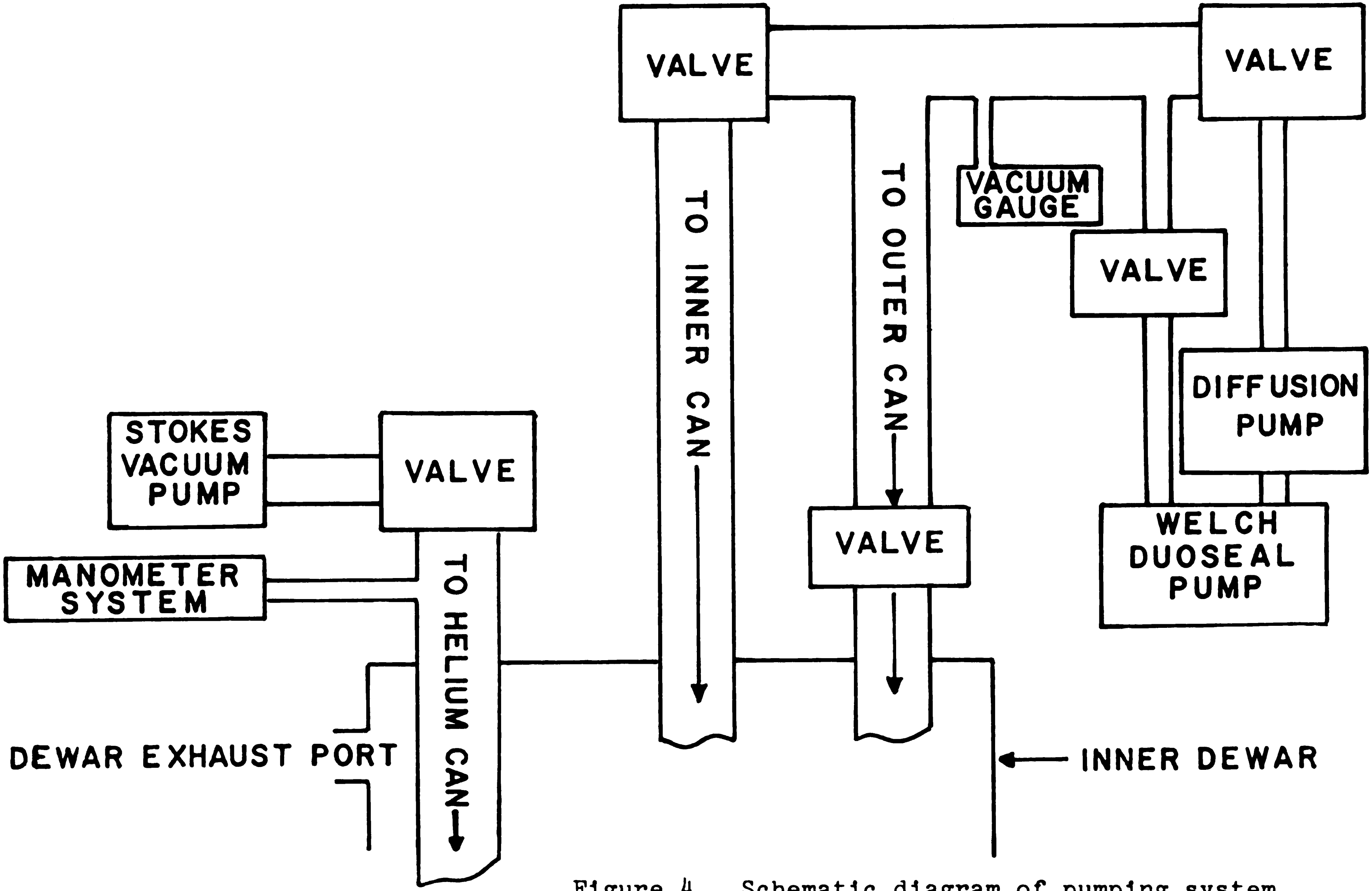

Figure 4. Schematic diagram of pumping system

A NRC 831 vacuum ionization gauge allows monitoring of the pressures in the inner and outer cans. Both the Helium can and the dewar have a U.S.G. gauge which gives rough readings (30 in vacuum to 15 P.S.I.)

5. Thermometer current supplies

Both sample and bath thermometers are 1/10 W, Allen Bradley carbon resistors, with room temperature resistances between 56 and 60 ohms. Their resistances are measured potentiometrically, using a standard four leads technique.

The sample and bath thermometer current supplies are diagrammed in Fig. 5. One can prove that the current I supplied to the load is given by

$$I = \frac{V_Z}{R_T} \qquad (2.1)$$

V_Z = reverse break down voltage of the Zener Diode

R_T = total resistance between the ground and the inverting input of the op amp.

With V_Z nearly equal to 6.2V, R_t has been adjusted to provide 1 microampere for the sample thermometer and 10 microamperes for the bath thermometer. Such a low current is needed to avoid self heating of the sample thermometer, while this problem is less critical for the bath thermometer.

6. Measuring Electronics

To measure the voltage across the sample thermometer, we use a Leeds and Northrup K-3 potentiometer. The off balance voltage from the potentiometer is amplified by a Leeds and Northrup 9835 B microvolt DC amplifier, and then "fed" to a

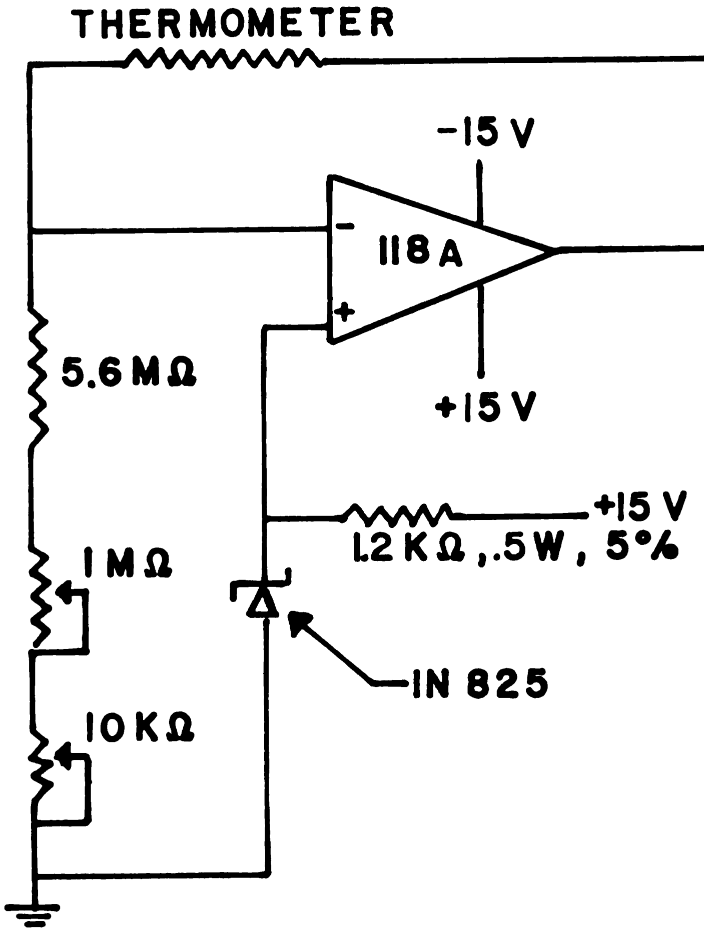

Figure 5. Sample thermometer current supply. Similar circuit for bath thermometer with all resistances divided by 10.

Leeds and Northrup dual pen Speedomax G recorder with a 5mv range card. The amplifier can be adjusted to give the amount of sensitivity desired. A similar system using the other pen of the recorder (with a 10 mv range card) monitors the bath thermometer voltage.

A filtered Lambda LM263 power supply (0 to 32v), in series with a set of variable resistors totaling 10 megohms provides the desired current through the sample heater. The latter can be turned on and off by a relay connected to an electronic timer (Veeder-Root Econoflex 71 2204) which is preset to run for a selected time interval. The relay connects an external resistor (of resistance 400 ohms, nearly equal to heater resistance) in place of the heater in the circuit, when the timer is off. This minimizes possible pulses from the measuring circuit.

A simple switch arrangement allows a Data Technology 323 digital voltmeter to measure either the heater voltage, or the voltage across a precision 10 ohm resistor in series with it. The latter voltage gives the current through the heater when it is on.

The above circuits are diagrammed in Fig. 6.

7. Magnet and Gauss-meter

The magnetic field is provided by a water cooled Harvey Wells 22KG magnet, with a Harvey Wells DC power supply providing up to 200 amperes at 80 volts. An electric motor with two reduction boxes can rotate the magnet at 2.8, 14, or 70 degrees per minute. Angles are measured using the 360 gear

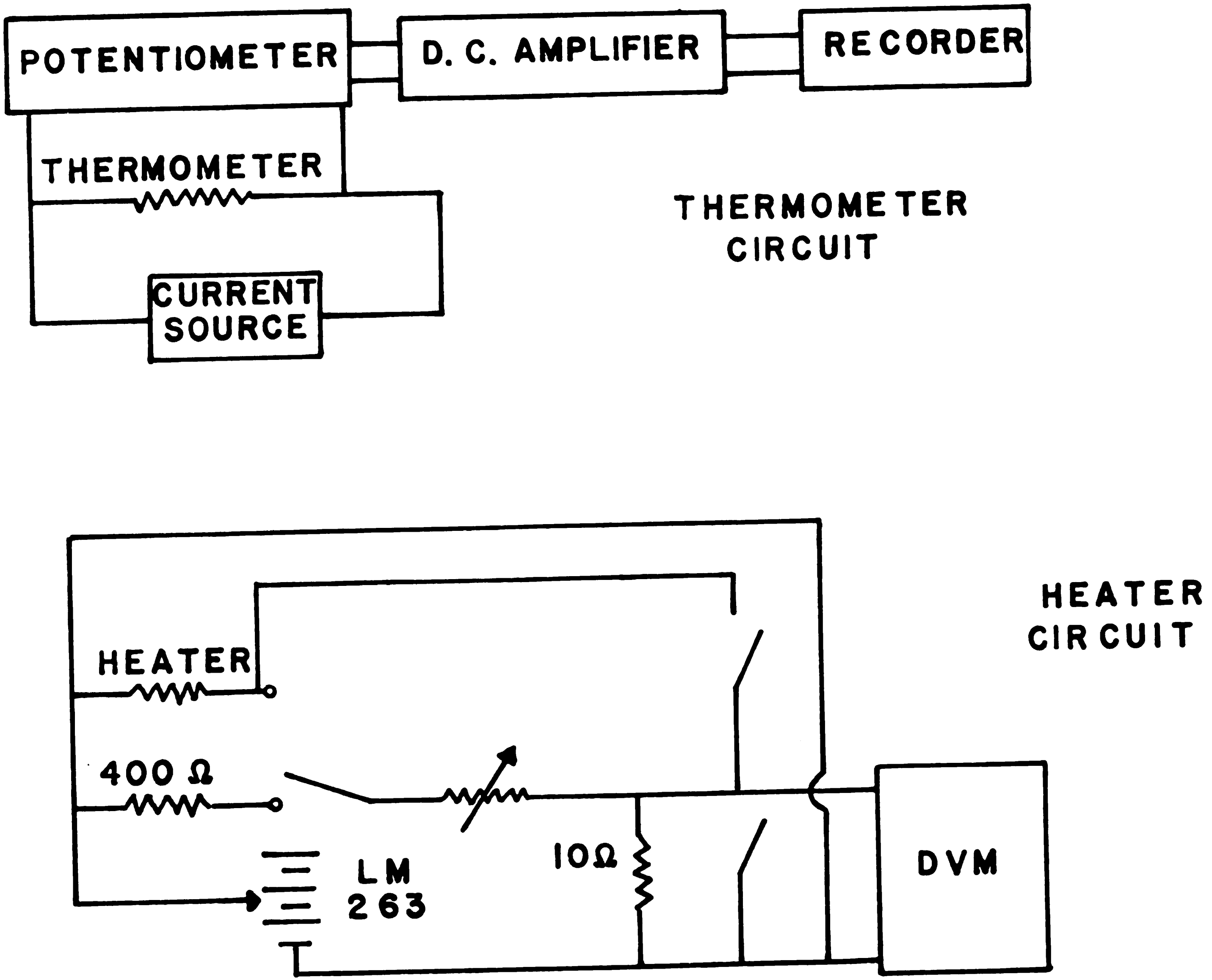

Figure 6. Diagram of electrical measuring circuit

teeth on the base of the magnet. A "home built" sweep circuit allows us to increase or decrease the field linearly at any desired rate up to 3000 gauss per minute. The value of the field is measured to within 10 gauss, with a Bell 660 digital gaussmeter connected to a Hall probe taped to one pole face of the magnet. Further details are provided in P. T. Bailey's thesis.[19]

B. Experimental Procedures

1. Sample preparation

The samples were grown from saturated aqueous solutions containing appropriate stoichiometric ratios of $NiCl_2 \cdot 6H_2O$ and $CoCl_2 \cdot 6H_2O$. The solutions were placed in a crystal growing room which maintained constant temperature and humidity conditions.

Most of the samples appeared polycrystalline. Their colors ranged from dark for high concentrations of Co to brownish for high concentrations of Ni. Fairly large samples (weighing from 1 to 1.5 g) were readily obtained from high Co concentration solutions. But growing sufficiently large samples from high Ni concentration solutions proved to be a slow process. In this case, the weights of the samples used ranged from 600 to 800 milligrams.

With the evaporation method, it appeared difficult to grow large single crystals, especially for high concentrations of Ni. From some high Co concentration solutions (ranging from 1:4 to 1:1 Ni:Co ratio), we have obtained a few reasonably large crystals which might qualify as single, in the sense that crystal faces can be distinguished and the interfacial angles corresponded to those in pure $CoCl_2 \cdot 6H_2O$. Unfortunately, we also saw irregularities on the crystal faces and they were not used in any experiments.

For magnetic phase diagram measurements, we used two crystals previously grown by P. T. Bailey from 1:1 ratio solutions. They appeared single.

When a sample had reached a sufficient size, it was removed from the solution and pieces were cut from it. Both samples and pieces were then refrigerated to prevent dehydration. After an experiment on the sample, the pieces were sent for chemical analysis. This procedure became necessary after it turned out that the chemical composition of the sample could differ by as much as 10% from the stoichiometric ratio of the solution from which it was grown.

The day before a run, the sample was taken out of the refrigerator and weighed. Afterwards, it was lightly coated with GE 1202 glyptal, and a 12½ inch length of 1.4 mil Evanohm* wire (with resistance nearly equal to 400 ohms) was wound as non-inductively as possible around it. A 1/10 watt Allen-Bradley carbon resistor, with nominal resistance between 56 and 60 ohms was then glued to the sample. This thermometer was further secured with two cotton threads wound

---

*Trademark of wire supplied by Wilbur B. Driver Co., Newark, N. J.

around the sample in opposite directions. The first thread sewed to attach the sample to a hook below the radiation shield, while the other thread was tied down to the base of a german silver strip connected to the bottom of the Helium can.

Both heater and thermometer carried a set of two leads at each end (making a total of eight formex coated manganin wires, each one 6 inches long, 3.1 mil in diameter, with a resistance of 15 ohms). Once the sample was initially secured with one cotton thread, the leads were soldered to the terminal board and checked for continuity. The sample was further tied down and a stainless steel shield slipped around it. A lead O ring was placed on the inner can flange which was then tightly bolted to the Helium can flange. To prevent damage to the O ring, care was taken to tighten the flanges uniformly. A similar procedure was followed to bolt the outer can into place. As a precautionary step, we next closed the inner can pumping line and leak detected the outer can with a helium mass spectrometer leak detector Veeco MSAB17. Past experience has indicated that when the outer can was leak tight, the same condition would also likely prevail for both the inner can and the leads line.

After leak detection proved satisfactory, the calorimeter was lowered into the dewar and tightly bolted to the upper flange of the dewar. The needle valve was then opened and both dewar and Helium can were evacuated with the Stokes mechanical pump, while the inner can and outer can pumping lines were closed. Next, the outer dewar was filled with liquid nitrogen. The dewar was then closed and up to 3 P.S.I. Helium gas introduced into the inner dewar. This allowed the calorimeter to cool down to liquid nitrogen temperature in a few hours. The liquid nitrogen needed periodic replenishing. This was automatically done by an electronic circuit designed around an IC 555 timer.

2. Helium transfer and temperature calibration

Early the next morning, the sample resistance was noted. This gave the first calibration point at liquid nitrogen temperature. Next, the inner and outer cans were evacuated. If no leaks existed, the pressures in both cans reached 2×10^{-4} mm Hg rather quickly. Approximatively 2mm Hg of Helium exchange gas was then introduced into both cans.

Before liquid Helium transfer, the needle valve and the pumping lines to the Helium can were closed and the inner dewar was vented. We could then proceed with Helium transfer, via a flexible transfer tube. Approximatively 3 P.S.I. Helium gas was introduced into the Helium container through a pressurizing port to force liquid Helium into the dewar. Once liquid was tranferred, both Helium can and sample started cooling. The liquid level could be checked through the dewar viewing slit with a flashlight.

After transferring, the needle valve was opened, to allow liquid into the Helium can. The Helium can pumping lines were also opened. For magnetic measurements, the magnet was then rolled into place and a suitable magnetic field applied. Otherwise, we proceeded directly to temperature calibration.

The first calibration point was taken near 4.2°K. To proceed to the next point, the needle valve was closed and the outer can pumped on to isolate the Helium and inner can from the 4.2°K bath. The Helium can temperature was lowered by regulating the pumping speed through a small valve. When the desired temperature range was reached, the pumping was stopped. The Helium bath would immediately reach thermal equilibrium, and at sufficiently high temperatures the sample should do likewise not too long afterwards. The values of the bath and sample thermometer resistances, and the vapor pressure in the Helium can as read from the U-tube manometer or the McLeod gauge were noted down. The pumping was then resumed and the whole process repeated, until we had obtained between 10-15 calibration points in the temperature region of interest. Below the Lambda point, it might prove difficult for the bath to reach equilibrium when the pumping stopped. Also, due to the decreased efficiency of heat transfer through Helium gas, it might take quite a while for the sample to reach thermal equilibrium. In this case, the bath temperature fluctuations could be observed on a moving coil galvanometer and the small valve "fine tuned", to allow both bath and sample to stay in thermal equilibrium long enough for accurate readings to be taken.

3. Specific heat measurements

After the last calibration point, the small valve was left open, the outer can closed, and the inner can evacuated to isolate the sample. When the inner can pressure reached the 10^{-5} mm Hg range, the outer can was also evacuated. We would now be ready to take specific data.

In principle, a specific heat measurement consists in supplying a known quantity of heat to the sample and determining the initial and final temperatures. The sample temperature should remain stable before and after the heating period. In the present calorimeter, this could not be achieved since heat leaks due to radiation and thermal conducion down electrical leads could not be completely eliminated. To substract this background heat, we applied the standard procedure of extrapolating the "before" and "after" recorder traces back to the middle of the heating period, as depicted in Fig. 7. The extrapolated points C, D were then considered as corresponding to the true initial and final temperatures. For this method to give good results, the background heat leak should remain fairly constant in the time scale of interest, i.e. the "before" and "after" recorder traces should remain parallel. Below 4.2°K, this could be readily achieved by keeping the bath slightly hotter than the sample. Initially, we controlled the bath heating rate by progressively closing the small valve. When the latter was completely closed, we switched on the bath heater and increased the current as required.

Figure 7. Example of recorder pen path

a.) Specific heat data

b.) Field rotation data

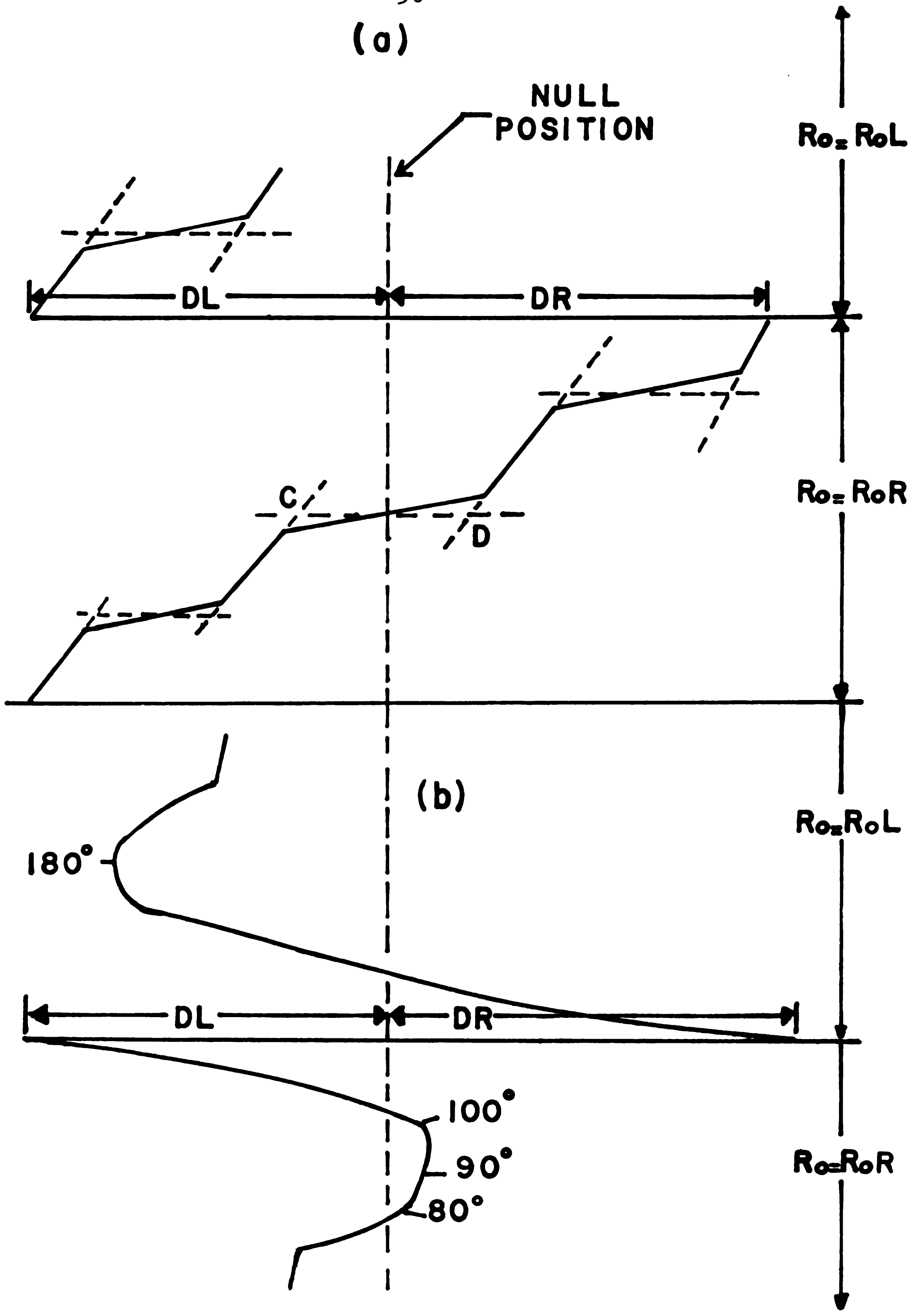
(a)
NULL POSITION
Ro= RoL
DL
DR
Ro= RoR
C
D
(b)
Ro=RoL
180°
DL
DR
100°
90°
80°
Ro=RoR

Figure 7

For best results, we usually chose the sample heater current to produce a deviation of between 10-15 divisions across the chart during the heating period (which usually lasts for 20 seconds). Near the critical temperature, this was usually not done to better visualize the transition.

4. Adiabatic field rotations

In magnetic phase diagram measurements, the first task after temperature calibration consisted in finding the direction of the easy axis. With the field maintained constant, the magnet was rotated until the sample showed a minimum in temperature. According to a simple mean field theory,[53] this corresponded to the direction of magnetization in the antiferromagnetic state.

5. Adiabatic magnetizations

To determine the first order antiferromagnetic - spin flop (AF-SF) boundary, the field, aligned along the easy axis, was swept up at a suitable rate. If initially the sample was in the antiferromagnetic state, it should start cooling until it reached the boundary, where the temperature should either stay constant or increase. The value of the field at the critical point was taken as the critical field. To ascertain that an AF-SF transition did take place, the field was swept down. The sample should start cooling until it reached the SF-AF boundary, when it should start warming again. To trace out the complete boundary, the sample was heated to near the desired new temperature, and the new critical field determined as before.

6. Antiferromagnetic-Paramagnetic boundary

This boundary was determined by specific heat measurements in a magnetic field. The boundary "crossing" was fairly easily seen by a sudden increase in temperature change with a given heat input. The field was then set to a new value, and the diffusion pump disconnected from the inner and outer cans. Some Helium gas was admitted into the inner can. The sample would cool back to the temperature of the Helium bath. Once the sample had cooled back to the ordered state, the inner can was pumped on again, and a new set of specific heat data taken.

7. Shutdown

At the end of an experiment, we closed the inner and outer cans. The remaining liquid Helium was pumped out of the dewar and the Helium can. The diffusion pump was turned off, but the forepump left on until the next morning, when it was turned off and the Stokes pump disconnected from the dewar. Next, the Helium dewar was flushed with nitrogen gas, and air was admitted into the inner can, the outer can and the forepump. The sample would be removed from the calorimeter, not too long afterwards.

C. Data Reduction

1. Converting pressure into temperature

We converted pressures into temperatures in the standard way. Above the Lambda point, the U-tube manometer reading was first changed to pressure at 0°C. Next, the height of liquid helium above the sample was estimated and a hydrostatic pressure correction added to the previous value (the exact helium height is not very critical). This hydrostatic correction was not made below the Lambda point, since then no temperature gradient existed in liquid helium. Also, no 0°C correction was made to readings below 2.5cm Hg, because those were read off the McLeod gauge which is relatively insensitive to temperature change.

Finally, the corrected pressures were converted to temperatures, using a computer generated interpolation table based on the 1958 He^4 scale of temperature.[20]

2. Thermometer calibration equation

First, we fitted the resistance-temperature relation to the two-parameters Clement-Quinnell equation.[21]

$$\left(\frac{\ln R}{T}\right)^{\frac{1}{2}} = a + b \ln R \qquad (2.2)$$

The relative deviations were next fitted to a fourth degree polynomial in lnR.

$$\frac{\left[\frac{\ln R}{T}\right]^{\frac{1}{2}}_{\text{meas}} - \left[\frac{\ln R}{T}\right]^{\frac{1}{2}}_{\text{calc}}}{\left[\frac{\ln R}{T}\right]^{\frac{1}{2}}_{\text{meas}}} = \sum_{n=0}^{4} C_n (\ln R)^n \qquad (2.3)$$

This resulted in the following explicit expression for T.

$$T = \ln R \left[\frac{a + b \ln R}{1 - \sum_{n=0}^{4} C_n (\ln R)^n} \right]^{-2} \qquad (2.4)$$

This type of fit usually resulted in relative deviations of no more than 0.2%.

Occassionally the following equation was also used.

$$\frac{1}{T} = \sum_{n=1}^{6} C_n (\ln R)^{n-1} \qquad (2.5)$$

Whichever equation the better fit.

3. Determination of thermometer resistances

When the chart recorder pen was at the null position, the thermometer resistance R_T simply equalled the potentiometer setting R_o. However, most experimental data were taken with the potentiometer offset from the null position. We used the following empirical equation.

$$R_T = \frac{R_o - [C_1 - C_2 R_T - 2C_3 R_T^2 - 3C_4 R_T^3]\, D}{1 + [C_2 + 2C_3 R_T + 3C_4 R_T^2]\, D} \qquad (2.6)$$

Where

D = deviation from the null position, considered positive (negative) when the pen was at the right (left) of the null position.

An iteration process was employed to determine R_T. First, R_o was substituted into (2.6) to get a new value for R_T, which was in turn substituted into (2.6), etc... . This process was considered convergent, when two successive values of R_T differed by 0.1%.

The coefficients C_1 to C_4 were obtained from a least squares fit to the chart calibration equation

$$\frac{R_oL - R_oR}{DL - DR} = C_1 + C_2R + C_3R^2 + C_4R^3 \qquad (2.7)$$

Chart calibration points were taken when the pen was near the extreme right of the chart (with deviation DR from the null position) for a given potentiometer setting R_oR. The latter was then changed to a new setting R_oL, such that the pen moved to near the extreme left of the chart, with deviation DL from the null position. In (2.7), R was approximated by $\frac{R_oL + R_oR}{2}$.

The relative deviations of this fit usually did not exceed 2%.

4. Calculations for specific heat, field rotations and field sweep data

The heat capacity HC was computed as

$$HC = \frac{VIt}{\Delta T} \qquad (2.8)$$

where V = voltage across heater

I = current through heater

t = duration of heat pulse

ΔT = temperature difference

Knowledge of the sample mass and its molecular weight would then allow conversion into specific heat values. The chart positions corresponding to the "true" initial and final temperatures were determined graphically, as described earlier. They were converted to resistance and temperature values. The difference between those temperatures was taken as ΔT, while their average was considered as the temperature corresponding to the computed specific heat.

The largest source of error came from reading distances on the chart. As mentioned earlier, this error was minimized by choosing suitable heat pulses so as to get sufficiently large deviations. Another source of error was the heat capacities of the addenda,thermometer, leads, varnish. According to N. D. Love[18], this error was largest at 4°K and amounted to nearly 2.8% of the total heat capacity at that temperature.

For field rotations and field sweep experiments, the recorder trace was marked whenever a certain angle or field was reached. The chart positions corresponding to those marks were converted to temperatures, as for specific heat data.

III. Experimental Results and Discussion

A. Review of calorimetric and magnetic properties of $CoCl_2 \cdot 6H_2O$ and $NiCl_2 \cdot 6H_2O$

Before discussing the results we have obtained, it will be pertinent to review the magnetic properties of $CoCl_2 \cdot 6H_2O$ and $NiCl_2 \cdot 6H_2O$.

1. Crystallographic and magnetic structures

Both $NiCl_2 \cdot 6H_2O$ and $CoCl_2 \cdot 6H_2O$ belong to the monoclinic base centered type, with space group C 2/m. Their crystal structures have been determined by Mizuno[22,23], and the appropriate lattice parameters are summarized in Table I.

Table I

Lattice parameters of $CoCl_2 \cdot 6H_2O$ and $NiCl_2 \cdot 6H_2O$

	a (Å)	b (Å)	c (Å)	β	no. of spins per unit cell
$CoCl_2 \cdot 6H_2O$	10.34	7.06	6.67	122°20'	2
$NiCl_2 \cdot 6H_2O$	10.23	7.05	6.57	122°10'	2

Despite their similarities in crystallographic structure and lattice parameters, the magnetic structures of the salts turn out to be different. Fig. 8 depicts the magnetic structure of $CoCl_2{\cdot}6H_2O$ in the antiferromagnetic state, as determined by Kleinberg[24] using neutron diffraction. The easy magnetization direction lies along the c-axis. The nearest neighbor exchange interaction J occurs along the diagonal in the a-b plane. Appreciable exchange interactions J_1, J_2 may also exist along the b and c axes.

As also determined by Kleinberg[25], the spins in $NiCl_2{\cdot}6H_2O$ are arranged similarly, except that the easy axis has moved in the a-c plane to a direction roughly 10° away from the a-axis.

Part of the reason for the difference in the magnetic behavior of $NiCl_2{\cdot}6H_2O$ and $CoCl_2{\cdot}6H_2O$ lies in the fact that the Ni^{++} and Co^{++} have different ground states, and therefore respond differently to the crystal field. Each Ni^{++} or Co^{++} ion is surrounded by an elongated octahedron consisting of four water molecules and two chlorine ions. The four water molecules form a distorted square, inclined by about 9° from the b-c plane while the chlorine ions lie along an axis perpendicular to the square. The resulting cubic and tetragonal fields split the ground state $^4F_{9/2}$ of the free Co^{++} ion into two triplets and a singlet, with a triplet lying lowest.[26] Since $S = 3/2$, this triplet has a fourfold spin degeneracy. The other two water molecules introduce a small orthorhombic component which, along with the spin-orbit

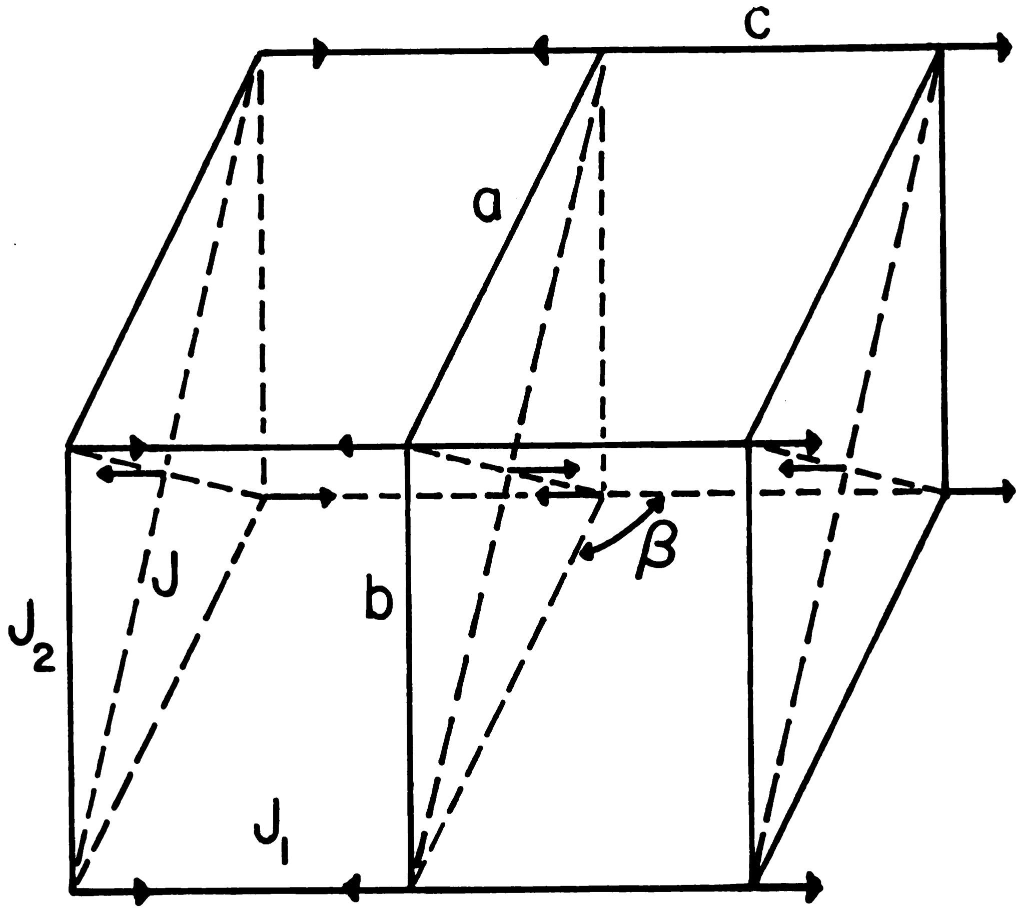

Figure 8. Magnetic structure of $CoCl_2 \cdot 6H_2O$
J, J_1, J_2 are possible exchange interactions.

coupling, split the lowest triplet into six Kramers doublets. It turns out that the lowest doublet lies about 10°K below the next lowest doublet, compared to a Neel temperature of only 2.29°K. Therefore, at low temperatures, one may describe the magnetic properties of $CoCl_2 \cdot 6H_2O$ by a spin Hamiltonian with effective spin $S = 1/2$. One may also expect the exchange interactions and the g tensor to be anisotropic.[27]

On the other hand, a cubic field lifts the orbital degeneracy of the Ni^{++} ion in its $^3F_4$ ground state, leaving an orbital singlet lowest.[28] The orthorhombic component lifts the remaining spin degeneracy, so that the effective spin $S = 1$, the same as the true spin of the free Ni^{++} ion. Susceptibility data and low temperature specific heat have been successfully analysed by Hamburger and Friedberg[29], and Iwashita and Uryu[30], using the following Hamiltonian.

$$\mathcal{H} = -J \sum_{<i,j>} \vec{S}_i \cdot \vec{S}_j - J_1 \sum_{<i,k>} \vec{S}_i \cdot \vec{S}_k + D\left[\sum_i S_{iz}^2 + \sum_j S_{jz}^2\right] + E\left[\sum_i (S_{ix}^2 - S_{iy}^2) + \sum_j (S_{jx}^2 - S_{jy}^2)\right] \tag{3.1}$$

In (3.1), J and J_1 denote nearest and next-nearest neighbors exchange interactions. It is also assumed that the nearest neighbor spins $\vec{S}_i$, $\vec{S}_j$ belong to different sublattices.

According to ref. 30

$J = -(2.78 \pm 0.02)°K$ $J_1 = -(0.30 \pm 0.10)°K$

$D = -(1.00 \pm 0.02)°K$ $E = (0.05 \pm 0.02)°K$

Thus, susceptibility data suggest that $NiCl_2 \cdot 6H_2O$ is a predominantly planar Heisenberg antiferromagnet, with a relatively strong uniaxial single ion anisotropy.

As for $CoCl_2 \cdot 6H_2O$, analysis of the paramagnetic susceptibility data led Kimura[31] to suggest that the exchange interactions are anisotropic. Further, the ratio J_1/J between next nearest and nearest neighbor interactions nearly equals 3/4. This simplies that the magnetic behavior of $CoCl_2 \cdot 6H_2O$ cannot be two-dimensional. More recently, Cieplak[32] added additional single ion anisotropy terms to the Kimura Hamiltonian, to account for the low temperature dependence of the paramagnetic-spin flop boundary.

Thus far, theoretical analyses of the susceptibility data seem to imply that $CoCl_2 \cdot 6H_2O$ and $NiCl_2 \cdot 6H_2O$ have different magnetic dimensionalities. To gain additional insight into the matter, let us next turn to specific heat data.

2. Specific Heat Data

The specific heats of $CoCl_2 \cdot 6H_2O$ and $NiCl_2 \cdot 6H_2O$ were first measured by Robinson and Friedberg[32], in the temperature interval 1.4°K to 20°K. They determined $T_N = 2.29°K$ and 5.34°K for $CoCl_2 \cdot 6H_2O$ and $NiCl_2 \cdot 6H_2O$ respectively. The total magnetic entropy changes correspond to the expected effective spins. Further, the amount of entropy gained up to T_N is only about 50% of the total entropy. This suggests two dimensional magnetic behavior.[33]

In Fig. 9, we have plotted the Robinson-Friedberg data (corrected for lattice specific heat) vs. T/T_N. Fig. 9 also shows the theoretical specific heats given by the Onsager solution, and by the planar $S = 1/2$ and $S = 1$ BPW models. Note that the $CoCl_2 \cdot 6H_2O$ data follows the exact quadratic Ising curve rather well, from 0.8 T/T_N up to 0.98 T/T_N. Above T_N, the fit between the $CoCl_2 \cdot 6H_2O$ data and the Onsager curve seems rather poor, while the $NiCl_2 \cdot 6H_2O$ data appear to fit the latter somewhat better up to 1.2 T/T_N. Below T_N, the $NiCl_2 \cdot 6H_2O$ data deviate systematically from the quadratic Ising curve, as befits an antiferromagnet with $S = 1$. What seems rather surprising is the good agreement between the $NiCl_2 \cdot 6H_2O$ data and the planar, $S = 1/2$ BPW model. In the absence of physical arguments to the contrary, this apparent fit should be merely considered as a mathematical accident. A priori, one might expect a $S = 1$ Ising model to do better. We have computed the specific heat of a planar, $S = 1$ Ising model in the generalized BPW approximation of Obokata and Oguchi.[34] As one can see, this approximation does not fit the data at all. Above T_N, both BPW approximations fail badly, because they underestimate the exact short range order.

Thus, one can say that the $S = 1/2$, planar BPW and the quadratic Ising models fit the $NiCl_2 \cdot 6H_2O$ and $CoCl_2 \cdot 6H_2O$ specific heats respectively, in some temperature range below

Figure 9. Experimental specific heats of $NiCl_2 \cdot 6H_2O$ and $CoCl_2 \cdot 6H_2O$ compared with the BPW and Ising models

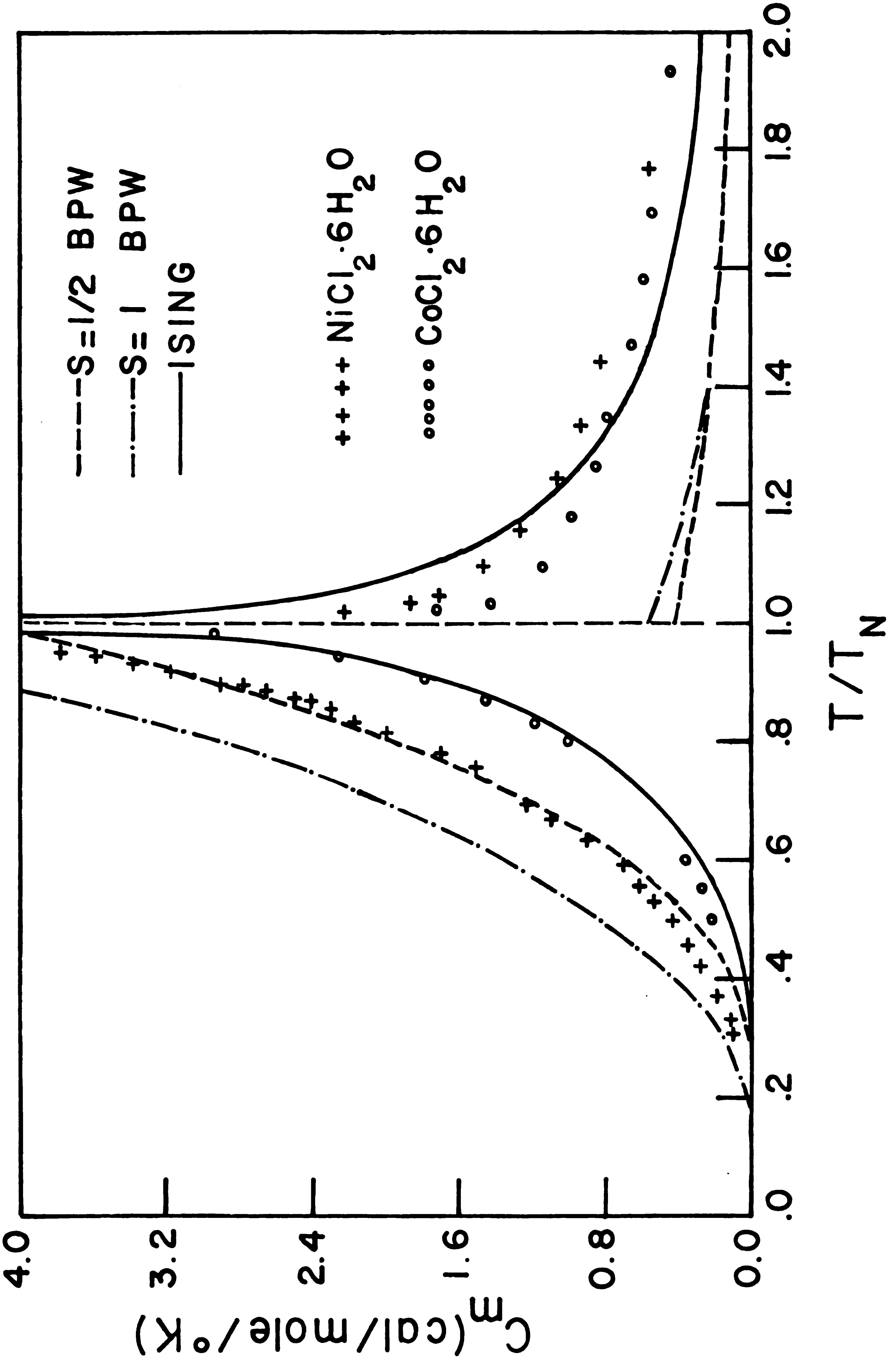
S=1/2 BPW
S= 1 BPW
ISING
$NiCl_2 \cdot 6H_2O$
$CoCl_2 \cdot 6H_2O$
C_m(cal/mole/°K)
4.0
3.2
2.4
1.6
0.8
0.0
.0
.2
.4
.6
.8
1.0
1.2
1.4
1.6
1.8
2.0
T/T_N

Figure 9

T_N (at least between 0.7 T/T_N and 0.9 T/T_N). Above T_N the quadratic Ising model fits the data better. A priori, one should not expect effective field type theories, such as the BPW models, to account for the critical behaviors of real systems. In view of our experimental results, it is pertinent to ask the question: to what extent does the quadratic Ising model fit the $CoCl_2 \cdot 6H_2O$ and $NiCl_2 \cdot 6H_2O$ specific heats near T_N?

High resolution calorimetric studies of $CoCl_2 \cdot 6H_2O$ were first carried out by Skalyo and Friedberg.[35] They found that in the reduced temperature range $5 \times 10^{-3} < t < 5 \times 10^{-2}$

$$\frac{C}{R} = -0.239 - 0.271 \ln t + \Delta \tag{3.2}$$

with $\Delta = 0$ if $T > T_N$, and $\Delta = 0.574$ if $T < T_N$.

Here $t = \dfrac{T - T_N}{T_N}$ with $T_N = 2.2890°K$

On the other hand, the critical behavior of the $NiCl_2 \cdot 6H_2O$ specific heat has been determined by Johnson and Reese as[36]

$$\frac{C}{R} = -0.55 \ln t + 0.27 \qquad T < T_N \tag{3.3}$$

$$\frac{C}{R} = 0.61 t^{-0.17} - 0.14 \qquad T > T_N \tag{3.4}$$

with $T_N = 5.348°K$

As noted by Wielinga et al,[37] for $t < 0.1$ the quadratic Ising model specific heat agrees to within a few percent with

$$\frac{C}{R} = -0.49 \ln t - 0.29 \tag{3.5}$$

for both $T < T_N$ and $T > T_N$.

A comparison of (3.5) with (3.2), (3.3), (3.4) shows that the quadratic Ising model does not describe the critical behaviors of $NiCl_2 \cdot 6H_2O$ and $CoCl_2 \cdot 6H_2O$ quantitatively, although the logarithmic nature of the transition may be given correctly. The critical behavior of $CoCl_2 \cdot 6H_2O$ has some similarities with those of Rb_2CoF_4 and K_2CoF_4, in which the Co^{++} ions are also subjected to crystal fields with octahedral cubic symmetry. For those compounds however, magnetization data show a much more striking agreement with the quadratic Ising models.[38] $NiCl_2 \cdot 6H_2O$ is more similar to K_2NiF_4, a two dimensional Heisenberg antiferromagnet whose critical behavior is dominated by a single ion anisotropy term. According to the recent measurements of Birgeneau et al.,[39] the magnetization curve of K_2NiF_4 does not follow the prediction of the quadratic Ising model quantitatively near T_N. But the critical exponent $\beta = 0.14$ still comes out close to the theoretical $\beta = 0.125$.

As far as the magnetic dimensionality of $CoCl_2 \cdot 6H_2O$ is concerned, one should also mention an attempt to fit the specific heat of this compound to the so called XY model.

The Hamiltonian for this model is

$$\mathcal{H}_{XY} = - \sum_{<i,j>} [J_x S_{xi} S_{xj} + J_y S_{yi} S_{yj}] \tag{3.6}$$

Assuming $J_x = J_y$ and the Co spins confined in the bc plane (so that x,y refer to the c and b directions respectively), DeJongh et al.[40] found good agreement between the $CoCl_2 \cdot 6H_2O$ specific heat and the quadratic XY model, in the temperature range 4°K to 10°K. Since the quadratic XY model does not allow long range order, the Ising-like anomaly in $CoCl_2 \cdot 6H_2O$ is presumably due to an in-plane anisotropy (J_x can differ from J_y by about 4%).

The low temperature specific heats of $CoCl_2 \cdot 6H_2O$ and $NiCl_2 \cdot 6H_2O$ also present some interesting features. The calorimetric measurements of Donaldson and Edmonds[41] indicated that the specific heat of $CoCl_2 \cdot 6H_2O$ follows a T^3 law between 0.7°K and 1.6°K (corresponding to 0.3 T/T_N and 0.7 T/T_N). The $NiCl_2 \cdot 6H_2O$ specific heat does likewise between 2.0°K and 4.0°K (or from 0.4 T/T_N to 0.75 T/T_N). Below 2.0°K the data decrease more rapidly with temperature. This behavior can be reasonably well explained by the Eisele-Keffer[42] spin wave theory of the two sublattice antiferromagnet with uniaxial anisotropy. According to this theory, for $T \ll T_N$, the magnetic specific heat C_m is given by

$$C_m = AT^3 f(T/T_{AE}) \tag{3.7}$$

where

A = constant which depends on the lattice structure

f(x) = function which approaches 1 for $x \gg 1$ and drops exponentially for $x < 1$

kT_{AE} = a measure of the energy gap introduced by anisotropy in the spin wave spectrum.

Donaldson and Edmonds found that the choice $T_{AE} = 4.0°K$ leads to a reasonable agreement between (3.7) and the $NiCl_2 \cdot 6H_2O$ data. Later, Hamburger and Friedberg[29] found that the same choice of T_{AE} produced good agreement between the low temperature theoretical and experimental parallel susceptibilities. The situation is less clear for $CoCl_2 \cdot 6H_2O$. The specific heat shows no sign of decreasing down to 0.7°K. To account for this, one should take $T_{AE} < 0.6°K$. However, the antiferromagnetic resonance data of Date[43] gave $T_{AE} = 1.66°K$. There has not yet been any satisfactory resolution of the discrepancy between these two estimations of T_{AE}. Kimura[43] attempted to explain the spin wave behavior of $CoCl_2 \cdot 6H_2O$ from a three dimensional anisotropic exchange Hamiltonian. It may be significant to note that his theory failed to account for the specific heat T^3 dependence.

To sum up, one can say that anisotropy plays an important role in the magnetic behaviors of $NiCl_2 \cdot 6H_2O$ and $CoCl_2 \cdot 6H_2O$. The calorimetric and susceptibility data for $NiCl_2 \cdot 6H_2O$ can be at least qualitatively understood in terms of a planar Heisenberg Hamiltonian, with single ion anisotropy. The exact nature of the anisotropy in $CoCl_2 \cdot 6H_2O$ is still a matter of some controversy. On the one hand, it is possible to fit the magnetic susceptibility data from 1.2°K to 4.2°K using the Kimura three-dimensional anisotropic Hamiltonian.[43] On the other hand, zero field calorimetric data suggest a two dimensional magnetic behavior, with nearest neighbor interactions only. One should also add that a consideration of the possible superexchange paths between the Co^{++} ions also tends to favor two dimensional behavior.[44] At any rate, the quadratic Ising model can account for the critical behaviors of $NiCl_2 \cdot 6H_2O$ and $CoCl_2 \cdot 6H_2O$ much better than the BPW models.

B. The Concentration Phase Diagram

We have measured the specific heats of ten mixed crystals, grown from saturated aqueous solutions containing various stoichiometric ratios of $NiCl_2 \cdot 6H_2O$ and $CoCl_2 \cdot 6H_2O$. Before each run, small pieces were cut from the sample and later sent out for chemical analysis. All the samples studied showed fairly sharp transitions, and the temperatures corresponding to specific heat maxima were taken as the Néel temperatures. The chemical analysis results indicate that all samples have chemical compositions which can be well represented by the formula $Co_xNi_{1-x}Cl_2 \cdot 6H_2O$. Table II lists the various chemical compositions, along with the corresponding Néel temperatures.

To explain the variation of T_N with chemical composition, we proceed as follows:

Table II

Chemical compositions[a] and Néel temperatures of the samples for which calorimetric measurements have been made. The values quoted for each element are percentages by weight.

Chemical Formula	Co	Ni	Cl	H_2O	T_N(°K)
$CoCl_2\cdot 6H_2O$[b]	24.77	0.00	29.80	45.43	2.29[c]
$Co_{0.89}Ni_{0.11}\ Cl_2\cdot 6H_2O$	21.47	2.56	29.97	44.43	2.43
$Co_{0.84}Ni_{0.16}\ Cl_2\cdot 6H_2O$	20.85	3.96	30.15	45.32	2.47
$Co_{0.83}Ni_{0.17}\ Cl_2\cdot 6H_2O$	20.31	4.24	29.92	45.30	2.49
$Co_{0.57}Ni_{0.43}\ Cl_2\cdot 6H_2O$	9.26	7.11	29.54	44.68	2.77
$Co_{0.52}Ni_{0.48}\ Cl_2\cdot 6H_2O$	13.31	12.18	29.99	44.76	2.87
$Co_{0.50}Ni_{0.50}\ Cl_2\cdot 6H_2O$	12.33	12.15	30.00	44.40	2.96
$Co_{0.30}Ni_{0.70}\ Cl_2\cdot 6H_2O$	7.49	17.86	29.69	44.96	3.47
$Co_{0.24}Ni_{0.76}\ Cl_2\cdot 6H_2O$	5.97	19.08	30.78	44.78	3.77
$Co_{0.16}Ni_{0.89}\ Cl_2\cdot 6H_2O$	4.18	21.41	29.99	44.34	4.26
$Co_{0.13}Ni_{0.87}\ Cl_2\cdot 6H_2O$	3.25	21.92	29.51	45.25	4.47
$NiCl_2\cdot 6H_2O$[b]	0.00	24.70	29.83	45.47	5.34[c]

---

[a] All chemical analyses carried out by Schwarzkopf Microanalytical Laboratory, Woodside, N. Y.

[b] Values for $CoCl_2\cdot 6H_2O$ and $NiCl_2\cdot 6H_2O$ are calculated values.

[c] Determined by W. K. Robinson and S. A. Friedberg, Phys. Rev., 117, 402 (1960).

a.) All theoretical curves are required to give the experimental Néel temperatures of pure $NiCl_2 \cdot 6H_2O$ and $CoCl_2 \cdot 6H_2O$. This condition fixes J_{Ni-Ni} and J_{Co-Co} in the particular theoretical model under consideration.

b.) To determine J_{Ni-Co}, we also require all theoretical curves to pass through a third fixed point (T_N = 2.96°K, x = 0.5). The choice of this fixed point may appear somewhat arbitrary, and will be justified later on.

1. Mean Field Fits

Fig. 10 shows the concentration phase diagram of the mean field models, as given by the above fitting procedure and equations (1.29), (1.45) of chapter I. As one can see, the virtual crystal approximation fails rather badly. The quenched model improves the situation significantly, especially at high Ni concentrations. However, both concentration phase diagrams start out by dropping below 2.29°K, and continues to predict Néel temperatures below 2.29°K, even up to 20% Ni. This is certainly not the case experimentally. In retrospect, one should not expect the virtual crystal approximation to work well for mixtures of magnetic ions which interact mainly through nearest neighbors, since this approximation is valid only when the fluctuations in local concentrations are unimportant.[45] This happens when the interactions are of long range, as in rare earth alloys for example.

Figure 10. T_N vs. concentration diagram for mean field models

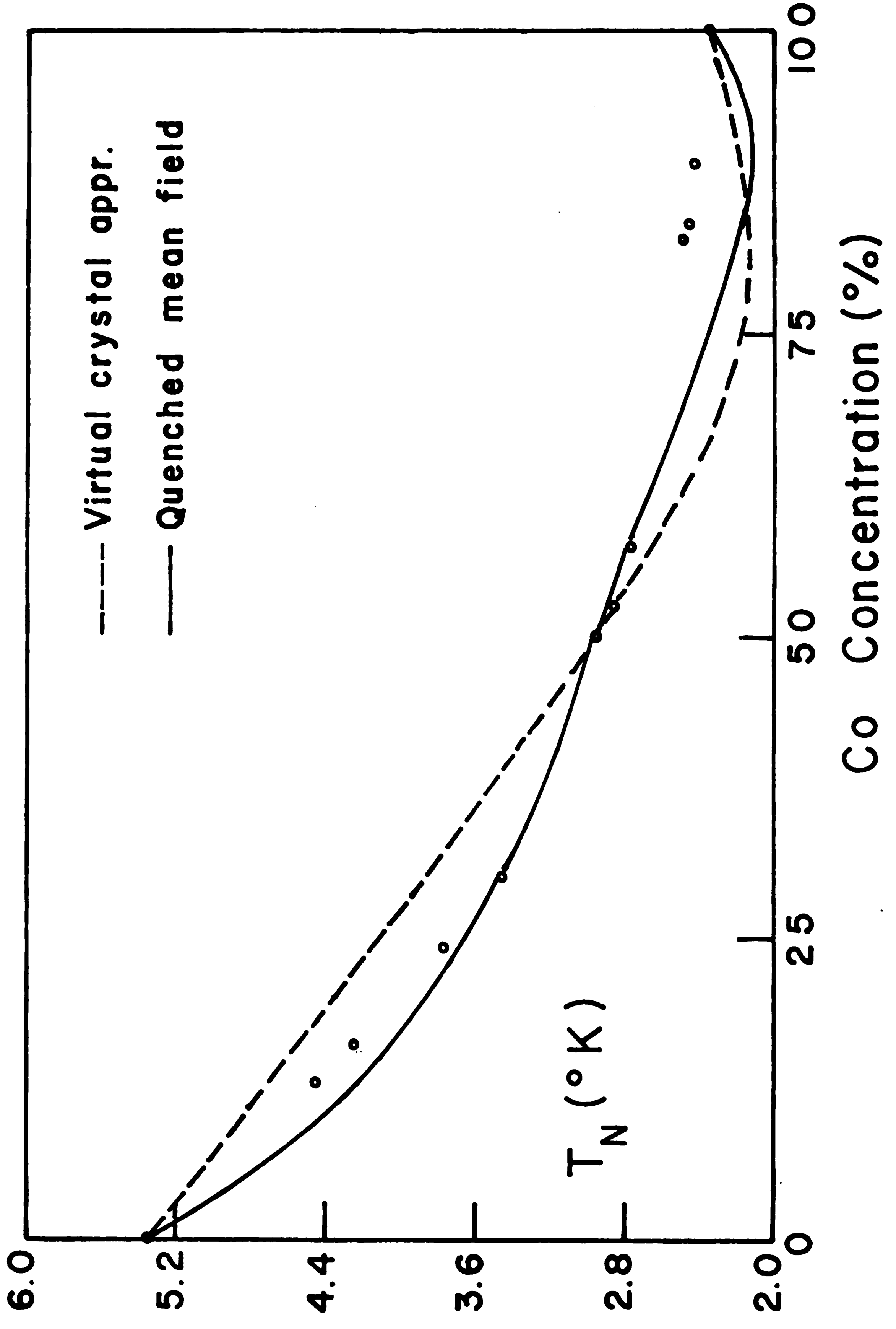

6.0
5.2
4.4
3.6
2.8
2.0
0
25
50
75
100
T_N (°K)
Co Concentration (%)
Virtual crystal appr.
Quenched mean field

Figure 10

The quenched mean field model takes a more realistic configurational average, and fits the data better. The failure at high concentrations of Co is probably due to the low effective spins and the two dimensional magnetic behavior of the Co ions. Usually, a combination of low spin and low dimensionality is fatal to mean field theories. We have not tried this, but one way to improve the mean field models may consist in explicitly including single ion anisotropy or anisotropic exchange terms in the Hamiltonian.

2. The Annealed Ising and Bethe Lattices

To determine the concentration phase diagram of the annealed Ising model, we use equation (1.68) in conjunction with the bond distribution function (1.77). This yields the following equation

$$\frac{p^2}{\coth(K_c-\beta_c J_{AA})-\varepsilon_c} + \frac{2pq}{\coth(K_c-\beta_c J_{AB})-\varepsilon_c} + \frac{q^2}{\coth(K_c-\beta_c J_{BB})-\varepsilon_c} = 0 \tag{3.8}$$

The concentration phase diagram of the annealed BPW model is more simply given by

$$p^2\tanh(\beta_c J_{AA}) + 2pq\tanh(\beta_c J_{AB}) + q^2\tanh(\beta_c J_{BB}) = \frac{1}{z-1} \tag{3.9}$$

In (3.8) and (3.9), p and q denote the Co and Ni fractions respectively ($p+q = 1$), while A and B refer to Co and Ni. z is the number of nearest neighbors. For the 2-dimensional case, $K_c = \frac{1}{2}\ln(1 + \sqrt{2})$; $\varepsilon_c = \frac{1}{\sqrt{2}}$ and $z = 4$.

For each value of p, the critical temperature T_c is determined by solving (3.8) or (3.9) numerically, using the Newton-Raphson algorithm. The latter is considered convergent when the relative difference between two successive approximations becomes less than 10^{-6}. All computer programs used in concentration phase diagram and specific heat calculations are listed in the appendix.

Fig. 11 shows the concentration phase diagrams of the planar annealed Ising and BPW models. The agreement between both models and experimental data appears reasonable. Overall, the Ising model tends to do better than the BPW model.

In Fig. 11, we have also plotted the previous results obtained by Robinson and Simmons,[46] and Takeda et al.[47] Robinson and Simmons determined T_N by the disappearance of the Cl^{35} NQR signal in four $Ni_xCo_{1-x}Cl_2 \cdot 6H_2O$ crystals with x = 0, 0.1, 0.25, 0.5. (Incidentally, they also stated that "X ray powder patterns show these crystals to be isomorphic"). Takeda et al. performed calorimetric and susceptibility measurements on powder samples. Robinson's data agree with ours, except for the last T_N at 50% Co. On the other hand, Takeda's results are systematically higher than ours. The origin of this discrepancy is not presently understood. We tend to think that the uncertainties in concentrations are higher than claimed in Takeda's paper.

With regards to the possibility of 3-dimensional magnetic behavior in $CoCl_2 \cdot 6H_2O$, we have also considered the annealed simple cubic Ising model. From high temperature series expansions, Sykes et al.[48] estimate $K_c = 0.2217$ and

Figure 11. T_N vs. concentration diagram for the annealed Ising and BPW models

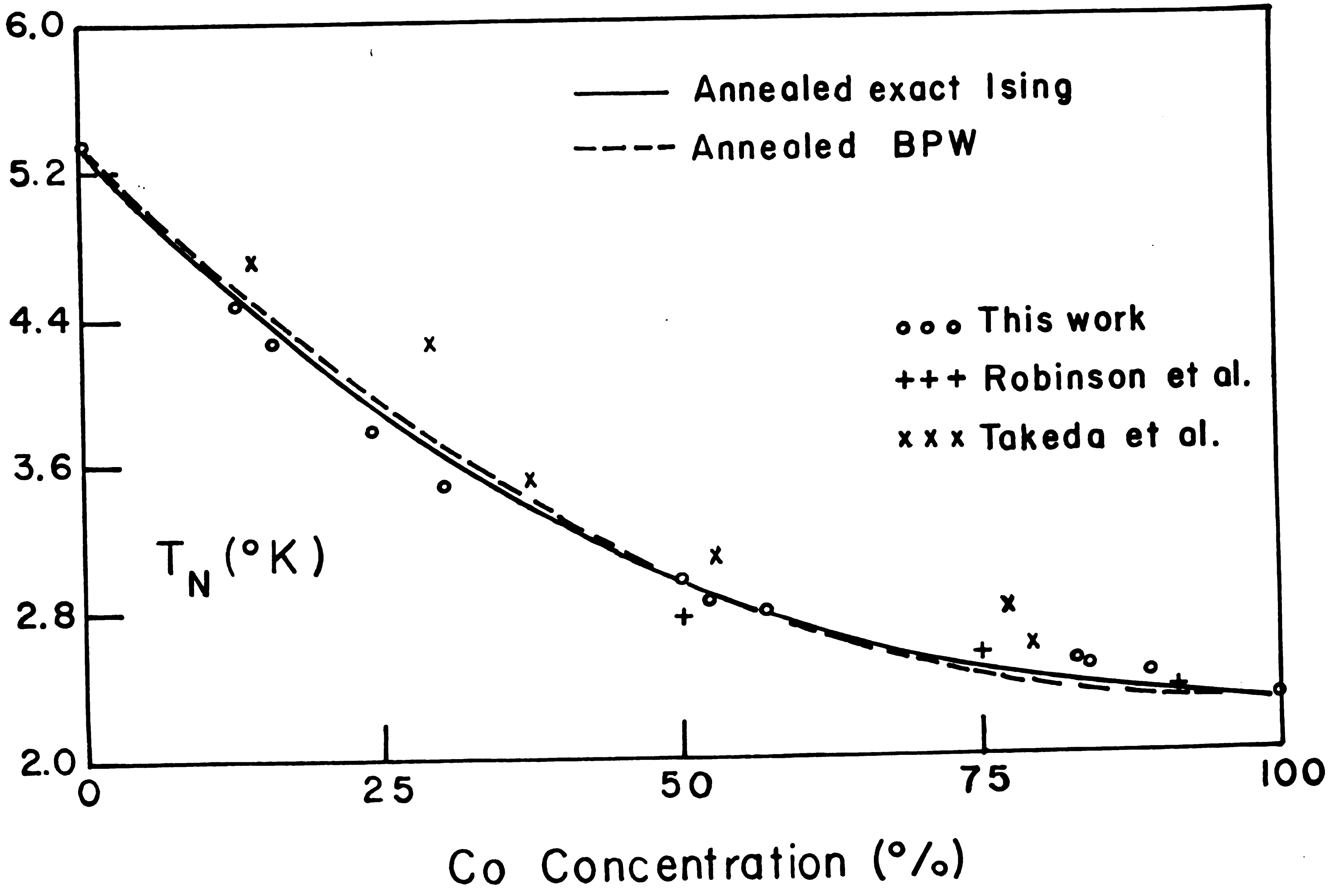
6.0
5.2
4.4
3.6
2.8
2.0
T_N (°K)
0
25
50
75
100
Co Concentration (°/o)
—— Annealed exact Ising
– – – – Annealed BPW
∘∘∘ This work
+++ Robinson et al.
x x x Takeda et al.

Figure 11

$\varepsilon_c = 0.3307$ for the simple cubic Ising model. Inserting these values into (3.8), we obtain the concentration phase diagram of the annealed simple cubic Ising model. Fig. 12 shows both square lattice and simple cubic phase diagrams. The latter gives lower critical temperatures for high concentrations of Co (there is even a shallow minimum near 100% Co), and higher critical temperatures for high Ni concentrations. On the scale of the graph, the differences between the two are slight but sufficiently significant to allow one to claim that the annealed square lattice Ising model fits the data better, at least for high Co concentrations.

3. Annealed and Quenched Bethe Lattices

The concentration phase diagram for the quenched BPW model is given by equation (1.113). Figure 13 shows the concentration phase diagrams of the quenched and annealed BPW models. The same J_{Ni-Co} has been chosen for both phase diagrams, to allow a direct comparison between the two up to 80% Co, both models give practically the same T_N. But as the Ni concentration increases, the quenched model give systematically higher critical temperatures. Fig. 13 also shows the phase diagram of the quenched classical Heisenberg BPW model, given by equation (1.114). Note that near 100% Co, the latter phase diagram starts out by dropping below 2.29°K. However, this initial minimum is much shallower than in the case of the virtual crystal mean field model (refer to fig. 10). For high Ni concentrations, both classical BPW and virtual

Figure 12. T_N vs. concentration diagram for the annealed square lattice and simple cubic Ising models

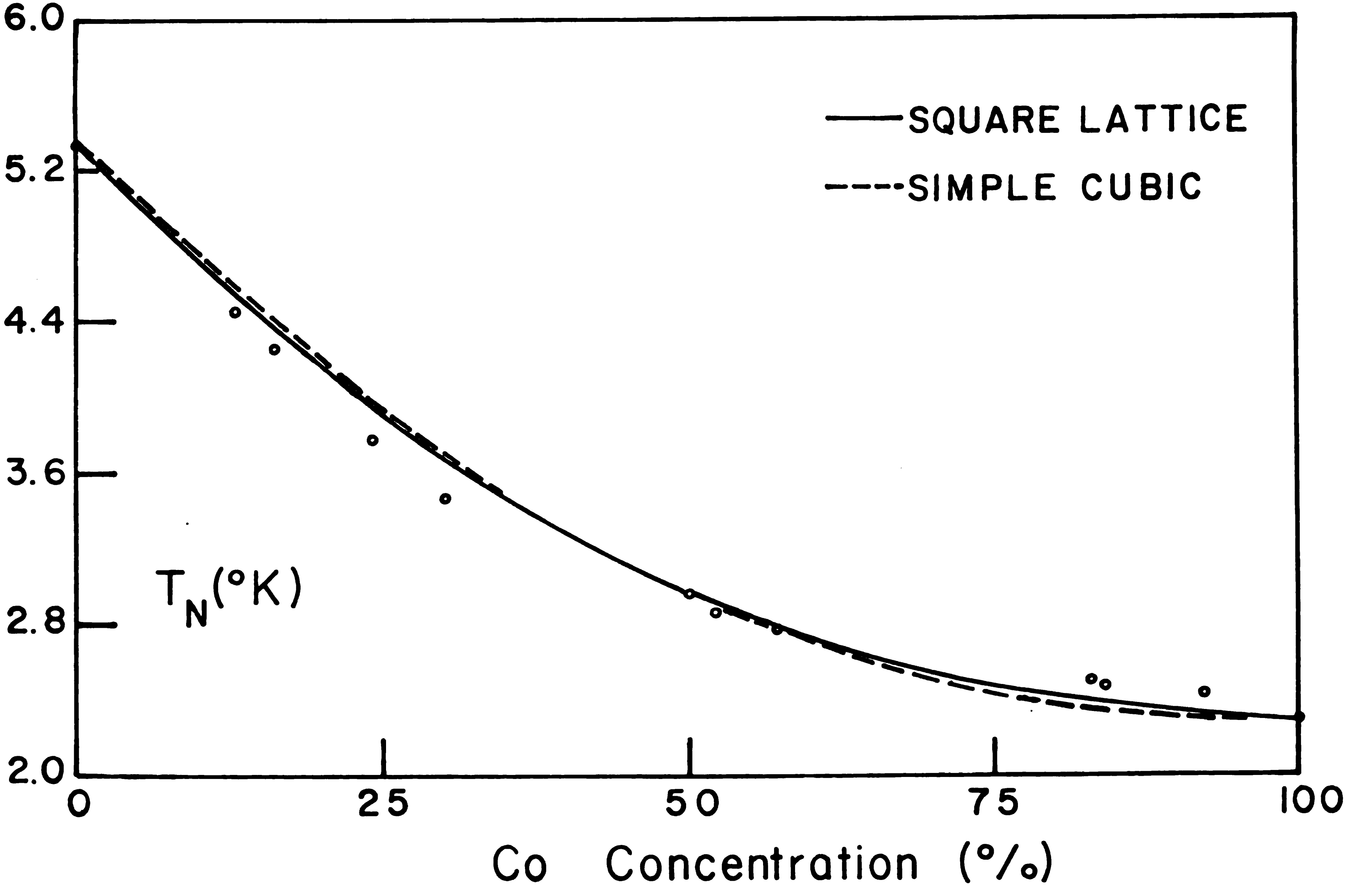
6.0
5.2
4.4
3.6
2.8
2.0
0
25
50
75
100
T_N(°K)
Co Concentration (°/o)
——SQUARE LATTICE
----SIMPLE CUBIC

Figure 12

Figure 13. T_N vs. concentration diagram for the annealed and quenched BPW models

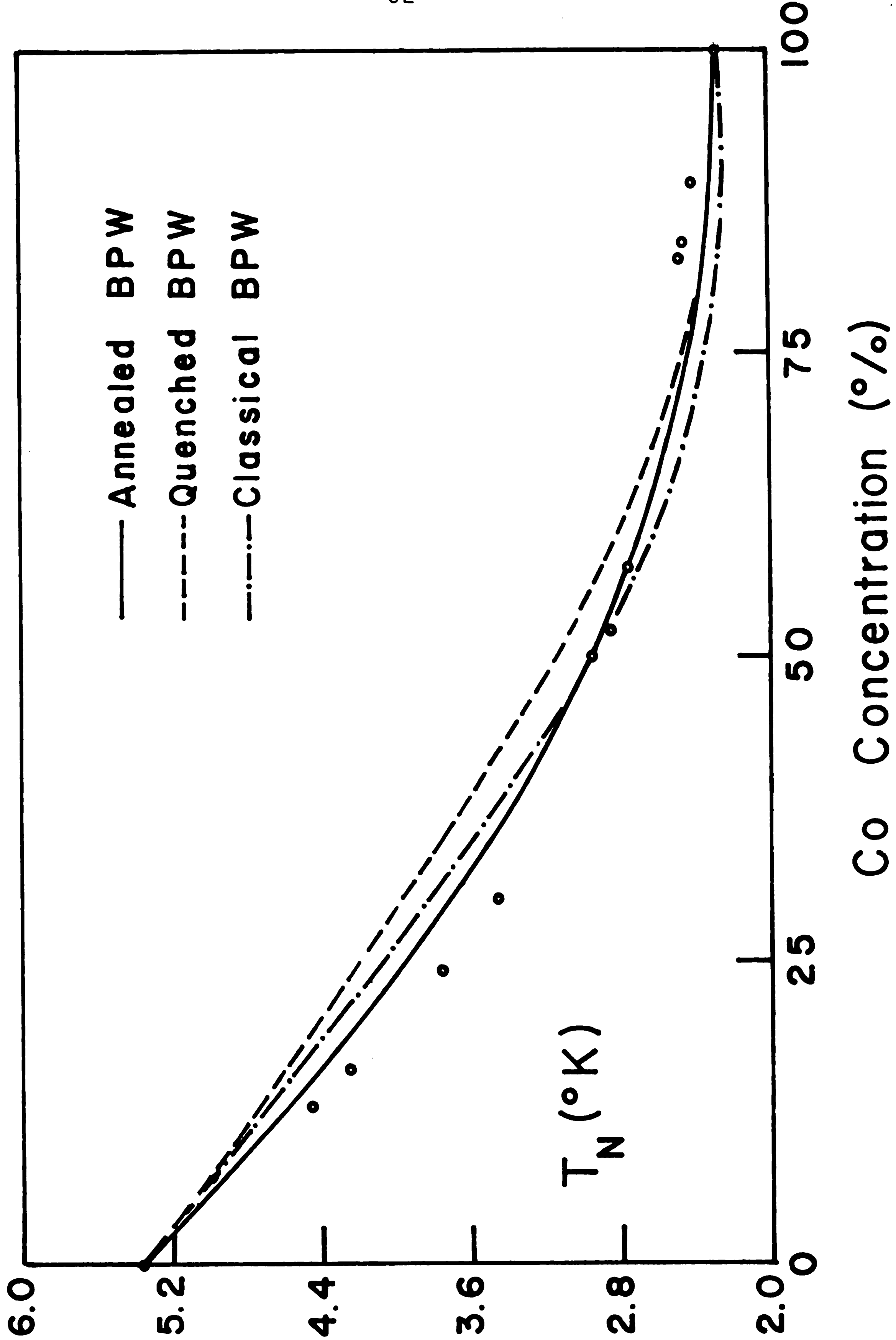
Annealed BPW
Quenched BPW
Classical BPW
T_N (°K)
6.0
5.2
4.4
3.6
2.8
2.0
0
25
50
75
100
Co Concentration (%)

Figure 13

crystal mean field models give similar critical temperatures. If the phase diagram of the quenched BPW model has been required to pass through the third fixed point ($T_N = 2.96°K$, $x = 0.5$), it would also give a shallow minimum near 100% Co, and would practically coincide with the classical Heisenberg BPW phase diagram for high Ni concentrations. Thus, making the spins go from $\frac{1}{2}$ to ∞ does not produce any significant change in the shape of the concentration phase diagram. In our opinion, the poor agreement between quenched BPW models and experimental critical temperatures is symptomatic of the fact that the BPW model does not describe the critical behaviors of $NiCl_2 \cdot 6H_2O$ and $CoCl_2 \cdot 6H_2O$ correctly. From this point of view, the apparent agreement between the annealed BPW model and experiment becomes more like a mathematical accident. Evidently, there are many ways in which ε_c and K_c can be chosen so as to make (3.8) "agree" with experiment. The simple cubic Ising model is a good example of this. Therefore, to gain more insight into the physics, one should also consider the ways in which the different theories fit the experimental specific heats. Before doing this, we will attempt to justify our fitting procedure for the concentration phase diagrams.

4. Choice of J_{Ni-Co}

Table III lists all the data points, along with the J_{Ni-Co} obtained by requiring the annealed square lattice Ising concentration phase diagram to pass through a particular point.

Table III

Values of J_{Ni-Co} obtained when the annealed 2-dimensional Ising concentration phase diagram is required to pass through a particular data point.

%Co	%Ni	T_N(°K)	J_{Ni-Co}(°K)
100	0	2.29	——
89	11	2.43	1.284
84	16	2.47	1.223
83	17	2.49	1.234
57	43	2.77	1.058
52	48	2.87	1.043
50	50	2.96	1.070
30	70	3.47	0.921
24	76	3.77	0.923
16	84	4.26	0.963
13	87	4.47	1.001
0	100	5.34	——

The average of all the J_{Ni-Co} is $\bar{J}_{Ni-Co} = 1.072 \pm 0.042°K$. A least squares fit of (3.8) through all the data points (except the 100% Co and 100% Ni points) give $J_{Ni-Co} = 1.032°K$, which is within the uncertainty range of $\bar{J}_{Ni-Co}$.

It seems then reasonable to choose (2.96°K, 50% Co) as the third fixed point since 2.96°K is itself an average over two runs, and also because the corresponding J_{Ni-Co} is very close to $\bar{J}_{Ni-Co}$. This will allow direct comparisons between the theoretical models without introducing unnecessary complications.

So far, we have taken J_{Ni-Ni}, J_{Co-Co} and J_{Ni-Co} to have the same sign. For the pure crystals, J_{Ni-Ni} and J_{Co-Co} are certainly both negative, and there seem to be no compelling physical reasons to assume J_{Ni-Co} positive. In this connection, it may be significant to note that with J_{Ni-Ni} and J_{Co-Co} assumed to have the same sign, and with the fixed points on the concentration phase diagram as chosen, the annealed Ising and BPW phase diagram equations (equations (3.8) and (3.9)) then require J_{Ni-Co} to have the same sign as J_{Ni-Ni} and J_{Co-Co}. On the other hand, the quenched BPW and mean field phase diagram equations allow J_{Ni-Co} to have both signs.

It is also instructive to consider the choice of J_{Ni-Co} from another point of view. Write the different exchange energies as $J_{AA}\vec{S}_A \cdot \vec{S}_A$; $J_{AB}\vec{S}_A \cdot \vec{S}_B$ and $J_{BB}\vec{S}_B \cdot \vec{S}_B$. If the J's arise from superexchange, then a simple argument given by Bacon et al.[40] leads one to expect that, as a first approximation

$$J_{AB}^2 = J_{AA}\, J_{BB} \tag{3.10}$$

Table IV lists the different J's obtained from the annealed Ising and BPW models, assuming $S_{Co} = 1/2$ and $S_{Ni} = 1$.

Table IV

Values of exchange constants in the Ising and BPW models

	J_{Co-Co} (°K)	J_{Ni-Ni} (°K)	J_{Ni-Co} (°K)	$\frac{J_{Ni-Co}}{\sqrt{J_{Ni-Ni}\, J_{Co-Co}}}$
Ising	4.036	2.353	2.140	0.69
BPW	3.176	1.851	1.564	0.65

As one can see, the agreement with (3.10) is not fantastic. Note however that (3.10) has been derived in a simple superexchange case [two magnetic ions separated by a diamagnetic ion]. It may not be valid when the superexchange goes through many diamagnetic groups as in $NiCl_2 \cdot 6H_2O$ and $CoCl_2 \cdot 6H_2O$. Also, strictly speaking, the J's listed in table IV correspond to the effective spins, not the "true" spins. As is well known, the effective J is related to the true J by the square of a g-tensor component.[38] By calculating the true J's correctly from the effective J's, it may be possible to find that the former will satisfy (3.10) more closely. One should add that even for "simpler" systems such as FeO - CoO oxides and rare earth alloys, other authors [Boubel et al.[16], Lindgård[45]] had found it necessary to impose significant deviations from (3.10).

C. Specific Heat Results

1. Comparisons between theoretical and experimental specific heats

Figures 14, 15, 16 show the theoretical and experimental specific heats for samples containing 89%, 50%, 13% Co respectively. They are the samples for which the most extensive sets of data have been taken. The data plotted have also been corrected for lattice specific heats, assuming a T^3 dependence for the latter (in the temperature range of interest, this correction amounts at most to a few percent). In Fig. 14, one sees that the annealed 2-dimensional Ising model agrees reasonably well with experiment below T_N, while, as expected, the annealed BPW model does not fit the data. In this case, the quenched BPW model with the same J_{Ni-Co} gives practically the same specific heat as the annealed BPW model, and is not shown on the graph for clarity.

In Fig. 15, the data start out by deviating systematically from the annealed Ising curve, up to about $0.8T/T_N$. Presumably, this is due to spin wave behavior. Beyond $0.8T/T_N$, critical behavior sets in, and the data follow the annealed Ising curve reasonably well, up to about 1.2 T/T_N. Note that although J_{Ni-Co} has been adjusted so that

Figure 14. Experimental and theoretical specific heats of $Ni_{0.11}Co_{0.89}Cl_2 \cdot 6H_2O$

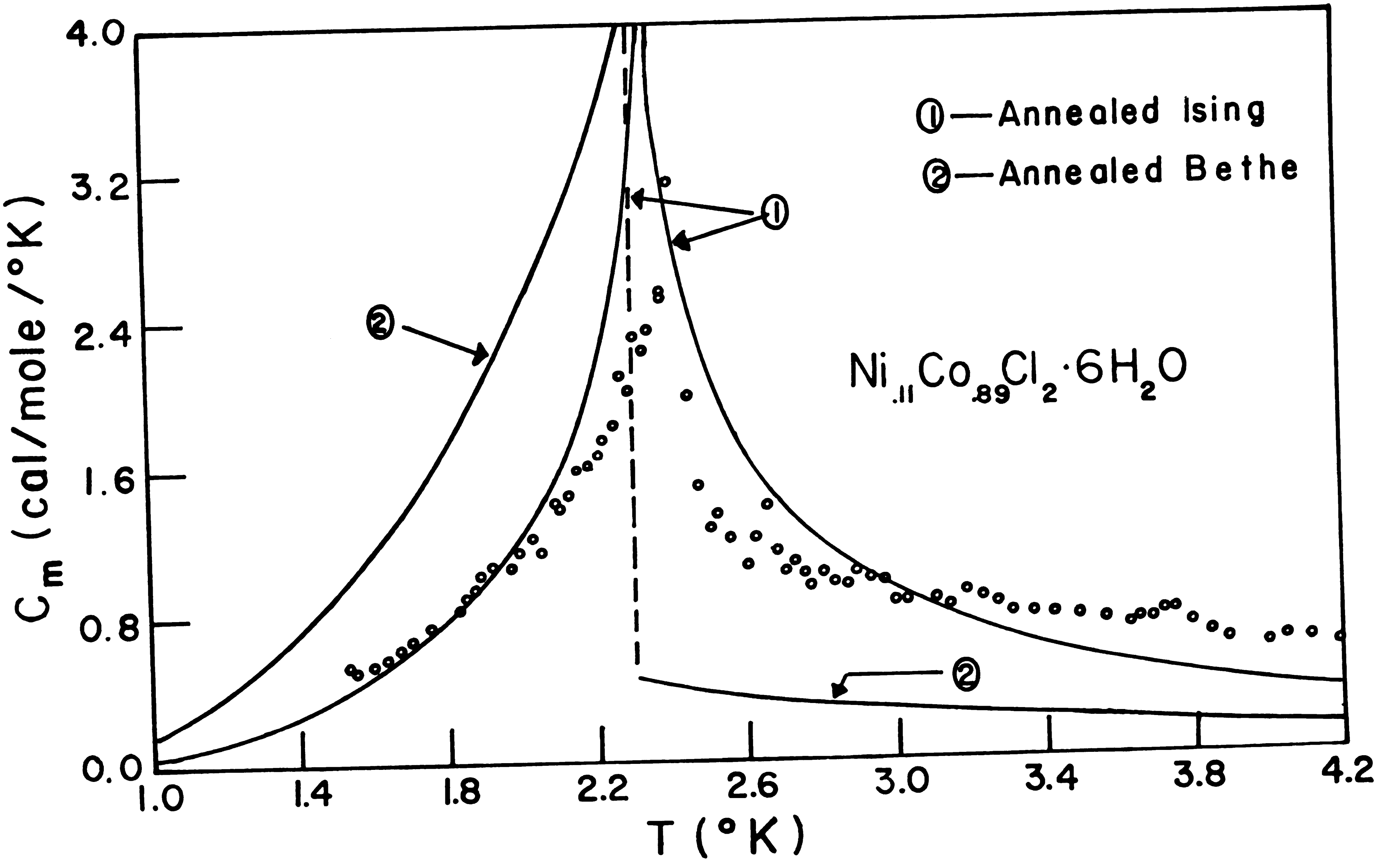
①—Annealed Ising
②—Annealed Bethe
$Ni_{.11}Co_{.89}Cl_2 \cdot 6H_2O$
①
②
②
C_m (cal/mole/°K)
4.0
3.2
2.4
1.6
0.8
0.0
1.0
1.4
1.8
2.2
2.6
3.0
3.4
3.8
4.2
T (°K)

Figure 14

Figure 15. Experimental and theoretical specific heats of $Ni_{0.50}Co_{0.50}Cl_2 \cdot 6H_2O$

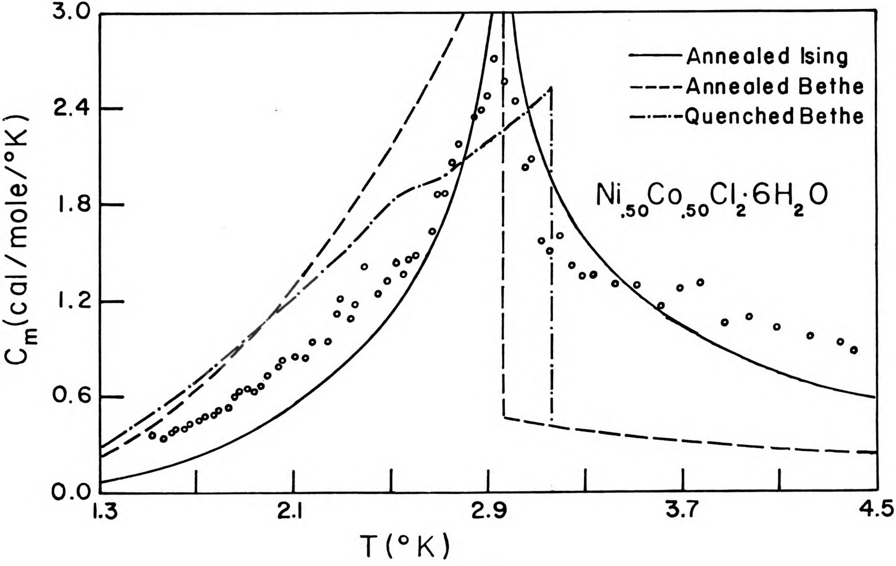
Annealed Ising
Annealed Bethe
Quenched Bethe
$Ni_{.50}Co_{.50}Cl_2 \cdot 6H_2O$
C_m(cal/mole/°K)
3.0
2.4
1.8
1.2
0.6
0.0
1.3
2.1
2.9
3.7
4.5
T(°K)

Figure 15

Figure 16. Experimental and theoretical specific heats of $Ni_{0.87}Co_{0.13}Cl_2 \cdot 6H_2O$

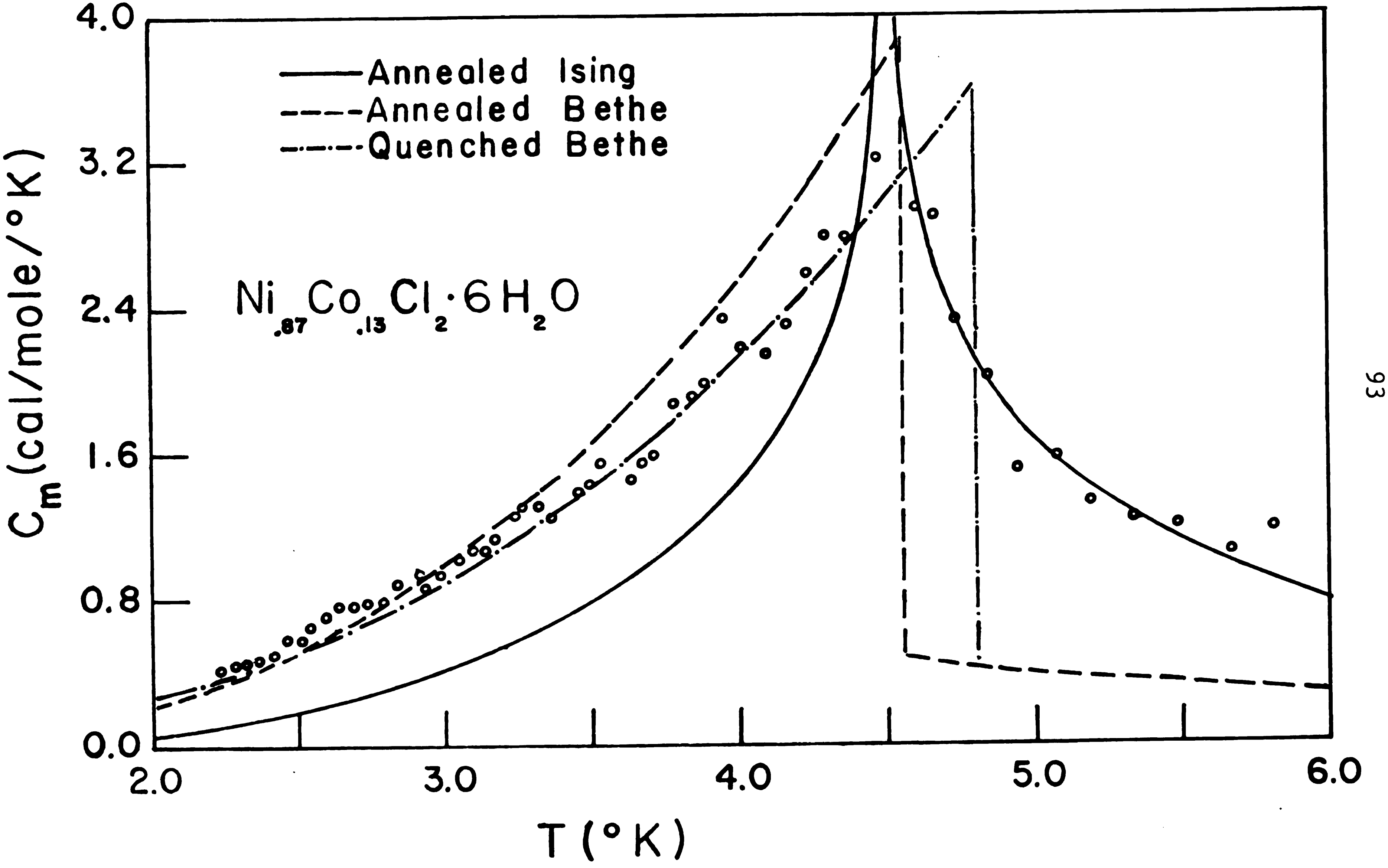

Annealed Ising
Annealed Bethe
Quenched Bethe
$Ni_{.87}Co_{.13}Cl_2 \cdot 6H_2O$
C_m (cal/mole/°K)
4.0
3.2
2.4
1.6
0.8
0.0
2.0
3.0
4.0
5.0
6.0
T (°K)

Figure 16

the annealed BPW model gives the experimental critical temperature 2.96°K, it does not fit the data as well as the quenched BPW model with the same J_{Ni-Co}. However, the quenched BPW specific heat curve exhibits a peculiar shoulder at around 2.5°K. This is probably an artifact of the quenched BPW model at 50% concentration.

One can now predict beforehand the behavior of the data with respect to theory in fig. 16. As expected, below T_N, the data agree with the annealed Ising curve only very near T_N. Above T_N, the agreement "area" covers a wider temperature range. Below T_N, the quenched BPW model fits the data fairly well, but the critical temperature it predicts is too high.

In summary, among the theoretical models considered, the annealed two dimensional Ising fits experimental data the best in the critical region. Although it predicts the T_N vs. concentration fairly well, the annealed BPW model does not fit the data as well as its quenched counterpart. The overall behavior of the data with respect to the random Ising and BPW models is what one might qualitatively predict, by looking at fig. 9 and assuming that the Ni and Co ions are randomly distributed on the lattice. Also, it appears that the exchange constants J_{Co-Co}, J_{Ni-Co}, J_{Ni-Ni} do not change appreciably with concentration. Since superexchange can depend sensitively on atomic distances and bond angles, this may mean that the latter do not change significantly with concentration. Detailed crystallographic work will be needed to confirm this.

2. Entropy calculation

We have also carried out total magnetic entropy change calculations for the three samples considered. The paramagnetic specific heats in the random Ising and BPW models are dominated by $1/T^2$ terms. A Green's function calculation shows that this is also the case for the pure Heisenberg paramagnet.[50] It seems therefore reasonable to assume that sufficiently above T_N, the total specific heats of the mixed crystals will be well approximated by

$$C_{ToT} = \frac{A}{T^2} + BT^3 \tag{3.11}$$

The second term is the lattice specific heat which we assume to have a T^3 dependence.

We can then calculate the total magnetic entropy change ΔS in the standard way.[32] Theoretically, ΔS is simply given by

$$\Delta S = R[p \ln (2S_{Co} + 1) + (1-p)\ln(2S_{Ni} + 1)] \tag{3.12}$$

p = fraction of Co

S_{Co} and S_{Ni} denote the effective spins of Co^{++} and Ni^{++}.
Table V lists the experimental and expected entropies.

Table V

Experimental and theoretical total magnetic entropy changes

%Co	ΔS_{th} (cal/mole/°K)	ΔS_{exp} (cal/mole/°K)
89	1.42	1.47
50	1.79	1.79
13	1.91	2.09

In table V, ΔS_{th} has been calculated by assuming $S_{Co} = \frac{1}{2}$ and $S_{Ni} = 1$. The agreement between the theoretical and experimental ΔS may be considered satisfactory given the uncertainties in entropy calculations. (for 13% Co, the main uncertainty comes in the estimation of the A/T^2 term)

Thus, entropy calculation suggest that the Ni^{++} and Co^{++} ions retain their "pure" effective spins in the mixed crystals. Fig. 17 shows the normalized entropy curves for the three mixed crystals. Note that only about 50% of the total entropy $S(\infty) = \Delta S$ is gained up to T_N, just as in the pure crystals.

3. Validity of the annealed models

An annealed bond Ising model can, at best, provide a good approximation to the thermodynamical behavior of mixtures of magnetic insulators. Recently, Harris[51] has shown

Figure 17. Normalized magnetic entropy for three Co concentrations. The Neel temperatures are indicated by arrows.

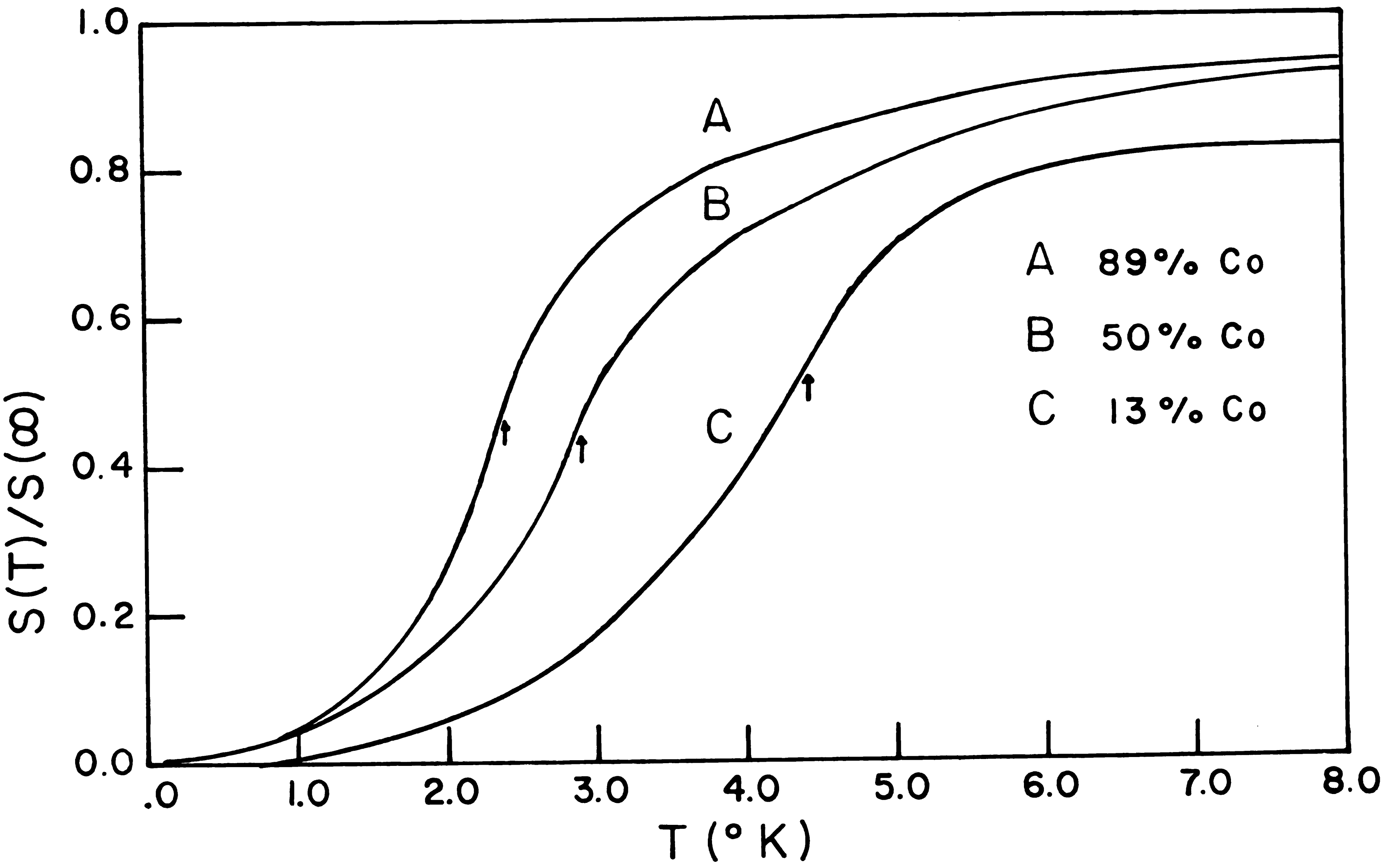
1.0
0.8
0.6
0.4
0.2
0.0
S(T)/S(∞)
.0
1.0
2.0
3.0
4.0
5.0
6.0
7.0
8.0
T (° K)
A
B
C
A 89% Co
B 50% Co
C 13% Co

Figure 17

that, at least as far as the T_c vs. concentration diagram is concerned, a CPA (Coherent Potential Approximation) calculation on the quenched site Ising system gives the same answer as the annealed bond Ising model. For Ising systems, many other theoretical comparisons between the annealed and quenched models have also been carried out.[4,52] The results of these studies suggest that there are probably no significant differences between the two, when all the interactions have the same sign. The greatest differences occur in the critical region. When antiferromagnetic and ferromagnetic bonds are allowed to mix, substantial differences between the two approaches do arise. As a notable example of this, the annealed Ising model does not allow a spin glass state to occur.[4]

These general conclusions appear to be qualitatively borne out by the detailed comparisons we have made between the annealed and quenched BPW models. At sufficiently high temperatures, both models give the same specific heat. But below T_N, the quantitative agreement is rather poor, except when the two models happen to give the same critical temperature. The concentration phase diagram of the quenched BPW model lies systematically higher than that of the annealed BPW model.

In chapter I (section 5), we have given a general expression for a quantity "c", which may be interpreted as a measure of the fluctuation of a bond occupation probability around its average value. In Fig. 18, we have plotted "c"

Figure 18. Fractional mean square fluctuations of the distribution functions for the three possible bonds in the annealed Ising and BPW models. Note that the right hand scale is ten times larger than the left hand scale.

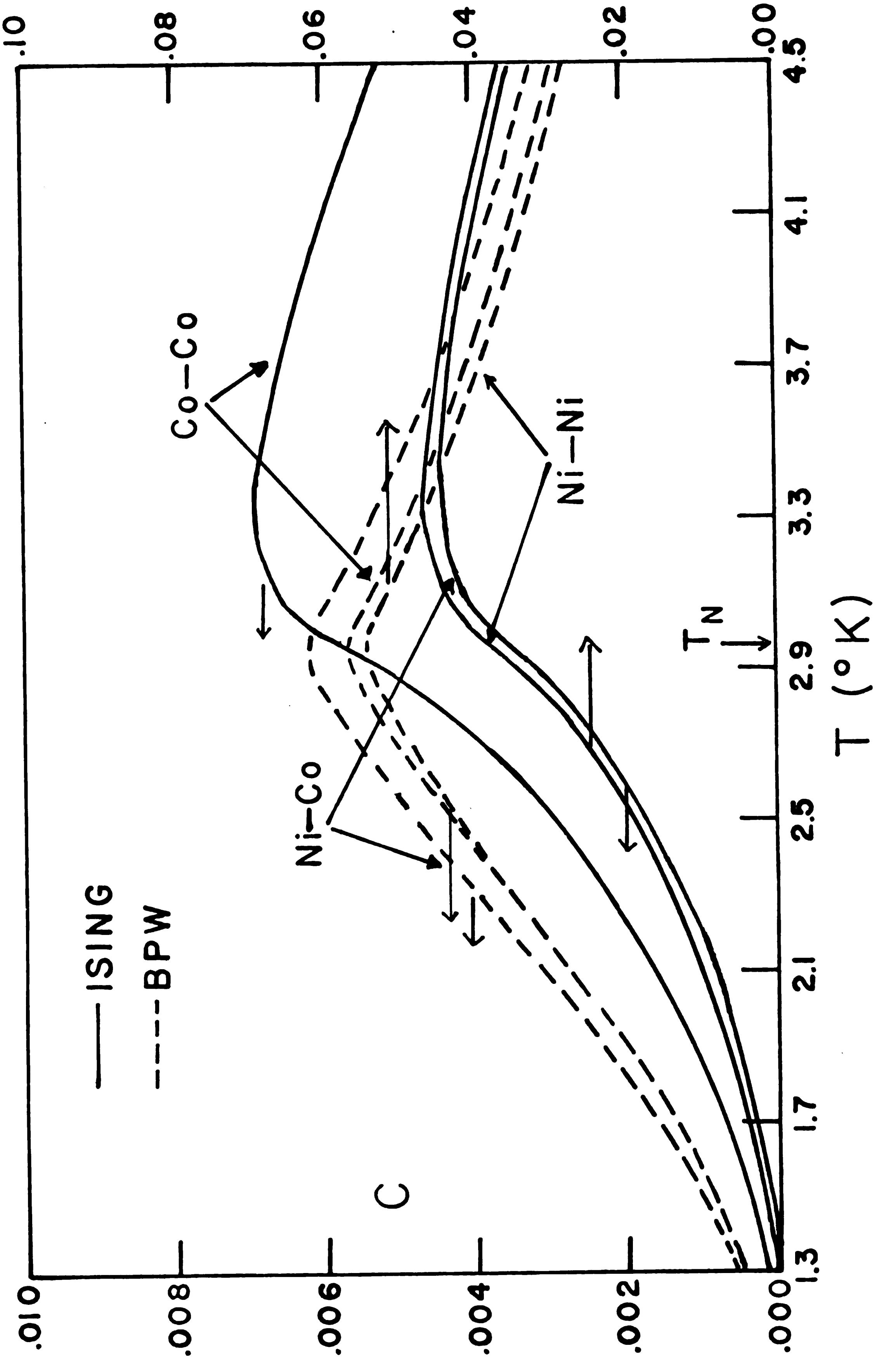
ISING
BPW
C
Co—Co
Ni—Co
Ni—Ni
T_N
T (°K)
1.3
1.7
2.1
2.5
2.9
3.3
3.7
4.1
4.5
.000
.002
.004
.006
.008
.010
.00
.02
.04
.06
.08
.10

Figure 18

for all three possible bonds, as given by the annealed Ising and BPW models in the case of 50% Co concentration. As expected, the magnitudes of the c's remain small (5% at most) and reach maximas near the critical temperature. Note that below T_N, the BPW curves lie systematically higher than the corresponding Ising curves. Similar conclusions can be drawn for 13% and 89% Co concentrations. This tends to suggest that the relatively substantial quantitative disagreements between the annealed and quenched BPW models below T_N are due to some peculiarity in the BPW approximation itself. A more qualitative, but perhaps more convincing argument lies in the fact that the annealed BPW model does not fit the specific heat data as well as the quenched BPW model, while the annealed Ising model already fits the same data in the "expected" manner.

4. Low temperature behavior

In Fig. 19, we have plotted C/T^3 vs. T/T_N for three different Co concentrations. There is some scatter, especially at high Co concentration, but it appears that the specific heats of all three samples follow a T^3 law, i.e.

$$C = \alpha T^3 \tag{3.13}$$

between 0.5 T/T_N and 0.75 T/T_N. For high Ni concentration, the T^3 dependence apparently persists even up to 0.9 T/T_N. Note that pure $CoCl_2 \cdot 6H_2O$ and $NiCl_2 \cdot 6H_2O$ also follow a T^3 law in roughly the same range of T/T_N.[41] This suggests

Figure 19. C/T^3 vs. T/T_N for three different Co concentrations

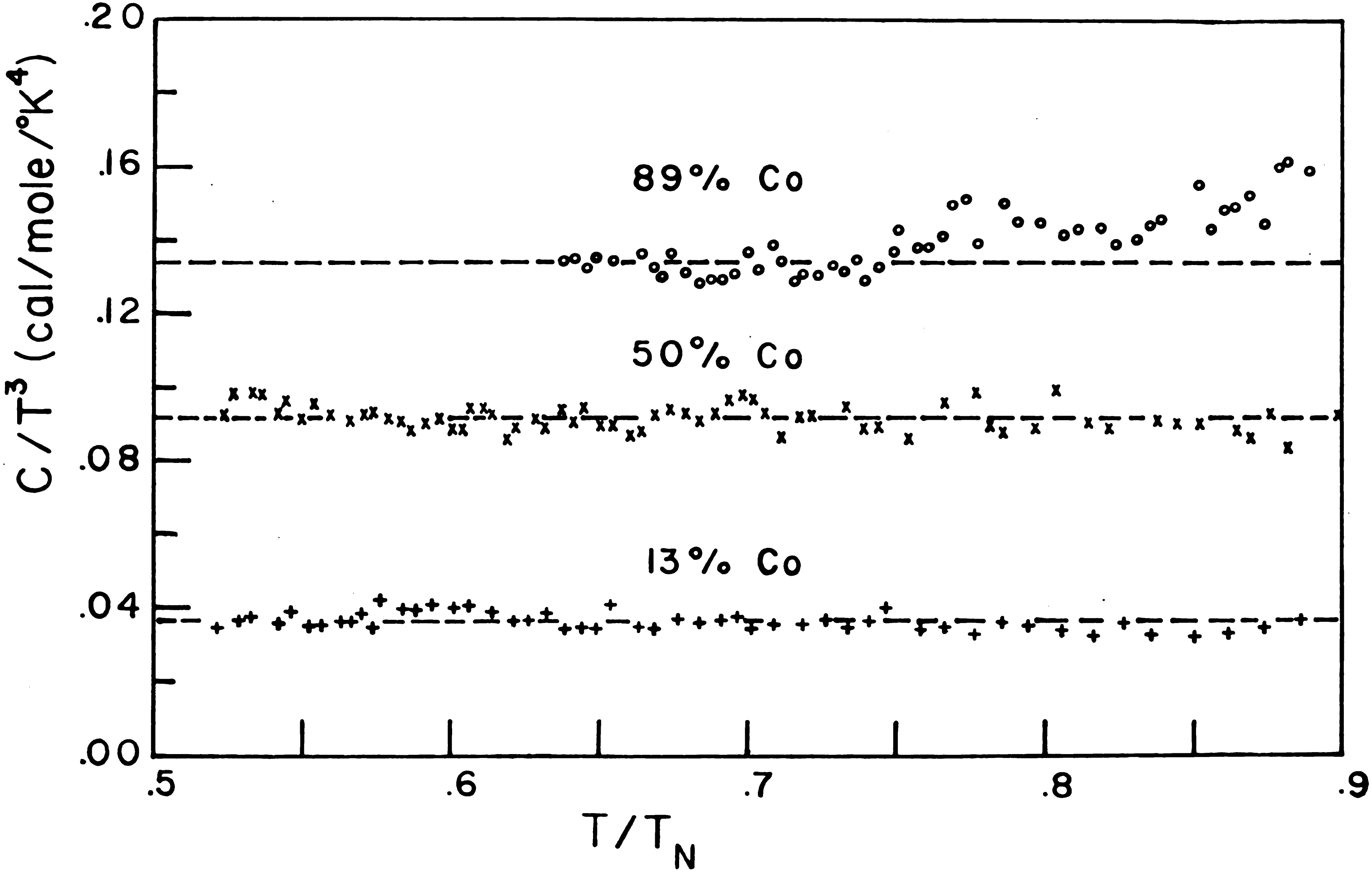

Figure 19

some sort of "scaling" of the spin wave spectrum.

For pure crystals, the spin wave coefficient α in (3.13) depends mainly on the crystal structure, and also on the exchange constant.[42] In Fig. 20, we have plotted α vs. concentration. To within the accuracies of the calculations, a linear variation of α with concentration is thereby suggested. A full interpretation of this awaits the development of a spin wave theory of mixed anisotropic Heisenberg antiferromagnets.

D. Magnetic Phase Diagram

Our interpretation of the magnetic phase diagram is based upon the magnetocaloric equation[53]

$$\frac{dT}{dH} = -\frac{TH}{C_H}\left(\frac{\partial \chi}{\partial T}\right)_H \qquad (3.14)$$

where

H = magnetic field

C_H = specific heat at constant field

χ = susceptibility

Suppose the field is aligned along the easy axis and increased adiabatically. In the antiferromagnetic state, the appropriate χ is χ_{11}, the parallel susceptibility. Since $\frac{\partial \chi_{11}}{\partial T} > 0$, the temperature T decreases. When the spins have flopped, the perpendicular susceptibility $\chi_\perp$ should be used in (3.13). According to the molecular field theory $\chi_\perp$ is a constant. Thus, the temperature should stay constant.

Figure 20. Spin wave coefficient α vs. Co concentration

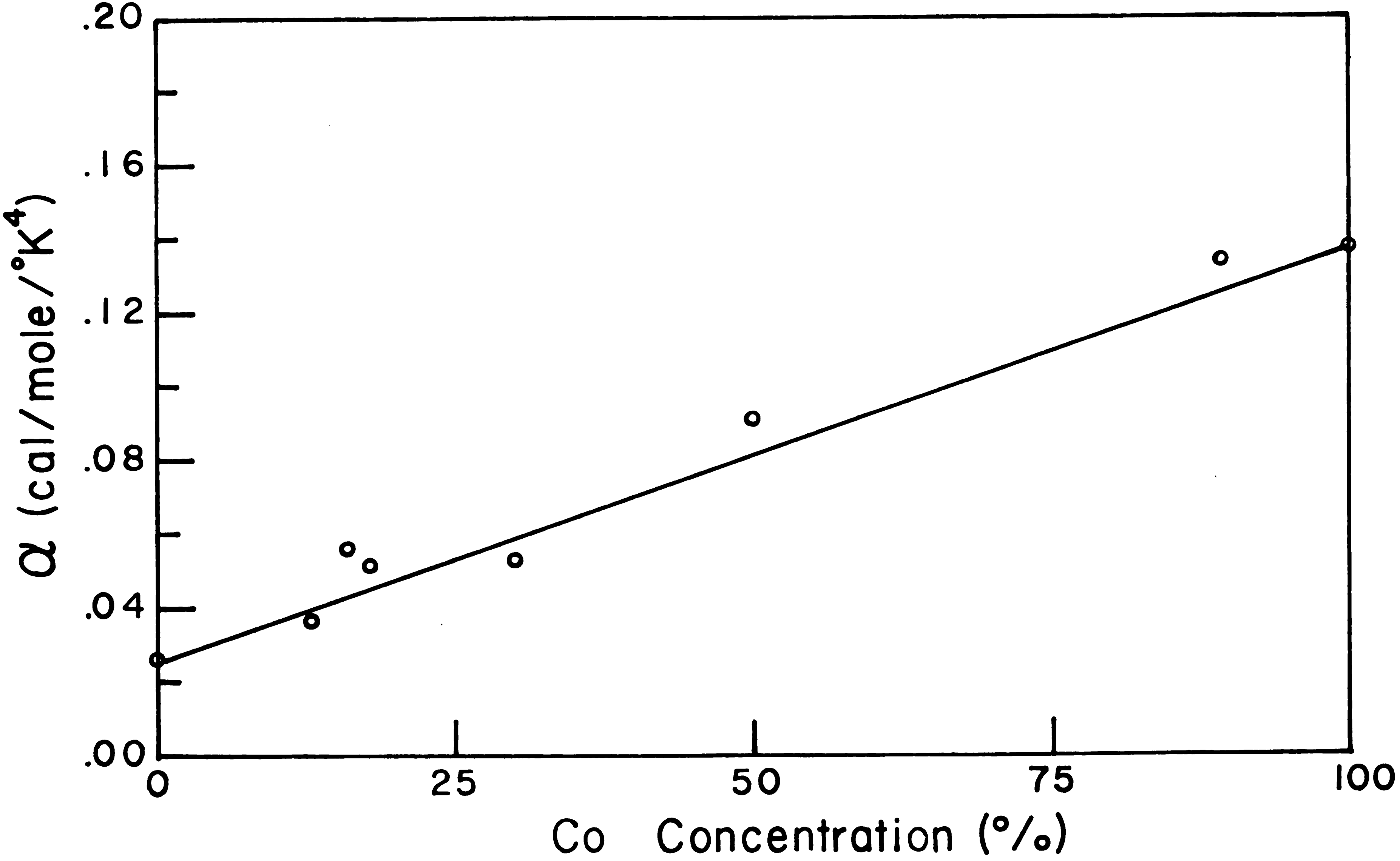

Figure 20

This allows a determination of the antiferromagnetic spin flop boundary using the procedures described in chapter II (section 5). The data points taken in this way are shown on the low temperature side of Fig. 21. (The data points on the high temperature side represent the antiferromagnetic-paramagnetic boundary for 57% Co).

H_{AF-SF} (0), the antiferromagnetic spin flop critical field at 0°K has been determined by Rives and Bhatia[54] as 6.6KG for $CoCl_2 \cdot 6H_2O$. The corresponding field in $NiCl_2 \cdot 6H_2O$ is considerably higher: 39.6KG.[55] The range between those two numbers may help to understand fig. 21 qualitatively. We note that for 57% Co, the critical fields are lower or comparable to the corresponding fields in $CoCl_2 \cdot 6H_2O$. This suggests that the anisotropies of the Ni^{++} and Co^{++} ions have not changed, even up to a fairly high degree of mixing. For 50% Co, the AF-SF boundary begins to rise substantially above the $CoCl_2 \cdot 6H_2O$ boundary. Qualitatively, one may say that some Ni^{++} spins have begun to flop. It may also be significant to note that the boundary curvature for both concentrations appears more pronounced than in $CoCl_2 \cdot 6H_2O$.

Among the many theories which can be brought to bear on this problem, the simplest is probably a recent treatment of the diluted anisotropic antiferromagnet by Moreira et al.[56] Basically, theirs is a generalization of the standard molecular field theory of the pure anisotropic antiferromagnet. They assume virtual crystal approximation and single ion uniaxial anisotropies which do not change with concentration.

Figure 21. Tentative magnetic phase diagram for two different Co concentrations

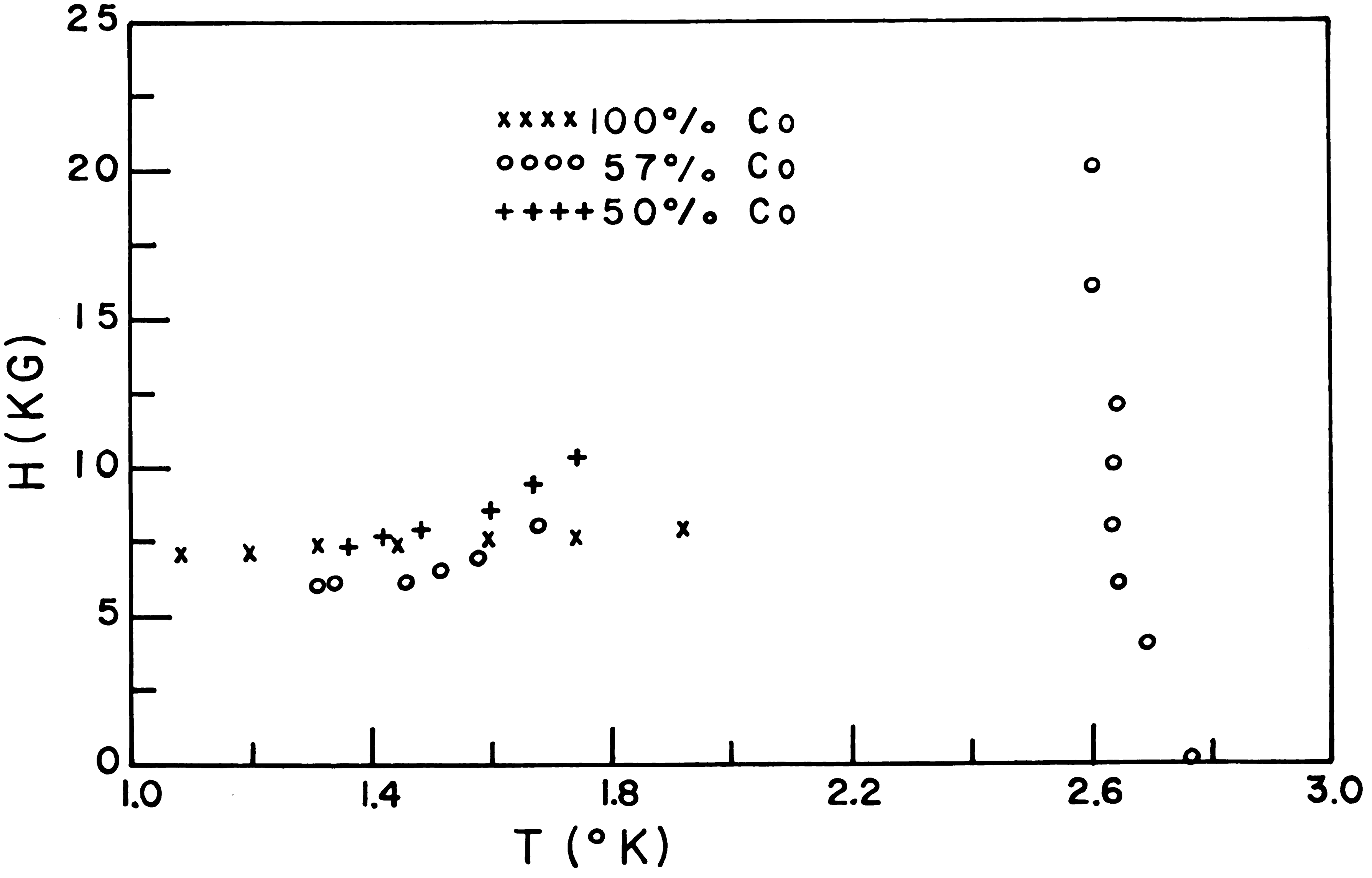
xxxx 100°/o Co
oooo 57°/o Co
++++ 50°/o Co
H (KG)
25
20
15
10
5
0
1.0
1.4
1.8
2.2
2.6
3.0
T (°K)

Figure 21

We have not attempted this, but it seems reasonably straight forward to extend the approach of ref. 56 to the case of mixed crystals, assuming the spins to be distributed on two distinct sublattices and oriented along the same easy axis. Although the virtual crystal approximation does not work well in the case of short range interactions, this approach may provide a first step towards a quantitative understanding of the phase diagram.

Finally, we should mention that in one respect, there is some difficulty in the interpretation of our data as critical AF-SF fields. According to a simple mean field theory developed in ref. 53, the temperature should exhibit a minimum at the easy axis, when the field is rotated around the easy axis in the antiferromagnetic state. The minumum should become a maximum in the spin flop state. This effect is quite evident in $CoCl_2 \cdot 6H_2O$. However, for 57% Co we observe no changeover from minimum to maximum above the critical field. This may mean that the rotation may not have been done in the plane where the spins have flopped, or that the theory of ref. 53 needs to be revised for the case of mixed crystals. At any rate, the magnetic phase diagrams of fig. 21 can only be considered as tentative. Further speculations should await experimental work on single crystals over a wider range of compositions.

E. Conclusions

We have performed a fairly extensive zero field calorimetric study of $Co_xNi_{1-x}Cl_2 \cdot 6H_2O$ over a wide range of compositions. The critical behaviors of the mixed crystals have been found to be reasonably well described by the annealed two dimensional Ising model. This is probably due to the fact the that specific heats of both $NiCl_2 \cdot 6H_2O$ and $CoCl_2 \cdot 6H_2O$ exhibit Ising-like behaviors in the critical region.

The fact that the annealed BPW model happens to fit the concentration fairly well has prompted us to carry out a detailed comparison between the quenched and annealed BPW models. The results of this comparison show that relatively substantial quantitative differences exist between the two models below T_N. From a consideration of the fluctuations in the bond occupation probabilities introduced by the annealing process, it is argued that these quantitative differences are probably due to some intrinsic feature of the BPW approximation. It is likely that the exact quenched Ising model will not provide an improvement over the annealed Ising model.

Apart from the assumption of Ising spins, we have also made the following implicit assumptions in our analysis of the data:

a.) the exchange constants are antiferromagnetic and do not change with concentration

b.) the magnetic structure is a simple interpenetrating two sublattice structures with all spins directed along the same easy axis (which may vary with concentration).

The Ising spins assumption will break down at low temperatures. But it seems reasonable to assume that a) and b) will continue to hold. Neutron diffraction, or NMR studies are needed to confirm b).

Assuming a) and b), it should be relatively straightforward to extend spin wave and molecular field theories, as a first step in accounting for the low temperature behavior of the specific heat and the magnetic phase diagram.

Good quality single crystals of different compositions needed to be grown to allow detailed measurements under magnetic fields. High resolution calorimetric studies may provide a good testing ground for current theoretical ideas about the critical indices of random systems.

REFERENCES

REFERENCES

1. Y. Osaka and T. Yaginuma, Bull. Chem. Soc. Jpn. 3, 4 (1928).
2. R. Brout, Phys. Rev. 115, 824 (1959).
3. J. S. Smart, Effective Field Theories of Magnetism, (W. B. Saunders, Philadelphia, 1966).
4. M. F. Thorpe and D. Beeman, Phys. Rev. B 14, 188 (1976).
5. I. Syozi and S. Miyazima, Prog. Theor. Phys. 36, 1083 (1966).
6. S. Miyazima and K. Yonezawa, Prog. Theor. Phys. 51, 99 (1974).
7. E. Ising, Z. Phys. 31, 153 (1925).
8. S. Katsura and F. Matsubara, Can. J. Phys. 52, 120 (1974).
9. L. Onsager, Phys. Rev. 65, 117 (1944).
10. H. A. Bethe, Proc. Roy. Soc. 150, 552 (1935).
11. R. Peierls, Proc. Roy. Soc. 154, 207 (1936).
12. P. R. Weiss, Phys. Rev. 74, 1498 (1948).
13. S. Katsura and M. Takizawa, Prog. Theor. Phys. 51, 82 (1974).
14. F. Matsubara, Prog. Theor. Phys. 51, 378 (1974).
15. T. P. Eggarter, J. Stat. Phys. 11, 363 (1974).
16. M. A. Boubel, R. P. Mainard, H. G. Fousse, A. J. Pointon and F. R. Jeannot, Phys. Stat. Sol. 35, 459 (1976).
17. S. Katsura, Can. J. Phys. 53, 854 (1975).
18. N. D. Love, Ph.D. dissertation, Michigan State University (1967).

19. P. T. Bailey, Ph.D. dissertation, Michigan State University (1971).

20. F. G. Brickwedde, H. van Dejk, M. Durieux, J. R. Clement, and J. K. Logan, J. Res. Nat. Bur. Stand. 64A, 1 (1960).

21. J. R. Clement and E. H. Quinnel, Rev. Sci. Instr. 23, 213 (1952).

22. J. Mizuno, J. Phys. Soc. Jpn. 15, 1412 (1960).

23. J. Mizuno, J. Phys. Soc. Jpn. 16, 1574 (1960).

24. R. Kleinberg, J. Chem. Phys. 53, 2660 (1970).

25. R. Kleinberg, J. Appl. Phys. 38, 1453 (1967).

26. A. Abragam and M. H. L. Pryce, Proc. Roy. Soc. A 205, 135 (1951).

27. J. S. Griffith, The Theory of Transition Metal Ions, (Cambridge University Press, 1964) p. 333.

28. R. Schlapp and W. G. Penney, Phys. Rev. 42, 666 (1932).

29. A. I. Hamburger and S. A. Friedberg, Physica 69, 67 (1973).

30. T. Iwashita and N. Uryu, J. Phys. Soc. Jpn., 38, 58 (1975).

31. I. Kimura, J. Phys. Soc. Jpn. 30, 1603 (1971).

32. W. K. Robinson and S. A. Friedberg, Phys. Rev. 117, 402 (1960).

33. C. Domb, Adv. Phys. 9, 149 (1960).

34. T. Obokata and T. Oguchi, J. Phys. Soc. Jpn. 25, 322 (1968).

35. J. Skalyo, Jr., and S. A. Friedberg, Phys. Rev. Lett. 13, 133 (1964).

36. W. L. Johnson and W. Reese, Phys. Rev. B 2, 1355 (1970).

37. R. F. Wielinga, H. W. J. Blöte, J. A. Roest and W. J. Huiskamp, Physica 34, 223 (1967).

38. L. J. de Jongh and A. R. Miedema, Adv. Phys. 23, 1 (1974).

39. R. J. Birgeneau, J. Als Nielsen and G. Shirane, Phys. Rev. B 16, 280 (1977).

40. L. J. de Jongh, D. D. Betts and D. J. Austen, Sol. Stat. Comm. 15, 1711 (1974).

41. R. H. Donaldson and D. T. Edmonds, Proc. Phys. Soc. 85, 1209 (1965).

42. J. A. Eisele and F. Keffer, Phys. Rev. 96, 929 (1954).

43. T. Iwashita and N. Uryu, J. Phys. Soc. Jpn. 39, 36 (1975).

44. T. Haseda, J. Phys. Soc. Jpn. 15, 483 (1960).

45. P. A. Lindgård, Phys. Rev. B 14, 4074 (1976).

46. W. A. Robinson and W. W. Simmons, Bull. Am. Phys. Soc. 10, 1201 (1965).

47. K. Takeda, M. Matsuura and T. Haseda, J. Phys. Soc. Jpn. 29, 885 (1970).

48. M. F. Sykes, D. L. Hunter, D. S. McKenzie and B. R. Heap, J. Phys. A 5, 667 (1972).

49. G. E. Bacon, R. Street and R. H. Tredgold, Proc. Roy. Soc. A 217, 252 (1953).

50. K. Fujii, S. Kadowaki, I. Mannari, Prog. Theor. Phys. 50, 74 (1973).

51. A. B. Harris, J. Phys. C 9, 2512 (1976).

52. D. C. Rapaport, J. Phys. C 5, 1830 (1972).

53. J. N. McElearney, Ph. D. dissertation, Michigan State University (1967).

54. J. E. Rives and S. N. Bhatia, Phys. Rev. B 12, 1920 (1975).

55. C. C. Becerra and A. P. Filho, Phys. Lett. 44A, 13 (1973).

56. F. G. B. Moreira, I. P. Fittipaldi, S. M. Rezende, R. A. Tahir Kheli and B. Zeks, Phys. Stat. Sol. 80, 385 (1977).

APPENDIX

```
C----PHASE DIAGRAM OF THE PLANAR ANNEALED ISING MODEL-----
      WRITE (4,3)
    3 FORMAT(1X,TA AND TB ?'$)
      READ (4,5) TA,TB
    5 FORMAT (2F10.3)
    2 CONTINUE
      B = 1./SQRT(2.)
      A = 1.0+B
      TEM = ALOG(1.0+SQRT(2.))/2.
      VJA = TA*TEM
      VJB = TB*TEM
      WRITE (4,27)
   27 FORMAT(1X,'VALUE OF JAB ?'$)
      READ (4,17) VJAB
   17 FORMAT(F10.3)
      IF (VJAB.NE.0.) GO TO 6
      WRITE (4,7)
    7 FORMAT (1X,'TEMP. AND CONC. FOR FIT ?'$)
      READ (4,5) TC,XC
      Q = 1.-XC
      U = 0.5-(XC*XC)/(A+B*EXP(-2.*VJA/TC))-(Q*Q)/(A+B*EXP(-2.*VJB/TC))
      TEM = B/(2.*XC*Q/U-A)
      VJAB = TC*ALOG(TEM)/2.
    6 CONTINUE
      XO = 0.007
      WRITE (4,11) VJA,VJB,VJAB
   11 FORMAT(1X,'JAA =',F10.3,5X,'JBB =',F10.3,5X,'JAB =',F10.3)
      DO 20 I = 1,21
      P = (I-1)/20.
      Q = 1.0-P
      P2 = P*P
      Q2 = Q*Q
      PQ2 = 2.0*P*Q
      ITER = 0
   10 CONTINUE
      DENA = A+B*EXP(-XO*VJA)
      DENB = A+B*EXP(-XO*VJB)
      DENAB = A+B*EXP(-XO*VJAB)
      FCT = P2/DENA + PQ2/DENAB + Q2/DENB -0.5
      DFCT = VJA*P2*EXP(-XO*VJA)/(DENA*DENA)
      DFCT = DFCT+VJAB*PQ2*EXP(-XO*VJAB)/(DENAB*DENAB)
      DFCT = B*(DFCT+VJB*Q2*EXP(-XO*VJB)/(DENB*DENB))
      XINC = FCT/DFCT
      IF (ABS(XINC/XO).LE.1.E-6) GO TO 14
      ITER = ITER+1
      XO = XO-XINC
      IF(ITER.LE.40) GO TO 10
      WRITE(4,15)
   15 FORMAT(1X,'TOO MANY ITERATIONS !')
      GO TO 40
```

```
14 TEMP = 2./(X0-XINC)
   WRITE (4,21) P,Q,TEMP
21 FORMAT(3(5X,F10.3))
20 CONTINUE
40 PAUSE
   GO TO 2
   END
```

```
C------PHASE DIAGRAM IN THE ANNEALED BPW MODEL---------
      WRITE (4,3)
    3 FORMAT(1X,'TA AND TB ?'$)
      READ (4,5) TA,TB
    5 FORMAT(2F10.3)
    2 CONTINUE
      WRITE(4,11)
   11 FORMAT(1X,'NO. OF NEAREST NBRS ?'$)
      READ (4,15) ZN
   15 FORMAT(F10.3)
      ZN1 = 1./( ZN-1.)
      WRITE(4,17)
   17 FORMAT(1X,'TEMP. AND CONC. FOR FIT ?'$)
      READ (4,5) TC,P
      Q = 1.-P
      TEM = ALOG(ZN/(ZN-2.))/2.
      VJAA = TA*TEM
      VJBB = TB*TEM
      IF(TC.EQ.0.) GO TO 6
      THAA = TANH(VJAA/TC)
      THBB = TANH(VJBB/TC)
      THAB = (ZN1-P*P*THAA-Q*Q*THBB)/(2.*P*Q)
      VJAB =TC* ALOG((1.+THAB)/(1.-THAB))/2.
      GO TO 8
    6 WRITE (4,35)
   35 FORMAT(1X,'ENTER JAB ='$)
      READ (4,15) VJAB
      IF (VJAB.EQ.0.) VJAB = SQRT(VJAA*VJBB)
    8 CONTINUE
      WRITE (4,21) VJAA,VJBB,VJAB
   21 FORMAT(1X,'JAA =',F10.3,5X,'JBB =',F10.3,5X,'JAB =',F10.3)
      WRITE (4,19)
   19 FORMAT(1X,'INITIAL GUESS ?'$)
      READ (4,15)X0
      DO 20 I =1,21
      P = (I-1)/20.
      Q = 1.-P
      ITER = 0
   10 CONTINUE
      THAA = TANH(X0*VJAA)
      THBB = TANH(X0*VJBB)
      THAB = TANH(X0*VJAB)
      FCT= P*P*THAA+Q*Q*THBB+2.*P*Q*THAB-ZN1
      DFCT=P*P*VJAA*(1.-THAA*THAA)+Q*Q*VJBB*(1.-THBB*THBB)
      DFCT=DFCT+2.*P*Q*VJAB*(1.-THAB*THAB)
      XINC = FCT/DFCT
      IF (ABS(XINC/X0).LE.1.E-6) GO TO 14
      ITER = ITER+1
      X0 = X0-XINC
      IF (ITER.LE.40) GO TO 10
```

```
   WRITE (4,25)
25 FORMAT(1X,'TOO MANY ITERATIONS !')
   GO TO 40
14 TEMP = 1./(XO-XINC)
   WRITE (4,31) P,Q,TEMP
31 FORMAT(3(5X,F10.3))
20 CONTINUE
40 PAUSE
   GO TO 2
   END
```

```
C-----PHASE DIAGRAM IN THE QUENCHED BPW MODEL---------
      WRITE (4,3)
    3 FORMAT(1X,'TA AND TB ?'$)
      READ (4,5) TA,TB
    5 FORMAT(2F10.3)
    2 CONTINUE
      WRITE(4,11)
   11 FORMAT(1X,'NO. OF NEAREST NBRS ?'$)
      READ (4,15) ZN
   15 FORMAT(F10.3)
      ZN1 = ZN-1.
      WRITE(4,17)
   17 FORMAT(1X,'TEMP. AND CONC. FOR FIT ?'$)
      READ (4,5) TC,P
      WRITE (4,19)
   19 FORMAT(1X,'INITIAL GUESS ?'$)
      READ (4,15)X0
      Q = 1.-P
      TEM = ALOG(ZN/(ZN-2.))/2.
      VJAA = TA*TEM
      VJBB = TB*TEM
      IF(TC.EQ.0.) GO TO 6
      THAA = TANH(VJAA/TC)
      THBB = TANH(VJBB/TC)
      THAB = (1.-P*ZN1*THAA)*(1.-Q*ZN1*THBB)/(ZN1*ZN1*P*Q)
      THAB = SQRT(THAB)
      VJAB =TC* ALOG((1.+THAB)/(1.-THAB))/2.
      GO TO 8
    6 WRITE (4,35)
   35 FORMAT(1X,'ENTER JAB ='$)
      READ (4,15) VJAB
      IF (VJAB.EQ.0.) VJAB = SQRT(VJAA*VJBB)
    8 CONTINUE
      WRITE (4,21) VJAA,VJBB,VJAB
   21 FORMAT(1X,'JAA =',F10.3,5X,'JBB =',F10.3,5X,'JAB =',F10.3)
      DO 20 I =1,21
      P = (I-1)/20.
      Q = 1.-P
      ITER = 0
   10 CONTINUE
      THAA = TANH(X0*VJAA)
      THBB = TANH(X0*VJBB)
      THAB = TANH(X0*VJAB)
      FCT=ZN1*(P*THAA+Q*THBB)-ZN1*ZN1*P*Q*(THAA*THBB-THAB*THAB)
      FCT = 1.-FCT
      DFCT=VJAA*THBB*(1.-THAA*THAA)+VJBB*THAA*(1.-THBB*THBB)
      DFCT=ZN1*P*Q*(DFCT-2.*THAB*VJAB*(1.-THAB*THAB))
      DFCT=ZN1*(DFCT-P*VJAA*(1.-THAA*THAA)-Q*VJBB*(1.-THBB*THBB))
      XINC = FCT/DFCT
      IF (ABS(XINC/X0).LE.1.E-6) GO TO 14
```

```
   ITER = ITER+1
   XO = XO-XINC
   IF (ITER.LE.40) GO TO 10
   WRITE (4,25)
25 FORMAT(1X,'TOO MANY ITERATIONS !')
   GO TO 40
14 TEMP = 1./(XO-XINC)
   WRITE (4,31) P,Q,TEMP
31 FORMAT(3(5X,F10.3))
20 CONTINUE
40 PAUSE
   GO TO 2
   END
```

```
C-----SPECIFIC HEAT ØF THE ANNEALED PLANAR ISING MØDEL-----
      PI = 3.1415926536
   15 FØRMAT(F10.3)
      WRITE (4,17)
   17 FØRMAT(1X,'NUMBER ØF NEAREST NEIGHBØRS ?'$)
      READ (4,15) ZN
      WRITE (4,19)
   19 FØRMAT (1X,'TA , TB , TC , XC ?'$)
      READ (4,25) TA,TB,TC,XC
   25 FØRMAT(4F10.3)
   21 FØRMAT(3F10.3)
    2 CØNTINUE
      WRITE (4,11)
   11 FØRMAT(1X,'CØBALT CØNCENTRATIØN ?'$)
      READ (4,15) P
      WRITE (4,31)
   31 FØRMAT(1X,'TINIT,TFINAL,TSTEP ?'$)
      READ (4,21)TO,TF,TSTEP
      B = 1./SQRT(2.)
      A = 1.0+B
      TEM = ALØG(1.0+SQRT(2.))/2.
      VJA = TA*TEM
      VJB = TB*TEM
      Q = 1.-XC
      U=0.5-(XC*XC)/(A+B*EXP(-2.*VJA/TC))-(Q*Q)/(A+B*EXP(-2.*VJB/TC))
      TEM = B/(2.*XC*Q/U-A)
      VJAB = TC*ALØG(TEM)/2.
      P2 = P*P
      Q = 1.0-P
      Q2 = Q*Q
      PQ2 = 2.*P*Q
      VJA2 = VJA*VJA
      VJAB2 = VJAB*VJAB
      VJB2 = VJB*VJB
C----------START ITERATIØN--------------------------------
      ITER = 1
      WRITE (4,41) VJA,VJB,VJAB
   41 FØRMAT(1X,'JAA =',F10.3,5X,'JBB =',F10.3,5X,'JAB =',F10.3)
      SKO = 1.2
   10 CØNTINUE
      AA = SKO-VJA/TO
      AB = SKO-VJAB/TO
      BB = SKO-VJB/TO
      CSHAA = CØSH(AA)
      CSHAB = CØSH(AB)
      CSHBB = CØSH(BB)
      SHAA = SINH(AA)
      SHAB = SINH(AB)
      SHBB = SINH(BB)
      SHK = SINH(2.*SKO)
      CHK = CØSH(2.*SKO)
      THK = SHK/CHK
```

```
      AK = 2.*SHK/(CHK*CHK)
      AKC = 2.*THK*THK-1.0
      CALL ELLIP(AK,CEL1,CEL2,DER)
      TERM = (0.5+AKC*CEL1/PI)
      CORR = TERM/THK
      DCORR = TERM/SHK+2.*(CEL2-CEL1)/AK/PI
      DCORR = -2.*DCORR/SHK
      DAA1 = (CSHAA/SHAA)-CORR
      DAB1 = (CSHAB/SHAB)-CORR
      DBB1 = (CSHBB/SHBB)-CORR
      DAA2 = CSHAA-CORR*SHAA
      DAB2 = CSHAB-CORR*SHAB
      DBB2 = CSHBB-CORR*SHBB
      FX = (P2/DAA1)+(PQ2/DAB1)+(Q2/DBB1)
      SUM1 = P2/(DAA1*DAA1)+PQ2/DAB1/DAB1 +Q2/DBB1/DBB1
      SUM2 =(P2/DAA2/DAA2)+(PQ2/DAB2/DAB2)+Q2/DBB2/DBB2
      DFX = DCORR*SUM1+SUM2
      SKINC = FX/DFX
      IF (ABS(SKINC/SKO).LE.1.E-6) GO TO 20
      ITER = ITER+1
      SKO = SKO-SKINC
   61 FORMAT(5X,I3,5X,F10.3)
      IF (ITER.LE.40) GO TO 10
      WRITE (4,45)
   45 FORMAT(1X,'TOO MANY ITERATIONS !')
      GO TO 40
   20 SKI = 1./SKO
      DAA22 = DAA2*DAA2
      DAB22 = DAB2*DAB2
      DBB22 = DBB2*DBB2
      SUM2 = P2*VJA/DAA22 +PQ2*VJAB/DAB22 +Q2*VJB/DBB22
      SUM3 = P2*VJA2/DAA22 +PQ2*VJAB2/DAB22 +Q2*VJB2/DBB22
      CORRM = 1.-CORR*CORR
      TERM1 = SUM2*SUM2/(SUM1-1./(CORRM-DCORR))
      CP =(SUM3*CORRM+TERM1)*ZN/(TO*TO)
      WRITE (4,51)TO,SKI,CORR,DCORR,CP
   51 FORMAT(F7.3,5X,F10.3,2(5X,E10.3),5X,F10.3)
      TO = TO+TSTEP
      IF (TO.GT.TF) GO TO 40
      ITER = 1
      GO TO 10
   40 PAUSE
      GO TO 2
      END
```

```
      SUBROUTINE ELLIP(AK,CEL1,CEL2,DER)
C-----THIS SUBROUTINE COMPUTES COMPLETE ELLIPTIC--------
C-----INTEGRALS OF THE FIRST AND SECOND KINDS-----------
      PI = 3.1415926536
      PI2 = PI/2.
      IFCT = 2
      SUM = AK*AK
      AKC2 = 1.-SUM
      AKC = SQRT(AKC2)
      CEL1 = 1.0E+20
      CEL2 = 1.0
      DER = 1.0E+20
      IF (ABS(AKC).LE.1.E-6) RETURN
      AARI = 1.0
      GEO = AKC
   10 CONTINUE
      ARI = (AARI+GEO)/2.
      DIFF = AARI-ARI
      SUM = SUM+IFCT*DIFF*DIFF
      IFCT = 2*IFCT
      GEO = SQRT(AARI*GEO)
      AARI = ARI
      IF (GEO/ARI-0.999999) 10,20,20
   20 CEL1 = PI2/ARI
      SUM = SUM/2.
      CEL2 = CEL1*(1.-SUM)
      DER = CEL1*(AK-SUM/AK)/AKC2
      RETURN
      END
```

```
C-----SPECIFIC HEAT ØF ANNEALED BETHE LATTICE---------
      ATH(X) = 0.5*ALØG((1.+X)/(1.-X))
      WRITE (4,3)
    3 FØRMAT(1X,'TA AND TB ?'$)
      READ (4,5) TA,TB
    5 FØRMAT(2F10.3)
      WRITE(4,11)
   11 FØRMAT(1X,'NØ. ØF NEAREST NBRS ?'$)
      READ (4,15) ZN
   15 FØRMAT(F10.3)
      ZN1 = 1./( ZN-1.)
      WRITE(4,17)
   17 FØRMAT(1X,'TEMP. AND CØNC. FØR FIT ?'$)
      READ (4,5) TC,P
      Q = 1.-P
      TEM = ATH(ZN1)
      VJAA = TA*TEM
      VJBB = TB*TEM
      IF(TC.EQ.0.) GØ TØ 6
      THAA = TANH(VJAA/TC)
      THBB = TANH(VJBB/TC)
      THAB = (ZN1-P*P*THAA-Q*Q*THBB)/(2.*P*Q)
      VJAB =TC* ALØG((1.+THAB)/(1.-THAB))/2.
      GØ TØ 8
    6 WRITE (4,35)
   35 FØRMAT(1X,'ENTER JAB ='$)
      READ (4,15) VJAB
      IF (VJAB.EQ.0.) VJAB = SQRT(VJAA*VJBB)
    8 CØNTINUE
      WRITE (4,21) VJAA,VJBB,VJAB
   21 FØRMAT(1X,'JAA =',F10.3,5X,'JBB =',F10.3,5X,'JAB =',F10.3)
    2 CØNTINUE
      WRITE (4,19)
   19 FØRMAT(1X,'ENTER CØNC. = ?'$)
      READ (4,15) P
      Q = 1.-P
      P2 = P*P
      Q2 = Q*Q
      PQ = 2.*P*Q
      WRITE (4,23)
   23 FØRMAT(1X,'TINIT,TINC,TMAX ?'$)
      READ (4,9) TO,TINC,TMAX
    9 FØRMAT(3F10.3)
      WRITE (4,27)
   27 FØRMAT(1X,'INITIAL GUESSES FØR K AND HO ?'$)
      READ (4,5) AKO,HO
C-----FIND EFFECTIVE FIELD CØRRESPØNDING TØ K--------
   12 ITER2 = 0
   14 CØNTINUE
      AFK = TANH(AKO)
      IF (AFK.LE.ZN1) HO = 0.0
```

```
   IF(HO.EQ.0.0) GO TO 16
   ITER1 = 0
10 CONTINUE
   THO = TANH(HO)
   THL = TANH(HO*ZN1)
   FCT1 = AFK*THO-THL
   IF (ABS(FCT1).LE.1.E-6) GO TO 16
   DFCT1 = AFK*(1.-THO*THO)-ZN1*(1.-THL*THL)
   HINC = FCT1/DFCT1
   IF (ABS(HINC/HO).LE.1.E-6) GO TO 16
   ITER1 = ITER1+1
   HO = HO -HINC
   IF (ITER1.LE.40) GO TO 10
   WRITE (4,37)
37 FORMAT(1X,'TOO MANY ITERATIONS IN FINDING HO !')
   GO TO 40
16 CONTINUE
   D1LK = ZN1*(1.-AFK*AFK*THO*THO)-AFK*(1.-THO*THO)
   D1LK = THO*(1.-AFK*AFK)/D1LK
   SH2L = SINH(2.*HO)
   CH2L = COSH(2.*HO)
   EX2K = EXP(2.*AKO)
   DEN = EX2K*CH2L+1.
   CORR = 1.-(2./DEN)
   DCORR = 4.*EX2K*(CH2L+SH2L*D1LK)/(DEN*DEN)
 C-----FIND AKO CORRESPONDING TO TO-------------------
   CHAA = COSH(AKO-VJAA/TO)
   CHAB = COSH(AKO-VJAB/TO)
   CHBB = COSH(AKO-VJBB/TO)
   SHAA = SINH(AKO-VJAA/TO)
   SHAB = SINH(AKO-VJAB/TO)
   SHBB = SINH(AKO-VJBB/TO)
   DENAA = CHAA-CORR*SHAA
   DENAB = CHAB-CORR*SHAB
   DENBB = CHBB-CORR*SHBB
   FCT2 = (P2*SHAA/DENAA)+(PQ*SHAB/DENAB)+(Q2*SHBB/DENBB)
   DAA2 = DENAA*DENAA
   DAB2 = DENAB*DENAB
   DBB2 = DENBB*DENBB
   IF (ABS(FCT2).LT.1.E-6) GO TO 20
   DFCT2=P2*(1.+DCORR*SHAA*SHAA)/DAA2+PQ*(1.+DCORR*SHAB*SHAB)/DAB2
   DFCT2 =Q2*(1.+DCORR*SHBB*SHBB)/DBB2 + DFCT2
   AKINC = FCT2/DFCT2
   IF (ABS(AKINC/AKO).LE.1.E-6) GO TO 20
   ITER2 = ITER2+1
   AKO = AKO-AKINC
   IF(ITER2.LE.40) GO TO 14
   WRITE (4,41)
41 FORMAT(1X,'TOO MANY ITERATIONS IN FINDING K  !')
   GO TO 40
20 CONTINUE
```

```
   SUM1 = P2*SHAA*SHAA/DAA2 + PQ*SHAB*SHAB/DAB2
   SUM1 = Q2*SHBB*SHBB/DBB2 +SUM1
   SUM2 = VJAA*P2/DAA2 + VJAB*PQ/DAB2 + VJBB*Q2/DBB2
   SUM3 = VJAA*VJAA*P2/DAA2 +VJAB*VJAB*PQ/DAB2
   SUM3 = VJBB*VJBB*Q2/DBB2 + SUM3
   TEM = 1.-CØRR*CØRR-DCØRR
   DKB = SUM2/(1.-SUM1*TEM)
   CP = ZN*(SUM3*(1.-CØRR*CØRR)-SUM2*TEM*DKB)/(TO*TO)
   WRITE (4,51) TO,AKO,HO,CØRR,DCØRR
51 FØRMAT(F6.3,4(5X,E11.4)$)
   WRITE (4,53) CP
53 FØRMAT(1H+,5X,F11.4)
   TO = TO+TINC
   IF (TO.GT.TMAX) GØ TØ 40
   GØ TØ 12
40 PAUSE
   GØ TØ 2
   END
```

```
C-----SPECIFIC HEAT OF QUENCHED PLANAR BETHE LATTICE-----
      ATH(X)=0.5*ALOG((1.+X)/(1.-X))
      LOGICAL VARI
      DIMENSION W(10),ENER(3)
      VNULL = 1.E-6
      WRITE(4,3)
    3 FORMAT(1X,'TA & TB ?'$)
      READ (4,5) TA,TB
    5 FORMAT(2F10.3)
   15 FORMAT(F10.3)
      ZNI = 1/3.
      Z = 4.
      WRITE(4,17)
   17 FORMAT(1X,'TEMP. AND CONC. FOR FIT ?'$)
      READ (4,5) TC,P
      Q = 1.-P
      TEM = ATH(ZNI)
      VJAA = TA*TEM
      VJBB = TB*TEM
      IF (TC.EQ.0.)GO TO 6
      THAA =TANH(VJAA/TC)
      THBB = TANH(VJBB/TC)
      THAB = (ZNI-P*THAA)*(ZNI-Q*THBB)/(P*Q)
      THAB = SQRT(THAB)
      VJAB = TC*ATH(THAB)
      GO TO 8
    6 WRITE(4,35)
   35 FORMAT(1X,'ENTER JAB ='$)
      READ (4,15) VJAB
      IF(VJAB.EQ.0.) VJAB=SQRT(VJAA*VJBB)
    8 CONTINUE
      WRITE (4,21) VJAA,VJBB,VJAB
   21 FORMAT(1X,'JAA =',F10.3,5X,'JBB =',F10.3,5X,'JAB =',F10.3)
    2 CONTINUE
      WRITE (4,19)
   19 FORMAT(1X,'ENTER CONC. ='$)
      READ (4,15) P
      Q = 1.-P
      W(1) = Q**4
      W(2) = 4.*P*Q*Q*Q
      W(3) = 6.*P*P*Q*Q
      W(4) = 4.*P*P*P*Q
      W(5) = P**4
      WRITE (4,23)
   23 FORMAT(1X,'TINIT,TINC,TMAX ?'$)
      READ (4,9)TO,TINC,TMAX
    9 FORMAT(3F10.3)
      WRITE (4,33)
   33 FORMAT(1X,'REL. INC. FOR DER. ?'$)
      READ(4,15) HINC
      WRITE(4,27)
```

```
27 FORMAT(1X,'GUESSES FOR HA & HB ?'$)
   READ(4,5) XO,YO
C-----START  ITERATION-----------------------------------
10 CONTINUE
   DO 80 K=1,3
   GO TO (62,64,66) ,K
62 TI = 1./(TO*(1.+HINC))
   GO TO 50
64 TI = 1./(TO*(1.-HINC))
   GO TO 50
66 TI = 1./TO
50 CONTINUE
   ITER = 0
   BAA = VJAA*TI
   BBB = VJBB*TI
   BAB = VJAB*TI
   TAA = TANH(BAA)
   TBB = TANH(BBB)
   TAB = TANH(BAB)
12 CONTINUE
   THX = TANH(XO)
   THY = TANH(YO)
   A = (1.+THX*TAA)/(1.-THX*TAA)
   B = (1.+THY*TAB)/(1.-THY*TAB)
   C = (1.+THX*TAB)/(1.-THX*TAB)
   D = (1.+THY*TBB)/(1.-THY*TBB)
   TAAS = TANH(XO+BAA)
   TAAD = TANH(XO-BAA)
   TABS = TANH(XO+BAB)
   TABD = TANH(XO-BAB)
   TBBS = TANH(YO+BBB)
   TBBD = TANH(YO-BBB)
   TBAS = TANH(YO+BAB)
   TBAD = TANH(YO-BAB)
   SA1 = 0.
   SB1 = 0.
   SNAA1 = 0.
   SNAB1 = 0.
   SNBB1 = 0.
   SNBA1 = 0.
   SNA2A = 0.
   SNA2B = 0.
   SNA1A = 0.
   SNABA = 0.
   SNABB = 0.
   SNB2B = 0.
   SNB2A = 0.
   SNB1B = 0.
   SNB1A = 0.
   SNA1B = 0.
   DO 22 I=1,5
```

```
      NA = I-1
      NB = 4-NA
      ZAPM = (A**NA)*(B**NB)
      ZBPM = (C**NA)*(D**NB)
      SA1 = SA1+W(I)/(1.+ZAPM)
      SB1 = SB1+W(I)/(1.+ZBPM)
      SNAA1 = SNAA1+NA*W(I)/(1.+ZAPM)
      SNAB1 = SNAB1+NA*W(I)/(1.+ZBPM)
      SNBB1 = SNBB1+NB*W(I)/(1.+ZBPM)
      SNBA1 = SNBA1+NB*W(I)/(1.+ZAPM)
      SNA2A = SNA2A+NA*NA*W(I)*ZAPM/((1.+ZAPM)**2)
      SNA2B = SNA2B+NA*NA*W(I)*ZBPM/((1.+ZBPM)**2)
      SNA1A = SNA1A+NA*W(I)*ZAPM/((1.+ZAPM)**2)
      SNABA = SNABA+NA*NB*W(I)*ZAPM/((1.+ZAPM)**2)
      SNABB = SNABB+NA*NB*W(I)*ZBPM/((1.+ZBPM)**2)
      SNB2B = SNB2B+NB*NB*W(I)*ZBPM/((1.+ZBPM)**2)
      SNB2A = SNB2A+NB*NB*W(I)*ZAPM/((1.+ZAPM)**2)
      SNB1B = SNB1B+NB*W(I)*ZBPM/((1.+ZBPM)**2)
      SNB1A = SNB1A+NB*W(I)*ZAPM/((1.+ZAPM)**2)
      SNA1B = SNA1B+NA*W(I)*ZBPM/((1.+ZBPM)**2)
   22 CONTINUE
      FXY = P*(TAAS*(Z*P-SNAA1)+TAAD*SNAA1)-Z*P*(1.-2.*SA1)
      FXY = FXY+Q*(TABS*(Z*P-SNAB1)+TABD*SNAB1)
      GXY = Q*(TBBS*(Z*Q-SNBB1)+TBBD*SNBB1)-Z*Q*(1.-2.*SB1)
      GXY = GXY+P*(TBAS*(Z*Q-SNBA1)+TBAD*SNBA1)
      VAR1 = (ABS(FXY).LE.VNULL).AND.(ABS(GXY).LE.VNULL)
      IF (VAR1) GO TO 30
      DFX = P*((1.-TAAS*TAAS)*(Z*P-SNAA1)+(1.-TAAD**2)*SNAA1)
      DFX = DFX+Q*((1.-TABS**2)*(Z*P-SNAB1)+(1.-TABD**2)*SNAB1)
      DFX = DFX+P*SNA2A*(TAAS-TAAD)**2+Q*SNA2B*(TABS-TABD)**2
      DFX = DFX-2.*Z*P*(TAAS-TAAD)*SNA1A
      YT=P*(TAAS-TAAD)*(TBAS-TBAD)*SNABA
      YT = YT+Q*(TABS-TBAD)*(TBBS-TBBD)*SNABB
      DFY = YT-2.*Z*P*(TBAS-TBAD)*SNB1A
      DGX = YT-2.*Z*Q*(TABS-TABD)*SNA1B
      DGY = Q*((1.-TBBS**2)*(Z*Q-SNBB1)+(1.-TBBD**2)*SNBB1)
      DGY = DGY+P*((1.-TBAS**2)*(Z*Q-SNBA1)+(1.-TBAD**2)*SNBA1)
      DGY = DGY+Q*SNB2B*(TBBS-TBBD)**2+P*SNB2A*(TBAS-TBAD)**2
      DGY = DGY-2.*Z*Q*(TBBS-TBBD)*SNB1B
      VAR1 = (ABS(XO).LE.VNULL).AND.(ABS(YO).LE.VNULL)
      IF (VAR1) GO TO 20
      DET = DFX*DGY-DFY*DGX
      XINC = (FXY*DGY-GXY*DFY)/DET
      YINC = (GXY*DFX-FXY*DGX)/DET
      VAR1 = (ABS(XINC/XO).LE.VNULL).AND.(ABS(YINC/YO).LE.VNULL)
      IF (VAR1) GO TO 30
      XO = XO-XINC
      YO = YO-YINC
      ITER = ITER+1
      IF(ITER.LE.40) GO TO 12
      WRITE (4,25)
```

```
25 FØRMAT(1X,'TØØ MANY ITERATIØNS !')
   GØ TØ 40
20 XO = 0.
   YO = 0.
30 CØNTINUE
   IF (K.EQ.3) GØ TØ 80
   TERM1 = VJAA*(Z*P*TAAS-SNAA1*(TAAS+TAAD))
   TERM1 = TERM1+VJAB*(Z*Q*TBAS-SNBA1*(TBAS+TBAD))
   TERM2 = VJBB*(Z*Q*TBBS-SNBB1*(TBBS+TBBD))
   TERM2 = TERM2+VJAB*(Z*P*TABS-SNAB1*(TABS+TABD))
   ENER(K) = P*TERM1+Q*TERM2
80 CØNTINUE
   CP = (ENER(2)-ENER(1))/(2.*TO*HINC)
   WRITE (4,31)TO,XO,YO,CP
31 FØRMAT(F10.3,3(5X,F11.4))
   TO = TO+TINC
   IF(TO.LE.TMAX) GØ TO 10
40 PAUSE
   GØ TØ 2
   END
```

MICHIGAN STATE UNIVERSITY LIBRARIES
3 1293 03085 5583